Assessment of Hip Fracture Risk using Cross-Section Strain Energy Determined from QCT-based Finite Element Model

By

Hossein Kheirollahi Nataj Bisheh

A thesis submitted to
the Faculty of Graduate Studies in partial fulfilment of
the requirements for the degree of
Master of Science

Department of Mechanical Engineering
Faculty of Engineering
University of Manitoba
Winnipeg, Manitoba

April 2015

Abstract

Accurate assessment of hip fracture risk is very important to prevent hip fracture and to monitor the effect of a treatment. A subject-specific QCT-based finite element model was constructed to assess hip fracture risk at the critical locations of femur during the single-leg stance and the sideways fall. The aim of this study was to improve the prediction of hip fracture risk by introducing a more proper failure criterion to more accurately describe bone failure mechanism. Hip fracture risk index was defined using the strain energy criterion, which is able to integrally consider information such as stresses, strains and material properties in bone failure. It was found that the femoral neck and the intertrochanteric region have higher fracture risk than other part of the femur, probably owing to the larger content of cancellous bone in these regions. The study results also suggested that women are more prone to hip fracture than men. The effects of different parameters such as age, body height, weight, and BMI on hip fracture risk were also investigated in this study. The findings in this study have a good agreement with those clinical observations reported in the literature. The main contributions from this study include: (1) introducing an algorithm for hip fracture risk assessment at the critical locations of femur using the strain energy criterion and QCT-based finite element modeling, (2) theoretically more reasonable definition of hip fracture risk index based on the strain energy criterion, and (3) a semi-automatic finite element analysis and automatic calculation of hip fracture risk index at the critical locations of femur using in-house

developed computer codes. The proposed hip fracture risk index based on the strain energy criterion will be a promising tool for more accurate assessment of hip fracture risk. However, experimental validation should be conducted before its clinical applications.

Acknowledgments

I owe a great deal of thanks to my supervisor Dr. Yunhua Luo for offering me the opportunity to study at the University of Manitoba and participate in this project, and for his motivating guidance and support throughout the research work and the completion of my dissertation. I also thank the examination committee members, Drs. Qingjin Peng and Francis Lin, for their time spent in evaluating the thesis and for their valuable comments.

I would like to express my gratitude to the Winnipeg Health Science Centre for providing the clinical cases in this study, and also the Natural Sciences and Engineering Research Council (NSERC) and the Manitoba Health Research Council (MHRC) for financial support of this project. I would also like to express my special thanks to Mr. Eric Renteria and Mr. Tony Aliatim, Application Engineer – Mimics Innovation Suite (Materialise, USA), for their technical support and guidance.

My thanks also go to my colleagues Dr. Tanvir Faisal, Siamak, Masoud, Yujia, Sean, Ida, Eniyavan, Sharif, Huijuan, and Yichen in the Computational Biomechanics Group for all the academic discussions and happy time working with them. I am really grateful to my all friends in Winnipeg for providing me so many merry moments and encouragement.

I would like to express my deep love and appreciation to my parents, father-in-law, mother-in-law, sister, brother, sister-in-law, brother-in-law, and my cute nieces for their consistent and unconditional love and support through my all life. Finally, my special appreciation to my lovely wife, Shima, for her understanding and love during the past year.

Dedication

To my parents

&

my lovely wife

Contents

List of Tables

List of Figures

List of Copyrighted Material

Figure 1-1 was cited from Osteoporosis Canada. Permission was obtained on April 13, 2015.

Figure 1-2 was cited from Osteoporosis Canada. Permission was obtained on April 13, 2015.

Figure 2-1 was cited from Valeo Health Clinic. Permission was obtained on April 13, 2015.

Figure 2-2 was cited from Wikipedia. Permission was obtained on March 31, 2015.

Figure 2-4 was cited from "Rachner, T. D., Khosla, S., and Hofbauer, L. C., 2011, "Osteoporosis: now and the future," The Lancet, **377**(9773), pp. 1276-1287.". Permission was obtained on April 27, 2015.

Figure 2-5 was cited from Advanced Orthopedic Specialists. The permission was obtained on April 13, 2015.

Figure 2-6 was cited from "De Bakker, P. M., Manske, S. L., Ebacher, V., Oxland, T. R., Cripton, P. A., and Guy, P., 2009, "During sideways falls proximal femur fractures initiate in the superolateral cortex: Evidence from high-speed video of simulated fractures," J. Biomech., **42**(12), pp. 1917–1925". Permission was obtained on April 27, 2015.

List of Abbreviations

2-D	Two-Dimensional
3-D	Three-Dimensional
aBMD	Areal Bone Mineral Density
APDL	ANSYS Parametric Design Language
BMC	Bone Mineral Content
BMD	Bone Mineral Density
BMI	Body Mass Index
DICOM	Digital Imaging and Communications in Medicine
DXA	Dual-Energy X-ray Absorptiometry
FE	Finite Element
FEM	Finite Element Method
FOS	Factor of Safety
FRAX®	Fracture Risk Assessment Tool
FRI	Fracture Risk Index
HR-pQCT	High-Resolution Peripheral Quantitative Computed Tomography
HSA	Hip Structural (or Strength) Analysis
HU	Hounsfield Unit

IntT CS	Intertrochanteric Cross-Section
ROI	Region of Interest
SFN CS	Smallest Femoral Neck Cross-Section
SubT CS	Subtrochanteric Cross-Section
QCT	Quantitative Computed Tomography
vBMD	Volumetric Bone Mineral Density
WHO	World Health Organization

List of Symbols

B	Matrix of Shape Functions Derivatives
h	Body Height
w	Body Weight
ρ_{ash}	Bone Ash Density
σ_3	The Third Principal Stress (Compressive Stress)
r	Correlation Coefficient
J	Jacobean Matrix
d	Displacement Vector
F	Force
η	Fracture Risk Index
ν	Poisson's Ratio
D	Material Properties Matrix
N	Newton (force unit)
p	Probability of Statistical Significance
U_v	Volumetric Strain Energy
U_d	Distortion Strain Energy
U	Strain Energy

$\widehat{U}$	Strain Energy Density
σ_1	The First Principal Stress (Tensile Stress)
ε	Strain
σ	Stress
ε_{vM}	von Mises Strain
σ_{vM}	von Mises Stress
ε_Y	Yield Strain
U_Y	Yield Strain Energy
$\widehat{U}_Y$	Yield Strain Energy Density
σ_Y	Yield Stress
E	Young's Modulus
W_i	Weight at the Integration Points

Chapter 1

Introduction

1.1 Background and Motivation

A major cause of suffering, disability, and death in the elderly is hip and other osteoporotic fractures. Osteoporosis is a skeletal disease determined by low bone mass and micro-architectural deterioration (Figure 1-1) with an increase in the possibility of bone fracture [1]. Osteoporosis is often known as a "silent disease" because bone loss occurs without any symptom [2]. Many factors, in addition to low bone mineral density (BMD), independently contribute to the risk of osteoporotic fracture, and in particular for hip fracture, including body mass index (BMI), age, history of maternal hip fracture, body weight, height, poor health, previous hyperthyroidism, poor depth perception, tachycardia, previous fracture, benzodiazepine use, low calcium intake, reduced sunlight exposure, early menopause, smoking, alcohol consumption, and physical activity levels [3,4]. Previous hip fracture increases the risk of second hip fracture two to ten folds [5].

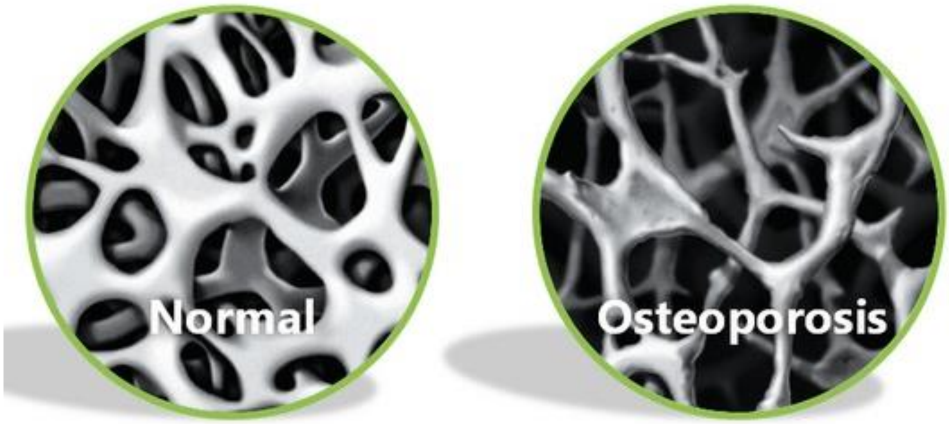

Figure 1-1. Bone mass in normal and osteoporotic conditions [6] (courtesy of Osteoporosis Canada).

Osteoporotic fractures are more common than heart attack, stroke, and breast cancer in Canada (Figure 1-2). At least one in three women and one in five men may experience an osteoporotic fracture during their lifetime [6]. The statistical studies show that hip fractures are increasing dramatically in the elderly. Ninety percent of hip fractures occur in individuals older than 70 years of age [7,8]. The estimation of total number of hip fractures in men and women in 1990 was 338,000 and 917,000 respectively over the world [9]. the number of hip fractures is estimated to 2.6 million by the year 2025, and 4.5 million by the year 2050 over the world [9]. About 25,000 hip fractures were reported in Canada in 1993 [6].

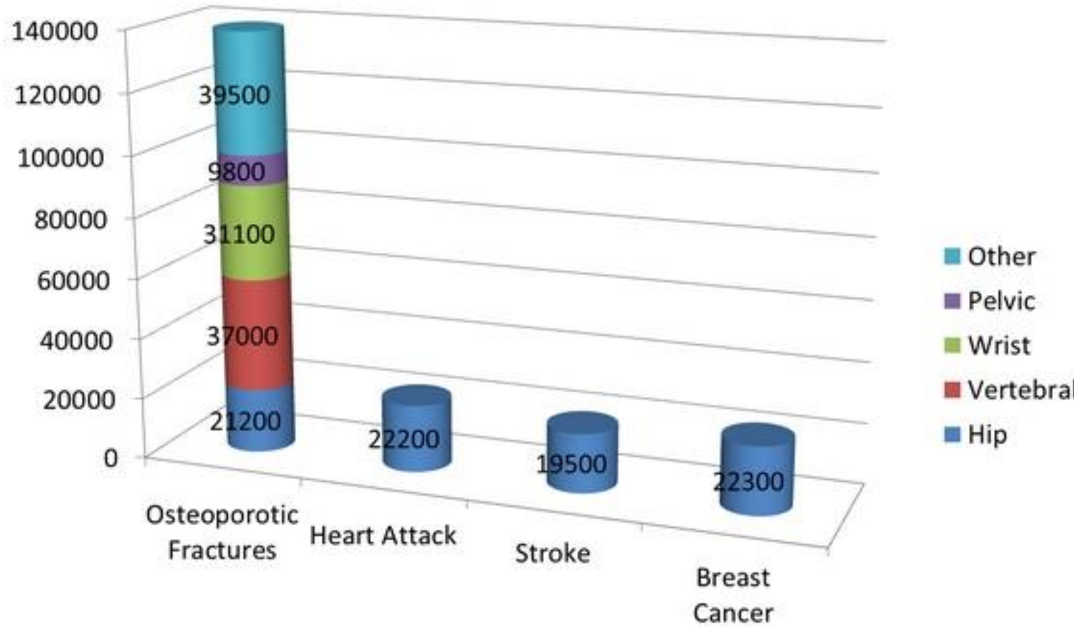

Figure 1-2. Annual incidence of common diseases in Canada [6] (courtesy of Osteoporosis Canada).

Osteoporotic fractures also cause high economic costs for the health-care systems worldwide. Treatment costs of all osteoporotic fractures have been estimated to be $20 billion in the USA and about $30 billion in the European Union per year [1]. The annual cost to the Canadian healthcare system for treating osteoporosis and the corresponding fractures was over $2.3 billion as of 2010. This cost will increase to $3.9 billion if a proportion of Canadians are assumed to living in long-term care facilities because of osteoporosis [6]. By the increasing trend in hip fractures because of the aging of the population, the worldwide annual costs of hip fractures in the year 2050 have been estimated to be $131.5 billion [10]. Hip fracture reduces the quality of life dramatically, so that it can result in reduction or loss of mobility, disfigurement, lowered self-esteem, and decreased independence [6].

Hip fracture leads to an up to 20% chance of death, a 25% chance of long term disability , and less than a 50% chance of full recovery [11]. Reduced bone strength and falling are usually the main causes of hip fracture. Hip fracture is the most common serious injury associated with the fall of an elderly person. Falls are the main etiological factor in over 97% of hip fractures [12]. Sideways falls, in contrast to forward or backward falls, increase the risk of hip fracture. Risk of hip fracture in the elderly is six times greater during the sideways falls than the forward or backward falls, and 30 times greater if the fall–related impact force is directly applied on the hip region [13].

Therefore, due to hip fracture prevalence among the elderly, high medical care costs, and the associated social problems, hip fracture risk should be assessed for osteoporosis patients to prevent fracture. The goal in the assessment of hip fracture risk is to identify who is at a risk of osteoporotic hip fracture and to put the patient in a program to prevent future fractures.

1.2 Literature Review

1.2.1 Available Methods for Hip Fracture Risk Assessment

Bone mineral density captured by Dual-Energy X-ray Absorptiometry (DXA) is now a well-established practice in clinical centres for screening osteoporosis. This method evaluates the bone mineral densities at several critical locations of the patient and compares them with those of healthy young adults. DXA is the most widely used method for measuring BMD due to its low dosage of radiation, high precision, stable calibration, and short scan time, less than 2 minutes for the spine, hip or forearm, and less than 3 minutes for the total body [14]. DXA employs two different X-ray energies to determine bone mineral content (BMC). With the preselected area, areal bone mineral density (aBMD) (g/cm^2) can be derived via BMC divided by the area of a region of interest (ROI) on lumbar spine, hip, forearm, or even whole body. The aBMD of an individual is then compared to the references in a proper population database, and the result is commonly expressed as T-score and Z-score. The T-score indicates the difference between the patient's BMD and the mean peak bone mass achieved in healthy young adults. The operational range of T-score for diagnosing osteoporosis has been recommended by the World Health Organization (WHO). T-score above -1 (T-score>-1) indicates normal bone density (low fracture risk), T-score from -2.5 to -1 (-2.5<T-score<-1) indicates low bone mass (intermediate fracture risk), and T-score lower than -2.5 (T-score<-2.5) indicates the presence of osteoporosis (high fracture risk) [15]. However, the limitation of using T-score lies in subjects with or without hip fractures may have the same BMD values [16]. Z-score, an indicator comparing the patient's aBMD with the mean value derived from the same age, sex, and ethnicity, is sometimes used in assessing hip fracture risk [17]. It can be used particularly in situations when use of T-score is inappropriate to assess fracture risk. High proportion of the elderly are classified as osteoporotic according to the WHO criteria, even their BMD is normal for their age [18]; it means T-score is not a proper fracture risk evaluator in the elderly. This deficiency does not appear in Z-score measurement since the patient's BMD is compared with that of the patient's peers with matched age. However, Z-score may be confusing since it obscures age as a risk factor in assessing osteoporosis [19]. A DXA image cannot provide any information about the distribution of mineral along the projection path; so, it is inappropriate to be used to draw conclusions about tissue mineralization or porosity [20]. T-scores cannot be used for children and young adults [21], as their bone density has not yet reached the peak value. On the other hand, the WHO definition of high risk of fracture (T-score<-2.5) only covers a very small percentage of the actual high-risk patients while the majority of actual fracture cases recorded by clinic occurred with T-score above the threshold. Therefore, their accuracy in assessing individual fractures is limited.

Fracture Risk Assessment Tool (FRAX®) is a tool to evaluate an individual's fracture probability in the next 10 years, adopted by the WHO in 2008 [22]. The FRAX® model has been developed from studying population-based cohorts in Europe, North America, Asia and Australia. It has been established as a tool to identify and treat patients with a high risk of bone fractures. Not all risk factors are properly considered in FRAX® and the actual risk may be considerably underestimated. The main limitations of the FRAX® include: it is a statistical model and fracture risk is not consistent within 10 years with some of the treatment results [23]. FRAX® also does not take into account fall-induced impact force that is critically important in the hip fracture risk assessment [24,25].

Hip Structural (or Strength) Analysis (HSA) programs are now commercially available and are used to automatically assess the geometric and structural parameters of the femur. The HSA program measures not only the BMD of the femur but also the structural geometry of cross-sections traversing the femur at specific locations [26].

Although, DXA scanners have high precision for measuring BMD, but they were not designed to measure geometry [27]. Small changes in femur position have a large effect on the projected dimensions of the geometry. Accuracy in measuring structural parameters of paired images using HSA is worse than conventional BMD due to positioning inconsistence [28]. HSA is not able to distinguish mineralization contributed by different bones, for example cancellous and cortical bone, and it thus measures average tissue mineralization which is sometimes misleading [27].

By integrating an imaging technology such as DXA or Quantitative Computed Tomography (QCT) and a numerical method such as the Finite Element Method (FEM), a category of more reliable tools for assessing hip fracture risk have been developed. [29–40]. These methods also do not have the aforementioned limitations. The FEM is a computational method that can be used to study the mechanical aspect of hip fracture. Image–based finite element analyses can more accurately predict fracture risk of femur. DXA- and QCT-based finite element (FE) analyses are the two commonly used methods for in-vivo assessment of hip fracture risk. In DXA-based FE analysis, a two-dimensional (2-D) FE model of the femur is constructed from the patient’s hip DXA image. In assessment of hip fracture risk using a DXA-based FE model, the real-world boundary and loading conditions cannot be accurately considered. Although DXA-based FE models are 2-D, they are preferred in clinics because the radiation dosage used in the DXA scanning is much lower than that of the QCT scanning. Whereas the purpose is to accurately determine the actual stresses/strains in the bone for precise fracture risk assessment, all components in the FE model, i.e. the geometry, the material properties, and the loading and boundary conditions, must be faithful to the real-world scenario. In contrast to planar DXA scan which is widely utilized, QCT scan provide information on three-dimensional (3-D) geometry and volumetric bone mineral density (vBMD) (g/cm^3) of the cancellous and cortical bone so that a faithful FE model of the bone can be generated. Therefore, a subject-specific QCT-based FE model, which is a 3-D FE model and more faithfully represents the real-world object, can provide more accurate assessment of hip fracture risk.

1.2.2 Bone Failure Criteria

Hip fracture under a stance force or impact force induced in sideways fall is usually measured by one of the two indices: Factor of Safety (FOS) or Fracture Risk Index (FRI). FOS less than one or FRI more than one indicates bone failure. For a precise assessment of hip fracture risk, FOS or FRI should be calculated accurately. For this purpose, parameters that are required in FOS and FRI calculation should be calculated accurately. One component required in accurate assessment of hip fracture risk is a proper failure criterion based on bone failure mechanism and microstructure. A number of 2-D and 3-D FE models have been developed in the literature to assess hip fracture risk.

Testi et al. [29] evaluated hip fracture risk using a 2-D FE model derived from DXA image of a surrogate femur. They validated their evaluation in-vitro using a replica of the human femur and then the predicted results were compared to strain-gauge measurements and to a 3-D FE model, with good agreement being observed. They considered the maximum principle strain criterion to assess hip fracture risk. Luo et al. [30] calculated the averaged FRI as the ratio between the effective stress (or von Mises stress) induced by the applied forces and the allowable stress (or yield stress) of the bone over an ROI. In their definition FRI was defined based on the von Mises stress failure criterion. Keyak et al. [41] assessed FOS to predict femur fracture load under two loading conditions - one representing the loading in a stance phase configuration and the other simulating the impact in a sideways fall configuration. Their study was based on 3-D FE model generated from CT data of the patient. They calculated FOS using the von Mises stress failure criterion. Lotz et al. [42,43] used the von Mises stress failure criterion for the cortical bone and the crushing-cracking stress criterion for the trabecular bone. In the study by Ota et al. [44] the hip fracture risk was assessed using the principle stress criterion.

In the previous studies [29,30,41–44] different failure criteria were considered for the hip fracture risk assessment. However, choosing a proper failure criterion to calculate FRI and FOS is challenging. Lotz et al. [42] and Schileo et al. [45] investigated the possibility of applying the strain-based criteria and compared their performance with the stress-based ones. According to the study of Lotz et al. [42], the von Mises strain criterion improved the hip fracture risk prediction, compared to the von Mises stress criterion. Schileo et al. [45] applied the maximum principle strain, the von Mises stress, and the maximum principle stress criteria and compared the results with the experimental findings under the same stance loading. Their study proved that the principal strain criterion predicted fracture risk better than the two stress-based criteria and its prediction was consistent with the experimental findings. Although, Schileo et al. [45] compared different failure criteria under the stance loading, they did not investigate their accuracy during the sideways fall. In the study reported by Keyak and Rossi [46], the performance of nine stress- and strain-based failure criteria in assessment of hip fracture risk was investigated. They evaluated the distortion energy, the Hoffman and a strain-based Hoffman analog, the maximum normal stress, the maximum normal strain, the maximum shear strain, the maximum shear stress, the Coulomb-Mohr, and the modified Mohr failure theories using a CT-based FE model of the femur. Two loading configurations, one simulating the single-leg stance and the other simulating the fall status were considered in their study. The results of their study suggest that the distortion energy and the maximum shear stress criteria may be the most accurate for identifying the fracture location under the stance loading or the impact in a fall.

The femur consists of inhomogeneous (porous) cancellous bone and nearly homogenous cortical bone, so, their failure mechanism is totally different due to their different microstructure. Failure mechanism of the cancellous bone is mostly in the form of buckling, and the failure of denser cancellous bone and the cortical bone is mostly characterized by local cracking [32,47]. Although stress- and strain-based failure criteria are accurate for ductile materials such as metal, they may not be accurate for bones because bone is classified as a brittle material [48]. The ultimate strain of metals is much larger than that of bones. Therefore, bone is considered as a brittle material rather than a ductile one. The tensile strength of bones is smaller than their compressive strength, which suggests that bone should be classified as one of the brittle materials [48]. Due to this property of bones, energies related to distortion and volume change should be taken into account in failure analysis. Therefore, the maximum distortion energy criterion that only considers the energy of distortion may not be accurate for bone failure analysis. The total strain energy, which is a combination of the energy due to element distortion (U_d) and the energy due to change of element volume (U_v), should be taken into account in bone failure analysis. Strain energy is a product of the stress and strain tensors, so it can be a more complete representative of both the force and deformation intensities [32]. Mirzaie et al. [32,49] predicted failure strength and failure patterns of human proximal femur and human vertebrae using the strain energy criterion with a QCT-based FE model. Their predictions of the failure loads and failure locations were in a good agreement with the experimental findings. The strain energy criterion is widely used in fracture analysis of engineering materials. It is usually used in crack problems [50–52], composite laminates [53,54], bone cement analysis [55], and other engineering fields. Therefore, computation of hip FRI over an ROI based on the strain energy criterion theoretically should be more accurate for assessing hip fracture risk. To the best of our knowledge, there are currently no published studies that use the strain energy criterion for the hip fracture risk assessment. We defined the hip fracture risk index over an ROI using the strain energy criterion. The aim of this study is to improve hip fracture risk assessment by using the strain energy criterion.

1.3 Objective of the Reported Research

The objective of this dissertation is to improve the prediction of hip fracture risk by developing a fracture risk index based on the strain energy criterion. Based on the discussions in Section 1.2, we define the hip fracture risk index using the strain energy criterion that is the most appropriate failure criterion according to bone failure mechanism. In total, sixty clinical cases (30 females and 30 males), including 120 right and left femurs, were obtained from the Winnipeg Health Science Centre for this investigation. For each clinical case, two finite element models for respectively the right and left femur were constructed using the patient's hip QCT images. Loading and boundary conditions for the single-leg stance and the sideways fall configuration were simulated; fracture risk indices at the critical regions on the femur were obtained using the new FRI definition. It is expected that the new fracture risk index based on the strain energy criterion can predict both the fracture risk level and the potential fracture locations more precisely than other failure criteria.

1.4 Outline of the Thesis

This thesis is organized as follows:

Chapter 2 - In this chapter, first the basic anatomy of the hip will be illustrated. Second, femur structure, physiology and material properties will be introduced. Then, hip fracture types and failure mechanism will be reviewed. Finally, the general finite element procedure for hip fracture analysis will be presented.

Chapter 3 - In this chapter, the procedure of constructing a QCT-based finite element model and finite element analysis of femur will be explained step by step. The definition of a new hip fracture risk index will be introduced, which is based on the cross-section strain energy.

Chapter 4 - In this chapter, verification results will be provided and explained to validate the in-house developed computer codes. Convergence tests will be presented. Stress and strain patterns in the femur will be presented and discussed. Hip fracture risk at the three critical cross-sections on femur for the 60 clinical cases will be calculated and hip fracture variations will be discussed. Finally, the effects of anthropometric parameters on hip fracture risk will be investigated.

Chapter 5 - In this chapter, major conclusions and contributions from this reported research will be summarized. Future research will be presented to remove the limitations in the current research.

Chapter 2

Theoretical Background

2.1 Basic Anatomy of the Hip

The human hip is a ball-and-socket joint, as shown in Figure 2-1, capable of tri-axial articulation. The ball bearing is the femoral head, located at the proximal end of the femur, and the socket bearing is the acetabulum, located at the three pelvic bones [56]. The stability in the hip is maintained by the deep socket-the acetabulum, and it is increased by the strong joint capsule and its surrounding muscles and ligaments [57].

The hip joint is also one of the largest joints in the body and is a major weight-bearing joint. Forces acting on the hip during walking can be five times of the person's body weight. A healthy hip can support body weight and allow motion without pain. Diseases or injuries will significantly influence on gait and place abnormal stress on the hip joint. To seriously damage the hip, a great force is needed because of the strong and large muscles of the thighs that support and protect the hip. Osteoarthritis, inflammatory arthritis, and bone fragility due to osteoporosis in the elderly can lead to the damage of the hip joint [57].

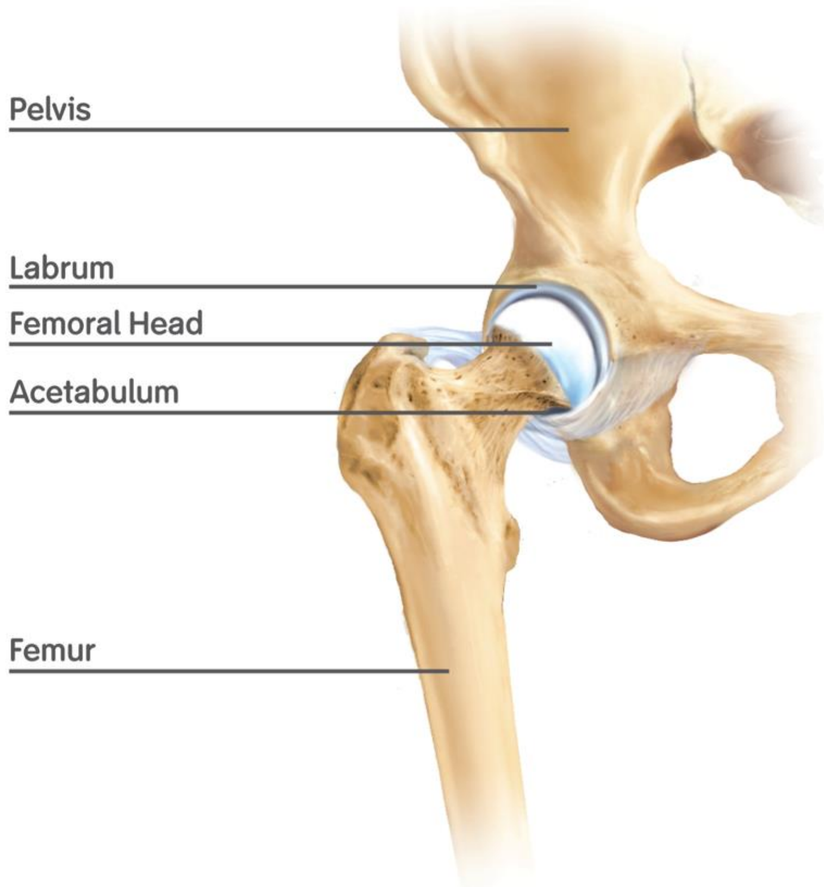

Figure 2-1. Anatomy of the hip joint [58**]** (courtesy of Valeo Health Clinic).

2.2 Femur Bone

2.2.1 Structure and Physiology

Bone is a dynamic living organ constituting the skeletal system together with other connective tissues such as ligaments, tendons, and cartilages. Bones support and protect the various organs of the body, store minerals, enable mobility, and also produce red and white blood cells. Bone is made of mineral (70%), organic matrix (22%), and water (8%) [59]. This kind of composition makes the bones stiff but tough, so that the skeleton is able to maintain the shape of the body [60]. Generally, the hardness, elasticity, and viscoelasticity of bone are respectively related to the mineral, organic matrix, and water.

Bones are classified according to their shape into long (e.g. humerus and femur), short (e.g. wrist bone), flat (e.g. cranial bones), irregular (e.g. vertebra), and sesamoid bone (e.g. patella) [61]. Mechanical functions of bone depend on its shape. Long bones, for example femur, act as a stiff lever to transmit muscle generated-forces over joints. On the other hand, the function of flat bones, for example skull bones, is to protect the internal organ such as the brain [62].

Anatomically, femur is divided into a number of sections, namely, diaphysis, epiphyses, metaphyses, articular cartilage, periosteum, medullary cavity, and endosteum. The structure of femur is shown in Figure 2-2. Different parts of the human femur are also described in Figure 2-3. The long bones such as the femur are mostly made of cortical (or compact) bone and trabecular (or cancellous) bone. In adult human, the cortical bone constitutes approximately 80% of total skeletal mass and the trabecular bone constitutes the remaining 20%. Spongy trabecular bone can be found in the inner parts of bones and dense cortical bone forms the outer layer of all bones (Figure 2-2). Cortical bone mainly can be found in the diaphysis, which surrounds the medullary cavity [60,63].

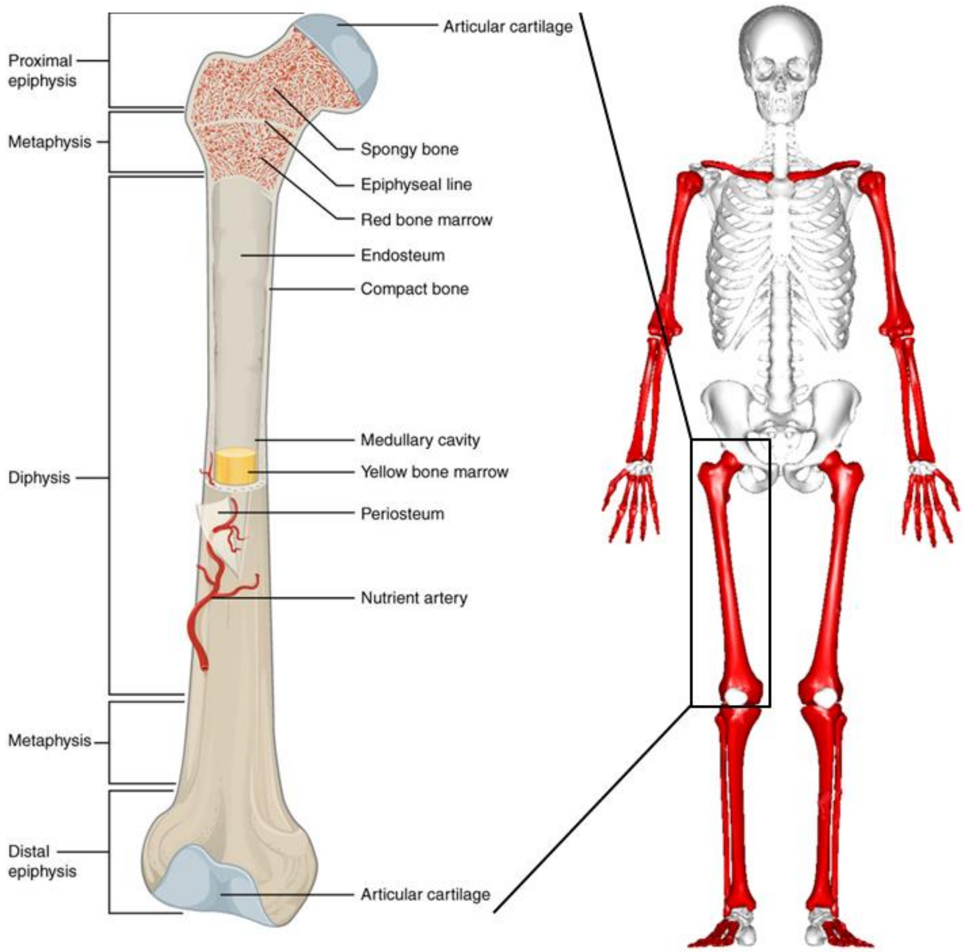

Figure 2-2. Anatomic structure of the human femur [64] (courtesy of Wikipedia).

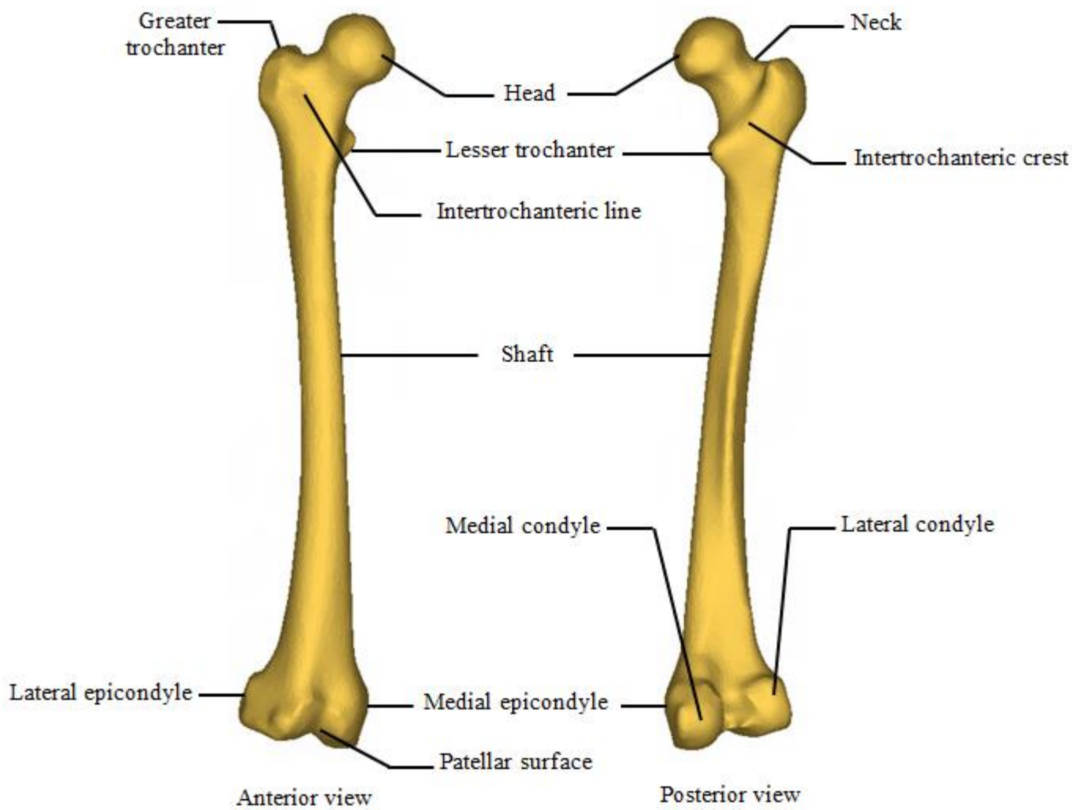

Figure 2-3. Different parts of the human femur.

2.2.2 Material Properties

Materials can be categorized into two groups based on their mechanical behavior in response to the direction of applied force: isotropic and anisotropic material. Isotropic material has identical mechanical behavior in all directions while anisotropic material has different behavior in different directions. There is a structure-mechanical function relationship in bone. Bone is built of a structural basic building block called mineralized collagen fibril [65]. In bones that have parallel-fibered structure such as long bones, the mineralized collagen fibrils are aligned in the direction parallel to the axis of long bones. This longitudinal orientation of the mineralized fibrils creates the highly anisotropic material behavior. It was reported that the parallel-fibered bone like the long bones has higher modulus in the direction parallel to the axis of bone than the one in the direction perpendicular to the axis [62,65,66]. Due to this property of long bones, they are classified as an anisotropic material.

Because of porous structure of trabecular bone, its mechanical properties such as elastic modulus can vary from one location to another at macrostructure level [67]. Different degrees of porosity of the trabecular bone make different degrees of density. The mechanical properties of bone are dependent on its density [68]. Due to variation of density in the trabecular bone, the mechanical properties also vary through the trabecular bone. Therefore, bone is also categorized as an inhomogeneous material.

Whereas there is not enough information on anisotropic properties of bone, it is typically considered isotropic in finite element analyses. Anisotropic long bones can often be considered as orthotropic material. To construct anisotropic/orthotropic FE models, the bone density and the directions of the orthotropic axes are required. The effects of anisotropic and isotropic material properties assignment on subject-specific FE analysis were investigated in the literature [69,70]. It was reported that inhomogeneous orthotropic material properties assignment is very important for the FE analysis of small bone specimens, while in global FE analysis of long bones such as the femur, anisotropy is less dominant, and an inhomogeneous isotropic material model can be used [69]. The results of another study [70] showed that there is no significance difference between acquired results from isotropic and orthotropic material properties assignments of femur under two loading conditions (double-leg standing and single-leg standing).

There are two ways to assign material properties into a bone FE model: homogeneous and inhomogeneous. Homogenous material properties assignment is simpler and takes less time. But due to inhomogeneous property of bone, considering homogenous material properties is unrealistic and reduces the accuracy of subject-specific FE analysis. In homogenous material properties assignment, constant densities are considered for both the trabecular and the cortical bone. Therefore, constant Young's moduli are assigned to both the trabecular and the cortical bone. The homogenous assignment of material properties is also called two-material model [33]. While in inhomogeneous assignment, mechanical properties are assigned according to bone density. Based on above discussions, femur is considered as an inhomogeneous isotropic material in this study.

2.3 Age-Related Bon Loss and Osteoporosis

Osteoporosis is a common health problem in the elderly, characterized by a systemic loss of bone mass, strength, and the deterioration of microarchitecture, which increases the possibility of fragility fractures (Figure 2-4B) [71]. Bone mineral density can be assessed with DXA, and osteoporosis is defined by a T-score of less than -2.5, i.e. more than 2.5 standard deviations below the average of a young adult [15]. Multiple factors are involved in the development of osteoporosis. Disruption in bone modeling and remodeling is obviously the main cause of osteoporosis. Adult bone normally is continuously going through bone formation and resorption processes. Bone loss occurs when either bone resorption is too fast or bone formation is too slow, the worst scenario is the combination of the above two aspects. Thus, osteoporosis occurs only when the rate of bone resorption (destruction) exceeds the rate of bone formation (construction). Resorption and formation processes are conducted by the specialized bone-resorbing cells, osteoclasts, and bone-forming cells, osteoblasts (Figure 2-4C).

Osteoporosis is categorized to the primary and secondary form. Primary osteoporosis, the most common form, is due to the typical age-related bone loss. It is further classified as type1 and type2. Secondary osteoporosis is the result of other diseases or conditions that predispose to bone loss and is classified as type3. Type1 or postmenopausal osteoporosis occurs in 5% to 20% of women [72]. The incidence of osteoporosis in women is eight times higher than that in men [73]. Type1 osteoporosis is characterized by increased bone resorption due to osteoclastic activity. Type2 or senile osteoporosis occurs in women or men more than 70 years of age and usually is associated with decreased bone formation. In type2 osteoporosis, masses in trabecular and cortical bone are gradually lost, primarily leading to increased fracture risk of hip, long bone, and vertebral fractures. Type3 or secondary osteoporosis occurs equally in men and women and at any age [74]. Approximately 40% of the total number of osteoporotic fractures observed in clinic are related to secondary osteoporosis [75].

Aging contributes to bone loss in women and men [76]. Normally by aging, the BMD decreases, which contributes to osteoporosis. There is a rapid loss of the trabecular bone in women associated to menopause. But, there is a less loss of the cortical bone in women following the menopause. Generally, bone loss in men is less than in women, however, there is a very similar pattern of slow, age-related bone loss in men as present in women [77].

2.4 Hip Fracture

2.4.1 Hip Fracture Types

Fracture may occur anywhere from the articular cartilage of the hip joint to the femur shaft [78]. Hip fractures are generally classified into intracapsular (femoral neck and head) and extracapsular (intertrochanteric and subtrochanteric). Hip fractures are further assorted into three types based on the anatomical locations: femoral neck (or cervical), intertrochanteric, and subtrochanteric fractures as shown in Figure 2-5 [79]. The femoral neck fractures take place at the femoral neck region between the trochanters and the femoral head. The intertrochanteric fractures occur in the area between the greater trochanter and the lesser trochanter. Subtrochanteric fractures occur below the lesser trochanter.

Not only does the location of the fracture types differ, but also the etiology. It was reported that women with the intertrochanteric fracture have significantly lower BMD than those with the femoral neck fracture [80–82]. Women with intertrochanteric fracture have low BMD especially due to large trabecular bone loss. On the other hand, the femoral neck fracture may not mainly attribute to bone loss and low BMD, but may be related to external causes such as sideways fall [83]. Femoral neck and intertrochanteric fractures are often the result of falls from standing height and impact onto the greater trochanter, particularly for the elderly patients. The subtrochanteric fractures, on the other hand, are typically the result of high energy impacts such as motor vehicle accidents and falls from a height [84]. According to clinical observations, hip fractures at the femoral neck and the intertrochanteric region are more common than the subtrochanteric fractures [85–89].

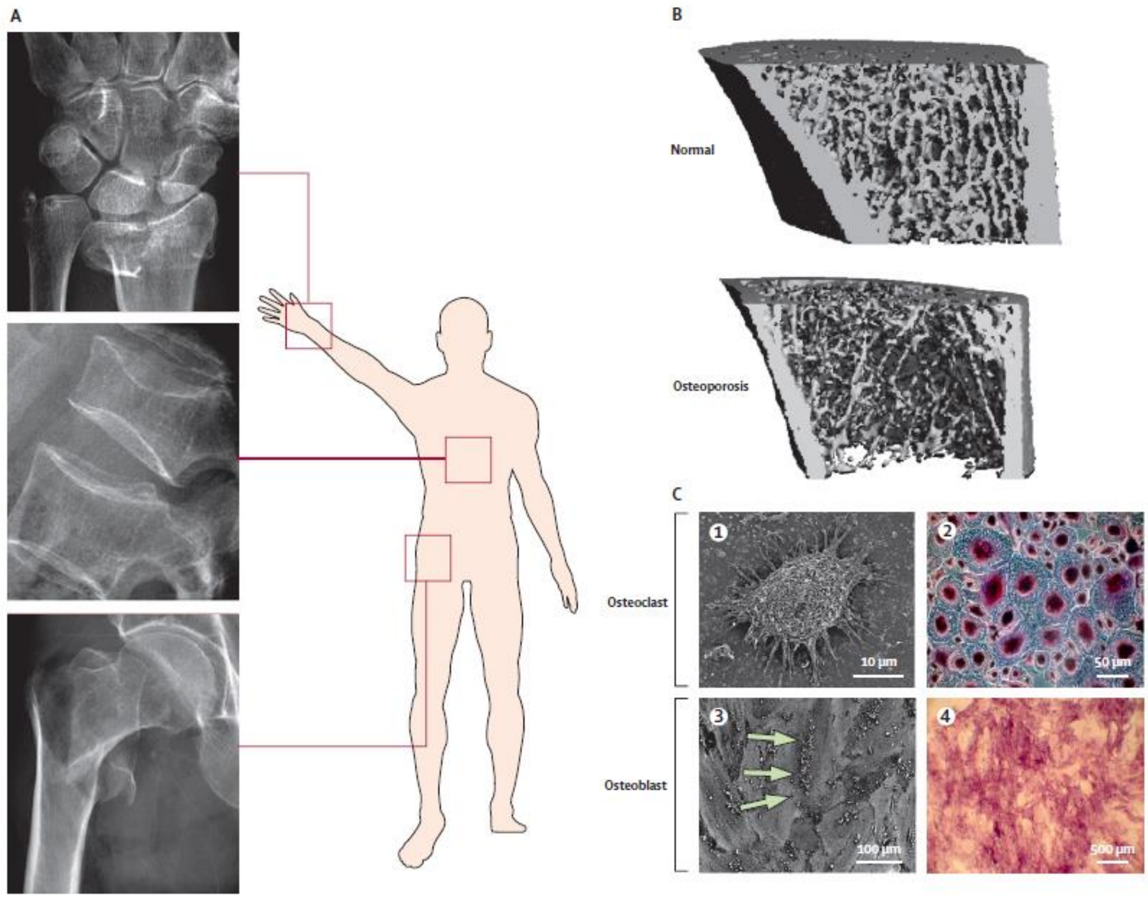

Figure 2-4. Osteoporosis at a glance: (A) fragility fractures of wrist, vertebrae, and hip; (B) comparison of osteoporotic bone and normal bone; (C) bone-resorbing osteoclasts and bone-forming osteoblasts: (1) morphology of osteoclast; (2) tartrate-resistant acidic phosphatase staining of multinucleated osteoclasts; (3) morphology of osteoblasts; (4) alkaline phosphatase staining of osteoblasts [71].

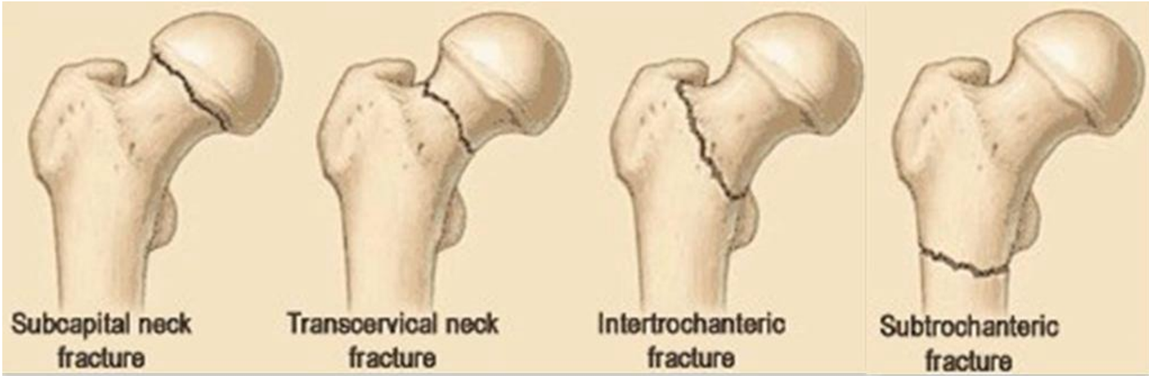

Figure 2-5. Three main types of hip fractures: the femoral neck (or cervical) fractures (subcapital and transcervical fractures), the intertrochanteric fractures, and the subtrochanteric fractures [90] (courtesy of Advanced Orthopedic Specialists).

2.4.2 Mechanics of Hip Fracture

Two major factors contributing the high incidence of hip fractures in the elderly are age-related osteoporosis and accidental falling [91]. Falling plays a more dominant role in causing hip fracture than low BMD, so that falling was responsible for 97% hip fractures [12]. However, only about 5% of falls in the elderly resulted in hip fracture [92].

In the normal walking, the greatest stresses occur in the subcapital and the mid-femoral neck regions [93]. Within these regions, the maximum compressive stresses occur in the inferior surface and smaller magnitude tensile stresses occur in the superior surface of the femoral neck (Figure 2-6a) [93]. Conversely, during the sideways fall, the greatest compressive stresses and strains occur in the superior femoral neck while the lower tensile stresses appear at the inferior region (Figure 2-6b) [93,94]. The maximum magnitude of stresses during a sideways fall is approximately four times greater than those in the normal walking [93]. Due to the high compressive stress in the superior region of the femoral neck during the sideways fall, fracture usually initiates from this region [95,96]. It was found that bone loss in the elderly mainly occurs at the superior aspect of the femoral neck [97], and this same region has been observed to be a site of fracture initiation during ex-vivo experiments under the sideways fall loading, followed by failure in the inferior aspect of the femoral neck or the medial intertrochanteric region [34]. This fragility can be explained by noting that the superior femoral neck only experiences low tensile stresses during regular standing and walking; according to the Wolff's Law, bone in this region tends to weaken over time if alternative loading is not regularly experienced. During a sideways fall impact to the greater trochanter, however, the same area is heavily loaded in compression (Figure 2-6b). The weakened structure is often unable to support the sudden increased load, leading to higher possibility of fracture [98]. This strongly suggests that the superior region of femoral neck has the highest fracture risk and would be more prone to failure than the inferior region and would thus constitute a relatively weak region in the femoral structure during the sideways fall.

The mechanism leading to fracture initiation in the superior region of femoral neck under compression during the sideways fall is still a topic of argument. Mayhew et al. [96] suggested that local buckling of the thinning cortical shell may be an important factor of fractures, because this area of the neck often becomes thinner with age. Turner [98], however, disagreed to the occurrence of shell buckling in the femoral neck, as it is filled with the trabecular bone and marrow, making it a far more complex and also stronger structure than an empty shell. Fractures have been observed to initiate in areas that are subjected to compression during the sideways fall, where the cortical bone is thinner [34], a finding that potentially supports the buckling hypothesis as the mechanism leading to hip fracture.

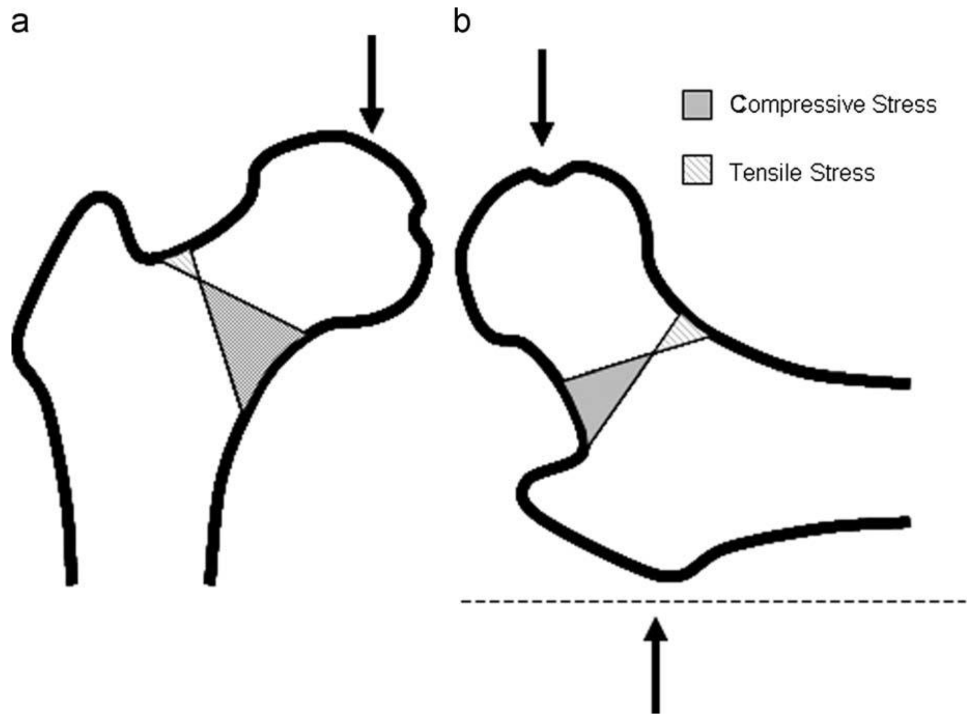

Figure 2-6. Stress distributions in the femoral neck region during (a) the normal gait and (b) the sideways fall. During the normal gait, the greatest compressive stress occurs in the inferior region while during the sideways fall, the superior region receives the greatest compressive stress [34].

2.5 Finite Element Analysis of Hip Fracture

The finite element method, an advanced computational method for structural stress analysis, was introduced to orthopedic biomechanics in 1972 to assess stresses in human bones [99]. Since then, this method has been applied increasingly for failure analyses of bones, bone-prosthesis structures, and bone fixation devices. The use of FE modeling to specifically investigate hip fracture risk of the intact femur started in the early 1990s with the investigation by Lotz et al. [42,43]. They used data from QCT images to create models of the femur and load them in both the single-leg stance and the sideways fall configuration.

The aim of FE analyses was to assess bones under physiological loading to find relationships between load carrying functions and morphology of bones, and to optimize designs of fixation techniques of implants [100]. From a biomechanical viewpoint, an approach that is able to provide complex geometries and to accurately represent the heterogeneous distribution of material properties may provide accurate assessment of bone strength, compared to the BMD-based methods. In this regard, there is an increasing interest in the use of finite element method to assess bone biomechanical behavior. For the FE analyses, different commercially available software such as ANSYS and ABAQUS or in-house computer codes developed using MATLAB, C, and etc. are usually used. Since 1972, the finite element method, along with the newly developed digital imaging techniques, has been actively used to evaluate bone strength and to study osteoporosis. Generally, the implemented image-based FE models can be divided into two categories, i.e., three-dimensional (QCT-based) and two-dimensional (DXA-based), which are described in the following.

A number of DXA-based FE models were developed for subject-specific assessment of hip fracture risk [29–31]. The general procedure to construct a DXA-based FE model is first to extract the 2-D geometry of femur from the DXA image using image processing programs. The obtained geometry is meshed and the inhomogeneous material properties are assigned. The loading and boundary conditions are then applied to the constructed FE model to obtain the strain and stress distributions. Whereas the DXA is a 2-D image, the overlapped part of the femoral head with the pelvis is used to calculate the fracture risk while the BMD of the femoral head is overestimated from the DXA image. It means that the actual fracture risk is higher than what is calculated by the DXA-based FE models. The other issue in estimating the overall fracture risk is that a high stress is generated on the shaft due to the applied boundary conditions on the distal end of the femur. These stresses are used in predicting fracture risk, but they are not realistic because the boundary conditions are not properly applied and cannot faithfully simulate the single-leg stance and the sideways fall configuration. The mentioned limitations should be removed to improve the DXA-based FE models. Although DXA-based FE models are 2-D, they are preferred in clinics because the radiation dosage used in the DXA scanning is much lower than that used in the QCT scanning.

DXA scanning technique has certain limitations, namely, a 3-D object is projected onto a 2-D plane and the depth information is lost, but the QCT scanning technique does not have these limitations. For the complex geometry of bones, a QCT-based finite element model, which is a 3-D model, is principally more precise in estimating strength and fracture risk. Over the past 20 years, a number of subject-specific QCT-based FE models of human femur have been developed to evaluate bone strength, stress, strain, failure load, fracture location, and fracture risk during the single-leg stance and the sideways fall [32–40].

3-D FE model of bone is generated directly from QCT image and then material properties are assigned based on CT numbers using image processing programs such as Mimics (Materialise, Leuven, Belgium). Loading and boundary conditions, simulating the single-leg stance or the sideways fall configuration, are then applied to the constructed 3-D FE model using commercially available software such as ANSYS and

ABAQUS or in-house developed computer codes. One group of the 3-D FE models are constructed directly from voxels of QCT scans. The main advantage of voxel-based FE models is that they can be generated extremely fast. However, voxel elements create jagged edges due to protruding vertices of the cubes at the surface, resulting in errors in the computed local stresses and strains. High-resolution peripheral QCT (HR-pQCT) is a newly developed in-vivo clinical imaging modality. It can assess the 3-D microstructure of trabecular and cortical bone and is suitable as an input for microstructural finite element analysis to evaluate bone mechanical properties [101–103].

Therefore, in this research, QCT-based FE model was established to assess hip fracture risk using the strain energy criterion. In the next chapter, construction of the required QCT-based FE model will be explained in detail.

Chapter 3

Assessment of Hip Fracture Risk using QCT-based Finite Element Model

The proposed methodology for assessment of hip fracture risk at the three critical cross-sections of femur using the strain energy criterion determined from QCT-based finite element model is shown in Figure 3-1. The procedure is explained in detail in the following.

3.1 QCT-based Finite Element Model

3.1.1 QCT-Scan of Femur

The purpose of this study is to accurately assess hip fracture risk, so, a 3-D finite element model of subject's femur is required to achieve it. The 3-D model can be constructed from the subject's femur QCT images. QCT slices are produced using multiple scanners with a set of proper acquisition and reconstruction parameters. A sample set of QCT images are shown in Figure 3-2. Slice thickness of 1mm is commonly used. The scanned QCT images are stored in the format of Digital Imaging and Communications in Medicine (DICOM), which can be used for the construction of a 3-D FE model. A proper segmentation is done to separate the femur for constructing the 3-D model. Each voxel in the QCT scan has an intensity (or grey scale) that is expressed as Hounsfield Unit (HU), which is correlated to bone density [104,105].

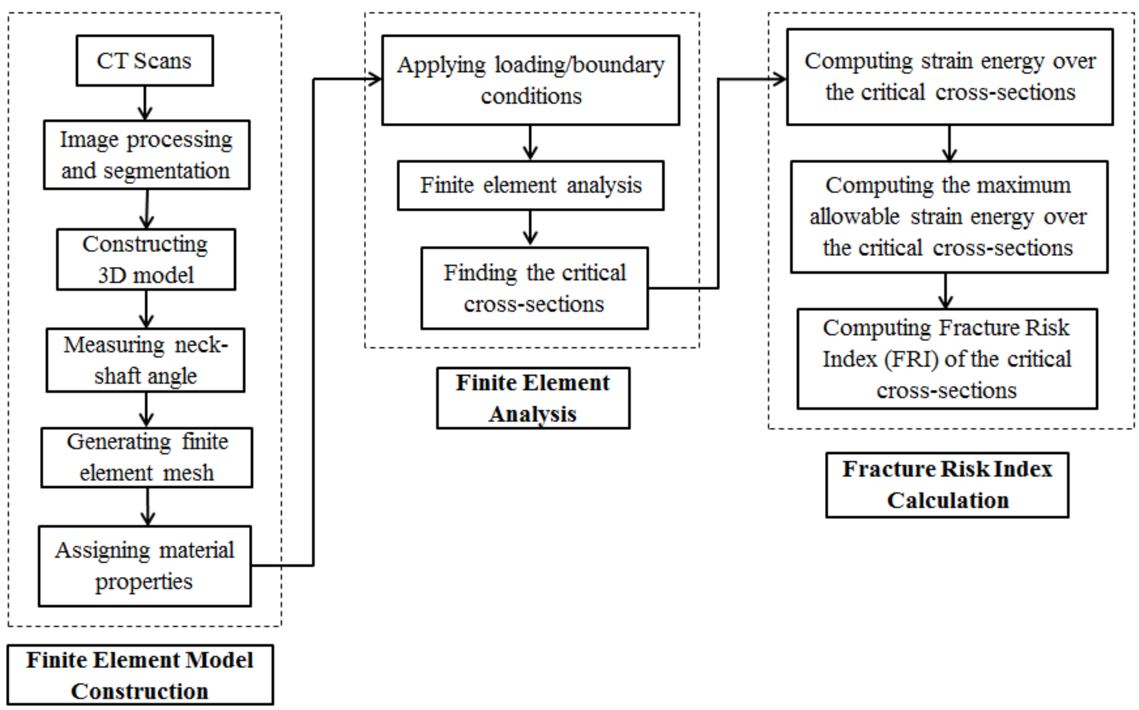

Figure 3-1. The proposed methodology for calculating hip fracture risk index using the strain energy criterion.

3.1.2 Generation of Finite Element Mesh

In the first step, the geometrical model of the femur is generated from clinical QCT images using Mimics (Materialise, Leuven, Belgium). QCT images (in DICOM format) are imported to Mimics for segmentation (Figure 3-2) and construction of 3-D geometric model of the femur (Figure 3-3). With the 3-D geometric model, a FE mesh is generated using the 3-matic module in Mimics (Figure 3-4). The 4-node linear tetrahedral element SOLID72 in ANSYS was used in this study. SOLID72 is well developed to simulate irregular and complex geometric models such as those produced from various CAD/CAM systems. The element has four nodes with six degrees of freedom at each node: translations in the nodal x, y, and z directions and rotations about the nodal x, y, and z directions. The element also has stress stiffening capability [106]. The geometry, node locations, and the coordinate system for this element are shown in Figure 3-5.

To investigate model convergence, FE models with different maximum element edge lengths were created. For each FE model, displacement was calculated under the same loading and boundary conditions. The maximum element edge length that produced converged finite element solutions was obtained and used in all the rest FE simulations.

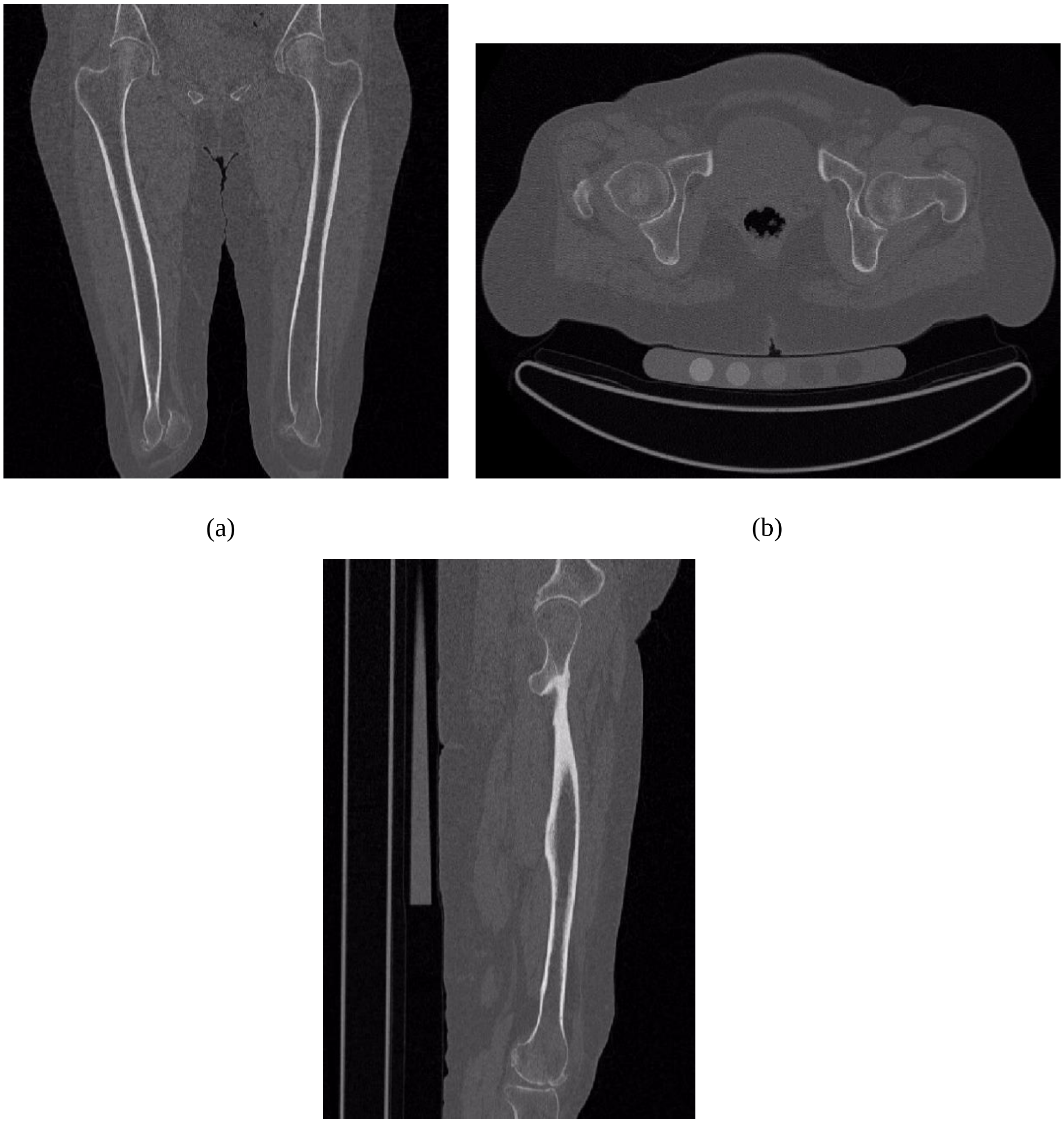

(a) (b)

(c)

Figure 3-2. QCT image of femur (in DICOM format) imported to Mimics in the three viewing planes: (a) coronal plane, (b) transverse plane, and (c) sagittal plane.

Figure 3-3. 3-D model generated from QCT image.

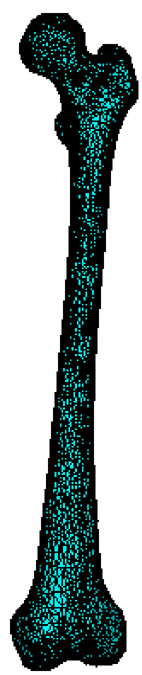

Figure 3-4. A 3-D finite element model.

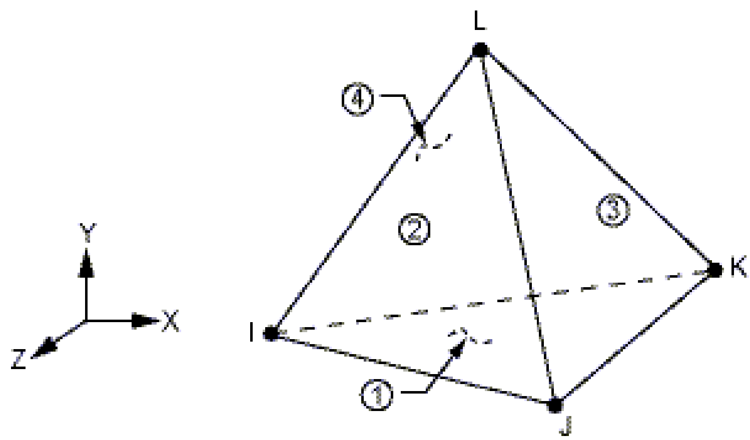

Figure 3-5. SOLID72, a 3-D 4-node linear tetrahedral structural solid element [106].

3.1.3 Assignment of Material Properties

To construct a more faithful FE model, bone material properties are considered inhomogeneous and isotropic in this study. Information on the inhomogeneous isotropic mechanical properties of the bone can be derived from the CT data using a mathematical relationship between the CT numbers and the mechanical properties of bone. The following empirical equation was used to determine bone ash density (ρ_{ash}) according to the HU number [38,107]:

$$\rho_{ash} = 0.04162 + 0.000854\,HU \quad (g/cm^3) \tag{3.1}$$

Equation (3.2) and Equation (3.3), derived by Keller [108], were respectively used to assign Young's modulus (E) and the yield stress (σ_Y) according to the bone ash density:

$$E = 10500\rho_{ash}^{2.29} \quad (MPa) \tag{3.2}$$

$$\sigma_Y = 116\rho_{ash}^{2.03} \quad (MPa) \tag{3.3}$$

A constant Poisson's ratio ($\nu = 0.4$) was considered [41,109,110]. To assign material properties, elements are grouped into several discrete material bins using Mimics (Materialise, Leuven, Belgium), which are used to approximately represent the continuous distribution of the inhomogeneous bone mechanical properties. To determine the maximum number of material bins, convergence study was performed. Models with different material bins were created for convergence study. For each FE model, displacement was calculated under the same loading and boundary conditions. The maximum number of material bins that generated converged finite element solutions was obtained. Figure 3-6 displays the inhomogeneous distribution of bone density.

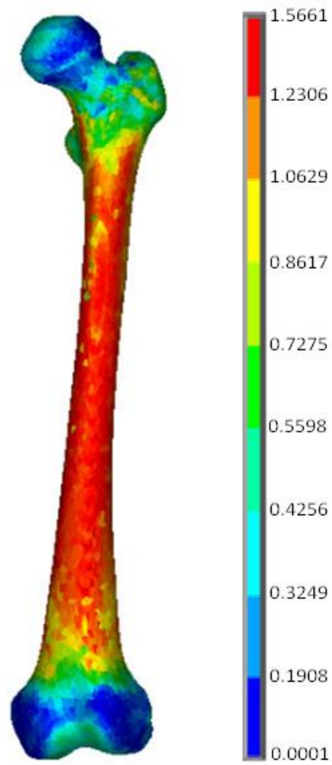

Figure 3-6. Inhomogeneous distribution of bone density (g/cm^3).

3.1.4 Loading and Boundary Conditions

For a precise assessment of hip fracture risk during the single-leg stance and the sideways fall, loading and boundary conditions simulating the single-leg stance and the sideways fall configuration are required in the FE model. To simulate the single-leg stance statue, 2.5 times of the patient's body weight was applied as a distributed load on the femoral head [97] and femur was fixed at the distal end [37,41] (see Figure 3-7a):

$$F_{Stance} = 2.5w \quad (N) \tag{3.4}$$

where w is the subject's body weight in Newton (N). To simulate sideways fall configuration, the distal end of femur were completely fixed and the surface of femoral head were fixed in the loading direction (Figure 3-7b) [39,40]. The peak impact force during the sideways fall on the greater trochanter can be estimated based on the previous studies on the kinematics and dynamics of the falls from the standing height [97,111]. The impact force during the sideways fall acting on the greater trochanter (Figure 3-7b) is given by [97,111]:

$$F_{Impact} = 8.25w(\frac{h}{170})^{\frac{1}{2}} \quad (N) \tag{3.5}$$

where h is the body height of the subject in centimeter (cm).

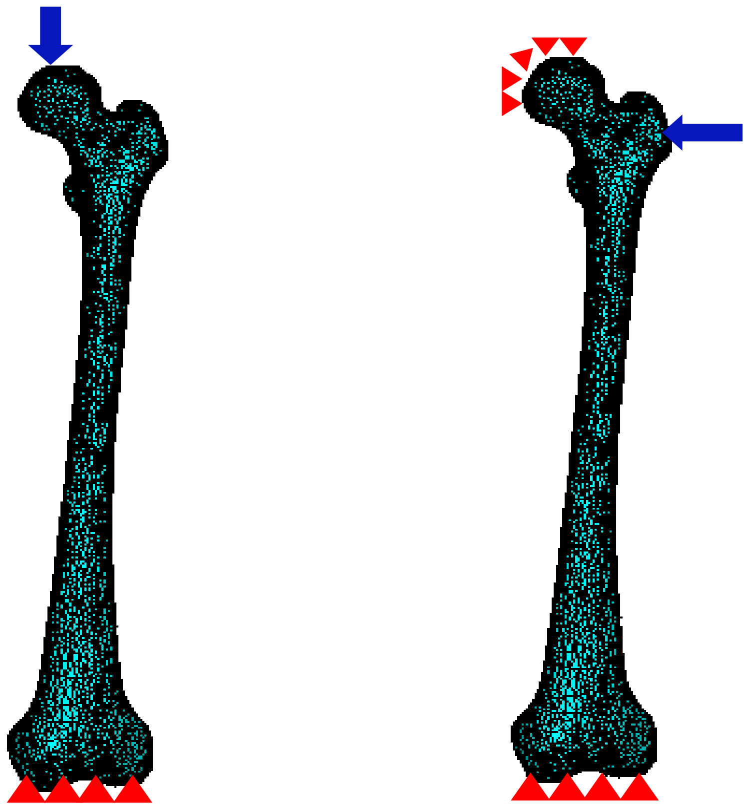

(a) (b)

Figure 3-7. Application of loading and boundary conditions during (a) the single-leg stance and (b) the sideways fall.

3.2 Finite Element Analysis using ANSYS

A finite element model of femur with the assigned material properties output from Mimics was imported to ANSYS for finite element analysis. Loading and boundary conditions on the greater trochanter, the femoral head, and the distal end of femur, simulating the single-leg stance and the sideways fall configuration, were applied to the nodes located on the respective boundaries (Figure 3-7a and Figure 3-7b). All loading and boundary conditions were applied using ANSYS Parametric Design Language

(APDL) codes. After importing the QCT-based FE model and applying the loading and boundary conditions, finite element analysis was performed and finite element solutions were obtained. In all the analysis, the nodal displacements, von Mises stress and strain, tensile and compressive stresses were obtained for each subject.

After solving the FE model of each subject, stress and strain distributions at the three critical cross-sections of femur were obtained. APDL codes were written in order to extract the boundary of the three critical cross-sections, the nodal displacements, the coordinates of nodes from the FE model, as well as information on element's density, corresponding nodes, and nodes connectivity. The results extracted by the APDL codes were used in next steps to calculate FRI at the three critical cross-sections of femur.

3.3 Detection of the Three Critical Cross-Sections on the Femur

The smallest femoral neck cross-section (SFN CS), the intertrochanteric cross-section (IntT CS), and the subtrochanteric cross-section (SubT CS) are the three critical cross-sections on the femur that usually have the highest fracture risk (Figure 3-8). To determine the smallest femoral neck cross-section and the intertrochanteric cross-section, neck-shaft angle is needed. The neck-shaft angle is the angle between the femoral neck axis and the femoral shaft axis. This angle traditionally is measured on conventional radiography images, or using 2-D images projected from CT/MRI scans. Although these methods are popular, but they are based on over simplification of the real 3-D anatomy and may lead to large errors and inaccurate results [112–114]. In this study, the neck-shaft angle was measured using a 3-D measurement technique based on fitting functions. In this technique, the shapes of particular parts of the femur are approximated using geometric entities such as circle, cylinder, sphere, and etc., which are well-fitted to the actual anatomy, and the geometrical relationships between these entities are obtained to estimate the neck-shaft angle.

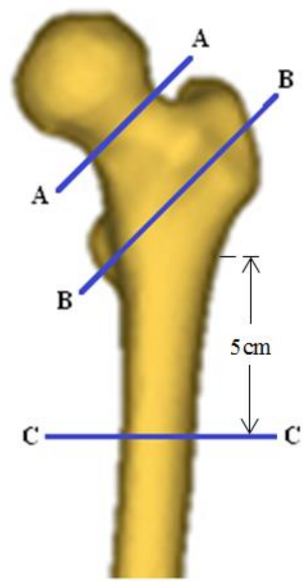

Figure 3-8. Three critical cross-sections of femur: the smallest femoral neck cross-section (A-A), the intertrochanteric cross-section (B-B), and the subtrochanteric cross-section (C-C).

First, a sphere is fitted to the femoral head (Figure 3-9a) to obtain the position of the joint's centre of rotation, which is also the femoral head centre. Then, the femoral neck axis and the femoral shaft axis are identified by applying the "fit ruled surface direction" function on the femoral neck and shaft (Figure 3-9b and Figure 3-9c) [115]. All fitting functions were applied using the 3-matic module in Mimics. The neck-shaft angle was also measured by the 3-matic module of Mimics (Figure 3-10).

With the femoral neck-shaft angle, the intertrochanteric cross-section and the smallest femoral neck cross-section were found using in-house computer codes. The intertrochanteric cross-section is chosen the cross-section that has the largest area in the intertrochanteric region. The smallest femoral neck cross-section is chosen the cross-section with the smallest area in the neck region [116–118]. By using APDL codes, perpendicular planes on the femoral neck axis were determined and then areas of planes were obtained. The planes with the smallest and largest areas were chosen respectively as the smallest femoral neck cross-section and the intertrochanteric cross-section. The subtrochanteric cross-section is considered five centimeter below the lesser trochanter (Figure 3-8) [78].

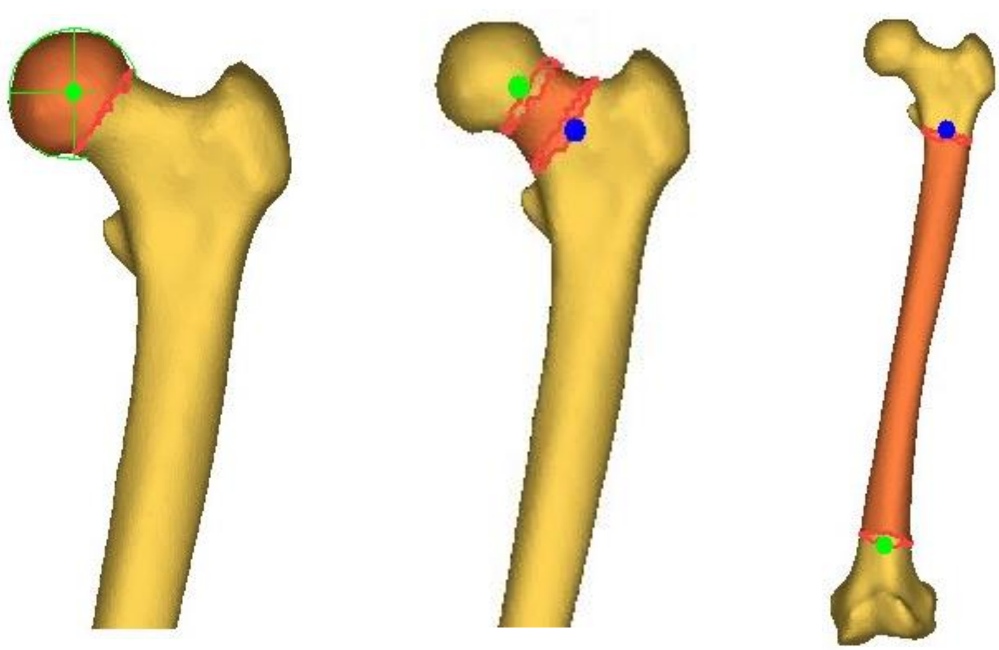

(a) (b) (c)

Figure 3-9. Fitting functions: (a) fit sphere function on the femoral head, (b) fit ruled surface direction function on the femoral neck, and (c) fit ruled surface direction function on the femoral shaft.

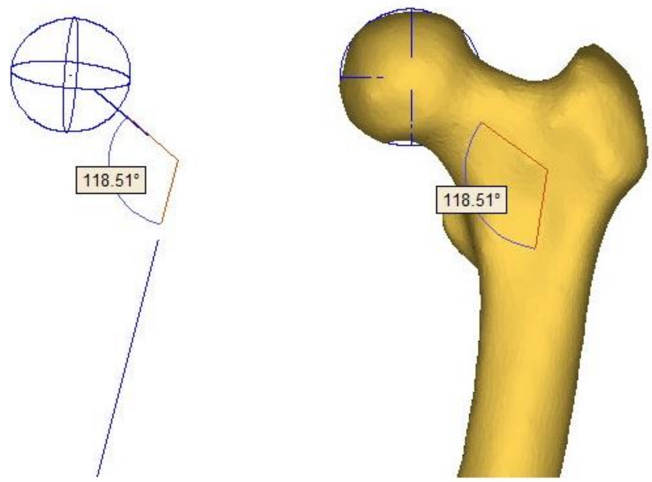

Figure 3-10. Neck-shaft angle measured by the fitting functions in the 3-matic module of Mimics.

3.4 Hip Fracture Risk Index at the Three Critical Cross-Sections

3.4.1 Femur Failure Criterion based on Cross-Section Strain Energy

Based on the previous discussion on the bone failure mechanism and microstructure, the strain energy criterion is theoretically the best failure criterion for hip fracture risk assessment. Therefore, hip fracture risk index was defined based on this criterion in this study. The criterion requires the determination of the strain energy associated with changes in shape and volume of the material [119]. According to this criterion, a femoral cross-section will not crack as long as the strain energy induced by external forces would not exceed the ultimate strain energy that the cross-section is able to sustain until bone yielding. The strain energy (U) stored at a cross-section is given by:

$$U = \int\int \hat{U} dA \tag{3.6}$$

where $\hat{U}$ is the strain energy density. The strain energy density is the scalar product of the stress vector (σ) and the strain vector (ε):

$$\hat{U} = \frac{1}{2}\sigma^T . \varepsilon \tag{3.7}$$

The strain energy of a cross-section at the yielding point (U_Y) is given by:

$$U_Y = \int\int \hat{U}_Y \, dA \tag{3.8}$$

where $\hat{U}_Y$ is the strain energy density at the yielding point:

$$\hat{U}_Y = \frac{1}{2}\sigma_Y \varepsilon_Y \tag{3.9}$$

where σ_Y and ε_Y are respectively the yield stress and the yield strain of the bone. Thus, based on the strain energy criterion, the femoral cross-section will not crack if $U < U_y$.

3.4.2 Strain Energy at the Three Critical Cross-Sections

The strain energy at the three critical cross-sections of femur induced by the applied forces was computed using in-house developed MATLAB codes and the data extracted by APDL codes from the obtained finite element solutions. The plane boundaries of the three critical cross-sections, extracted from the finite element mesh, were imported to MATALB to generate a 2-D mesh for calculating the cross-section strain energy. Figure 3-11 shows the generated triangle elements over the smallest femoral neck cross-section, the intertrochanteric cross-section, and the subtrochanteric cross-section.

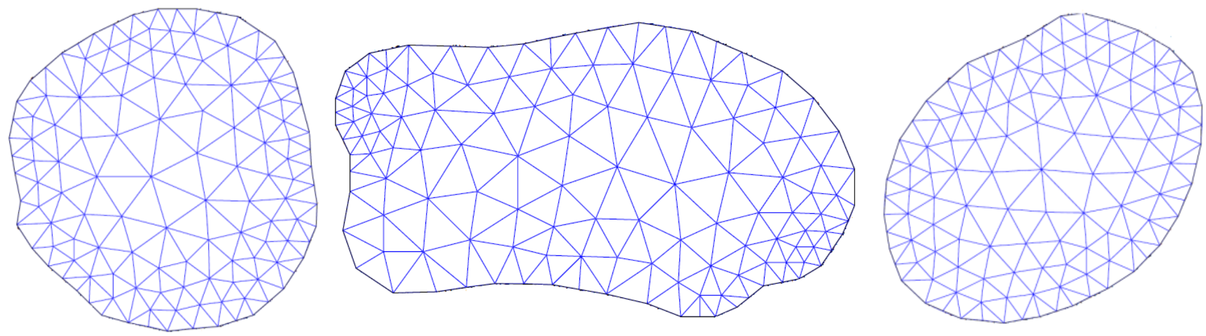

(a) (b) (c)

Figure 3-11. Generated triangle elements over (a) the smallest femoral neck cross-section, (b) the intertrochanteric cross-section, and (c) the subtrochanteric cross-section.

The strain energy at the three critical cross-sections induced by the applied forces is the sum of strain energy in all the triangle elements, i.e.:

$$U = \sum_{i=1}^{m} U_e \tag{3.10}$$

where U_e is the strain energy in an element (e) induced by the applied forces and m is the number of triangle elements created over the concerned cross-sections. Gaussian integration method was used to calculate the strain energy in an element (e). Integration points in each triangle element were determined using in-house MATLAB codes. By using Gaussian integration method, the strain energy of Element e induced by the applied forces is calculated as:

$$U_e = \int\int \widehat{U}_e \, dA \approx \sum_{i=1}^{n} W_i |J| \, \widehat{U}_i \tag{3.11}$$

where $\widehat{U}_e$ is the strain energy density of a triangle element (e); $\widehat{U}_i$ is the strain energy density at the integration points of in Element e; W_i is the weight at the integration points; $|J|$ is determinant of the Jacobean matrix of the triangle element; and n is the number of integration points over the triangle element (integration domain). The strain energy density at an integration point (i) was determined from the finite element solutions obtained by the 3-D QCT-based FE model, i.e.:

$$\widehat{U}_i = \frac{1}{2}\{\sigma\}^T\{\varepsilon\} \tag{3.12}$$

where $\{\sigma\} = [D]\{\varepsilon\}$ and $\{\varepsilon\} = [B]\{d\}$. The strain energy density at each integration point can be expressed by the finite element solutions as:

$$\widehat{U}_i = \frac{1}{2}\{d\}_e^T\,[B]_e^T[D]_e[B]_e\{d\}_e \tag{3.13}$$

where $\{d\}$ is the displacement vector consisting of displacements at the element nodes of the tetrahedral element where the integration point is located; matrix $[B]$ is the derivatives of shape functions of the tetrahedral element; and $[D]$ is the material property matrix of the tetrahedral element:

$$[D]_e = \frac{E}{(1+\nu)(1-2\nu)}\begin{bmatrix} 1-\nu & \nu & \nu & 0 & 0 & 0 \\ \nu & 1-\nu & \nu & 0 & 0 & 0 \\ \nu & \nu & 1-\nu & 0 & 0 & 0 \\ 0 & 0 & 0 & \frac{1}{2}-\nu & 0 & 0 \\ 0 & 0 & 0 & 0 & \frac{1}{2}-\nu & 0 \\ 0 & 0 & 0 & 0 & 0 & \frac{1}{2}-\nu \end{bmatrix} \tag{3.14}$$

where Poisson's ratio is constant ($\nu = 0.4$) and Young's modulus is function of the bone density obtained from Equation (3.2). For each integration point, its Young's modulus is calculated according to the bone density at the point, which is the density of the tetrahedral element where the integration point is located.

3.4.3 The Maximum Allowable Strain Energy of the Three Critical Cross-Sections

The maximum allowable strain energy of the three critical cross-sections of femur was also computed using in-house MATLAB codes and the data extracted by APDL codes from the obtained finite element solutions. The maximum allowable strain energy (or the yield strain energy) of the three critical cross-sections is the sum of the yield strain energy in all the triangle elements:

$$U_Y = \sum_{i=1}^{m} U_Y^e \tag{3.15}$$

where U_Y^e is the yield strain energy in Element e and m is the number of triangle elements created over the concerned cross-sections. The Gaussian integration method was also used to calculate the maximum allowable strain energy in each triangle element. The maximum allowable strain energy that a triangle element (e) can sustain is given by:

$$U_Y^e = \int\int \widehat{U}_Y^e \, dA \approx \sum_{i=1}^{n} W_i |J| \, \widehat{U}_{Yi} \tag{3.16}$$

where $\widehat{U}_Y^e$ is the yield strain energy density in a triangle element (e); n is the number of integration points over the triangle element (integration domain); and $\widehat{U}_{Yi}$ is the yield strain energy density at an integration point (i) and is calculated as:

$$\widehat{U}_{Yi} = \frac{1}{2}\sigma_{Yi}\varepsilon_{Yi} = \frac{\sigma_{Yi}^2}{2E_i} \tag{3.17}$$

where σ_{Yi} and E_i are respectively the yield stress and Young's modulus at the integration point. Both of them are functions of bone density, which is the density of the tetrahedral element where the integration point is located, as given in Equation (3.2) and Equation (3.3).

3.4.4 Hip Fracture Risk Index at the Three Critical Cross-Sections

Hip fracture risk index at the three critical cross-sections is defined as the ratio of the strain energy induced by the applied forces to the maximum allowable strain energy of the femur over the concerned cross-sections:

$$\eta_{SEN} = \frac{\mathrm{U}}{\mathrm{U_Y}} \tag{3.18}$$

where η_{SEN} is the fracture risk index at one of the three critical cross-sections of femur based on the strain energy criterion; and U and $\mathrm{U_Y}$ are respectively obtained from Equation (3.10) and Equation (3.15).

3.5 Enrollment of Clinical Cases

Information of 60 clinical cases (30 females and 30 males), including QCT image, height, body weight, and age, was acquired from the Winnipeg Health Science Centre in an anonymous way under a human research ethics approval. Statistical information of the clinical cases is listed in Table 3-1. The age scope of the subjects is between 50 and 82 years (average of 65 years) and their heights and body weights are respectively in range of 149-193.2 centimeters and 51.7-126.6 kilograms. For each case, BMI was calculated. A QCT-based FE model was constructed for each subject; loading and boundary conditions simulating the single-leg stance and the sideways fall configuration were separately applied to the FE model; FE analysis was then performed for each subject. Based on the previously described methodology, FRIs were calculated at the three critical cross-sections of femur for each subject.

Table 3-1. Statistical information of the 60 clinical cases.

	Age (years)	Height (cm)	Body weight (kg)	BMI (kg/m^2)
Range	50-82	149-193.2	51.7-126.6	18.83-43.36
Average	65	169.86	81.94	28.36

Chapter 4

Results and Discussions

4.1 Verification of In-House Computer Codes

To verify the proposed methodology for calculating the hip FRI using the cross-section strain energy criterion, FRI at the fixed-end cross-section of a cantilever beam (Figure 4-1) was computed using this methodology. The obtained FRI was compared with that computed using the von Mises stress criterion. A cantilever beam with the geometric dimensions shown in Figure 4-1 was considered and a vertical force (F) was applied on its free end. The beam is made of Stainless Steel (ASTM-A-441) with the following mechanical properties:

$$E = 200\ GPa$$

$$v = 0.3 \tag{4.1}$$

$$\sigma_Y = 320\ MPa$$

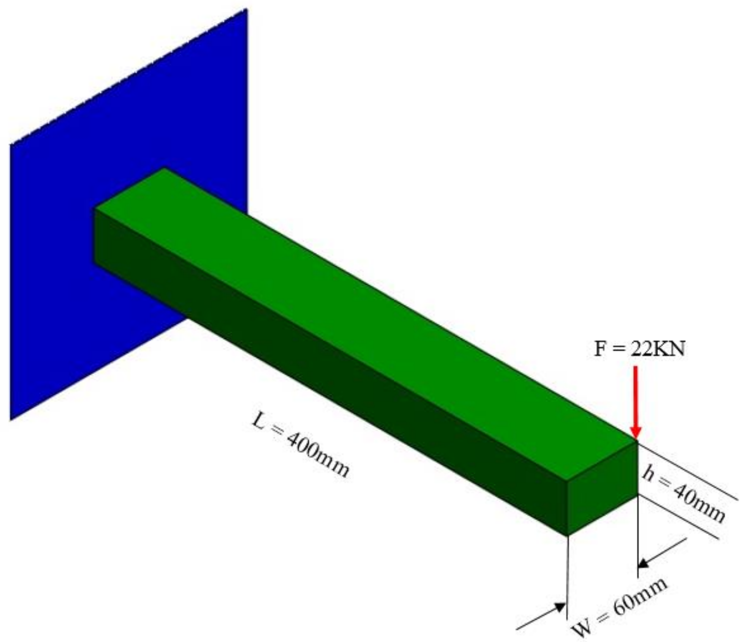

Figure 4-1. A cantilever beam, its geometric dimensions, and the applied force.

FRI at the fixed-end cross-section was considered for the comparison. Triangle elements were generated over the cross-section using in-house MATLAB codes (Figure 4-2). The cross-section strain energy, induced by the applied force, and the maximum allowable strain energy (or the yield strain energy) of the fixed cross-section were computed using the in-house MATLAB codes. The FRI based on the strain energy criterion (η_{SEN}) was defined as the ratio of the strain energy of the fixed-end cross-section to its maximum allowable strain energy (Equation (3.18)).

The maximum von Mises stress (σ_{vM}) of the fixed-end cross-section, induced by the applied force, was obtained using ANSYS (Figure 4-3). The FRI based on the von Mises stress criterion (η_{vM}) was defined as the ratio of the maximum von Mises stress of the fixed-end cross-section to its maximum allowable stress (or yield stress):

$$\eta_{vM} = \frac{\sigma_{vM}}{\sigma_Y} \tag{4.2}$$

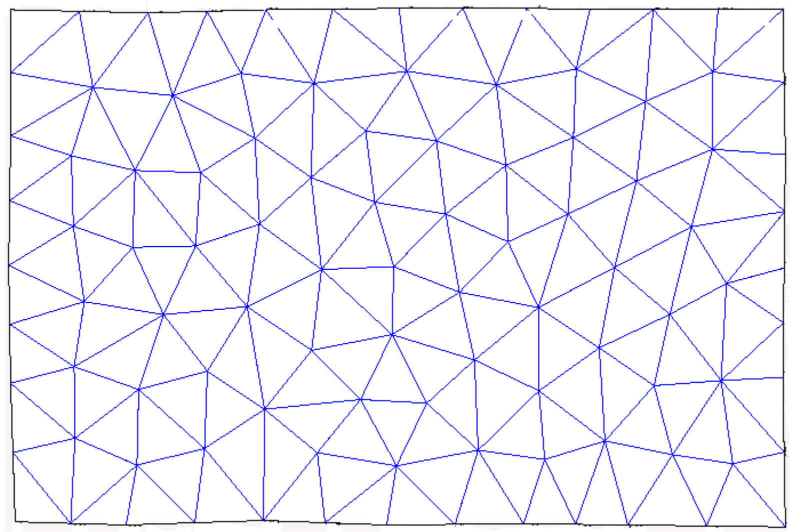

Figure 4-2. Generated triangle elements over the fixed-end cross-section of the cantilever beam.

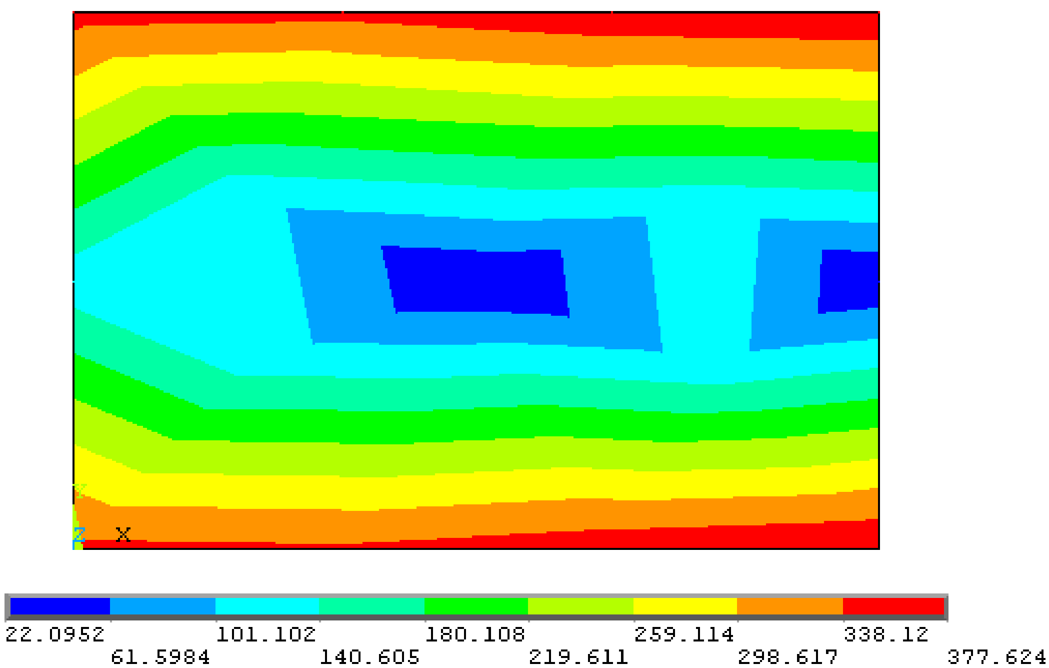

Figure 4-3. The von Mises stress (MPa) distribution at the fixed-end cross-section of the cantilever beam.

The strain energy induced by the applied force, the maximum allowable strain energy, and the FRI at the fixed-end cross-section using the strain energy criterion are shown in Table 4-1. Table 4-1 also shows the maximum von Mises stress induced by the applied force, the yield stress (which is the yield stress of the material used), and the FRI at the fixed-end cross-section based on the von Mises stress criterion. There is no significant difference between the FRIs computed using these two criteria (Table 4-1), which indicates the validity of the proposed methodology and in-house computer codes in calculation of FRIs at the three critical cross-sections of femur using the strain energy criterion. In this regard, an experimental set-up is needed to draw a strong conclusion on the accuracy of the proposed methodology; however, establishing an experimental set-up will be considered in future development.

Table 4-1. Comparison of FRIs at the fixed-end cross-section of the cantilever beam computed using the strain energy and the von Mises stress criteria.

	Strain energy criterion			von Mises stress criterion		
	U (J)	U_Y (J)	η_{SEN}	$\sigma_{vM}(MPa)$	$\sigma_Y(MPa)$	η_{vM}
	755.16	606.32	1.24	377.62	320	1.18
Relative error (%) between η_{SEN} and η_{vM}	5.08					

4.2 Convergence Studies

4.2.1 Element Size in Femur Finite Element Analysis

The convergence of finite element solutions is usually achieved by refining the finite element mesh with the same loading and boundary conditions. The displacement at a predefined point is monitored to judge if a convergence has been achieved, or not (Figure 4-4). The results of the convergence study showed that the displacements did not change significantly for the FE models with the maximum element edge length lower than 8 mm, meaning that a convergence was achieved with the above maximum element edge length. Therefore, in the construction of all femur FE models, the maximum element edge length was set to 8mm.

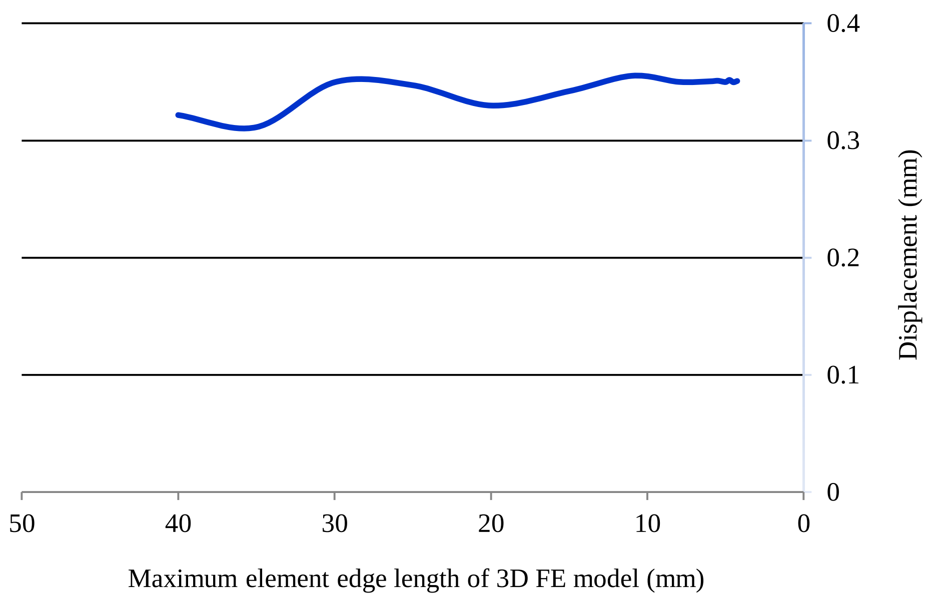

Figure 4-4. Convergence study on the maximum element edge length (mm) of 3-D FE model of femur.

4.2.2 Inhomogeneous Material Properties Assignment

For convergence study in assigning the inhomogeneous material properties, 3-D femur FE models with different material bins were created. For each FE model with different material bins, the maximum displacement at the smallest femoral neck cross-section was monitored under the same loading and boundary conditions. Data on the displacement were compared among the FE models with different material bins (Figure 4-5). The results of the convergence study showed that the displacement did not change significantly in the FE models with the number of material bins higher than 50. Therefore, in the assignment of femur inhomogeneous material properties, 50 discrete material bins were considered.

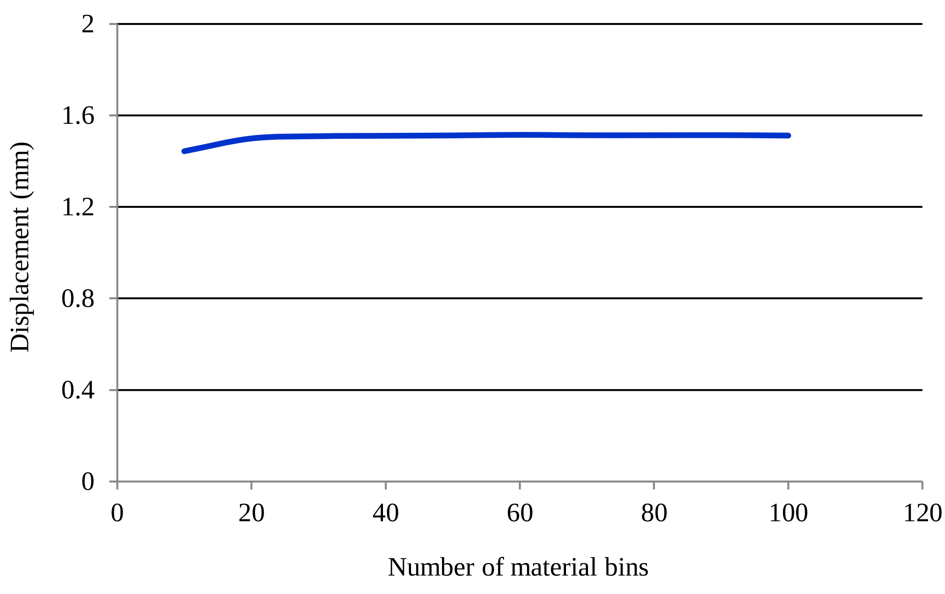

Figure 4-5. Convergence study on the number of material bins for the inhomogeneous material properties assignment.

4.2.3 Element Size in Calculating Cross-Section Strain Energy

Convergence study was performed on the maximum element edge length of the triangle elements generated over the three critical cross-sections of femur. The triangle elements were generated over the smallest femoral neck cross-section with different maximum element edge lengths. The FRI at this cross-section with different maximum element edge lengths was computed under the same loading and boundary conditions. The results of the convergence study showed that the FRI did not change significantly at the smallest femoral neck cross-section with the maximum element edge length lower than 5mm (Figure 4-6). Therefore, the maximum element edge length was set to 5mm for the triangle elements generated over the smallest femoral neck cross-section, the intertrochanteric cross-section, and the subtrochanteric cross-section of femur.

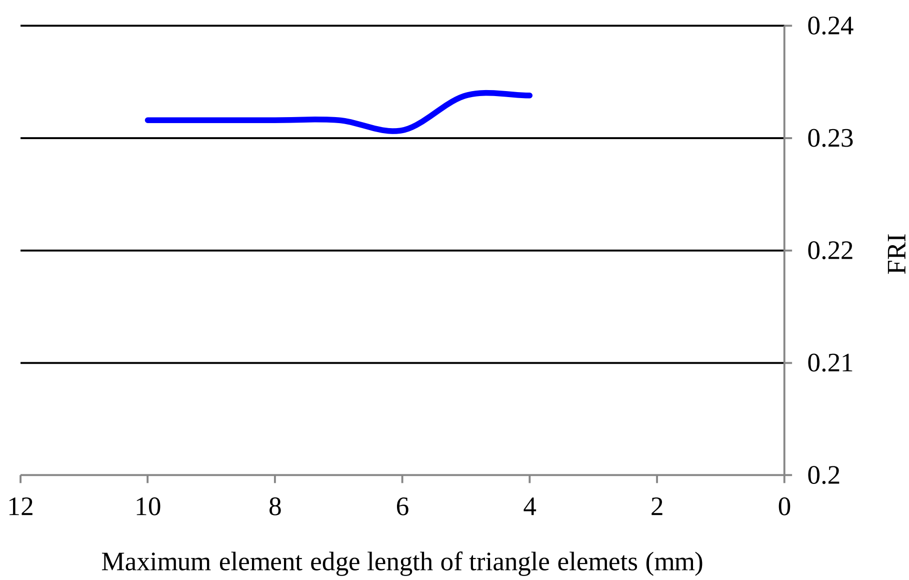

Figure 4-6. Convergence study on the maximum element edge length (mm) of the triangle elements generated over the three critical cross-sections of femur.

4.2.4 Number of Integration Points in Calculating Cross-Section Strain Energy

The effect of the number of integration points over the triangle elements on the calculated FRI was investigated. FRI at the smallest femoral neck cross-section was computed for 5 clinical cases with different number of integration points. The relative errors between the FRIs attained with 3 and 7 integration points are shown in Table 4-2. As it can be seen, the errors are not significant. Therefore, the 3-points integration rule was used in this study by considering its less computational time.

Table 4-2. FRI at the smallest femoral neck cross-section for 5 clinical cases obtained by different number of integration points.

Case No.	FRI		Relative error (%)
	3 integration points	7 integration points	
1	0.239	0.2416	1.07
2	0.6898	0.6975	1.1
3	0.2966	0.2976	0.33
4	0.8885	0.899	1.16
5	1.1482	1.1701	1.87

4.3 Stress Patterns at the Three Critical Cross-Sections

The results of the finite element analyses showed that during the single-leg stance, the tensile stress (σ_1) in the superior region of the femoral neck is higher than that in the inferior region (Figure 4-7a and Figure 4-9a); and the compressive stress (σ_3) in the inferior region is higher than that in the superior region (Figure 4-7b and Figure 4-9b). Conversely, during the sideways fall, the tensile stress in the inferior region of femoral neck is higher than that in the superior region (Figure 4-8a and Figure 4-10a) and the compressive stress in the superior region is higher than that in the inferior region (Figure 4-8b and Figure 4-10b). During the single-leg stance; the maximum tensile stress, occurring at the superior femoral neck, is lower than the maximum compressive stress, occurring at the inferior femoral neck; while during the sideways fall, the maximum compressive stress, occurring at the superior femoral neck, is larger than maximum tensile stress, occurring at the inferior femoral neck (Table 4-3). Figure 4-7c and Figure 4-8c show the distribution of von Mises stress in the femur during the single-leg stance and the sideways fall respectively. The distributions of the tensile, compressive, and von Mises stresses at the smallest femoral neck cross-section during the single-leg stance and the sideways fall are shown respectively in Figure 4-9 and Figure 4-10.

For 10 clinical cases (5 females and 5 males, totally 20 right and left femurs), the maximum von Mises stress at the three critical cross-sections of femur during both the single-leg stance and the sideways fall was calculated and the results are shown in Figure 4-11 and Figure 4-12. It was observed that during the sideways fall, the femoral neck and the intertrochanteric region receive higher stresses than the subtrochanteric region (Table 4-5); but during the single-leg stance, there is not very much difference between the stresses in the three regions (Table 4-4); for some cases, the stresses at the subtrochanteric region are the same range as (or even higher than) the stresses at the femoral neck and the intertrochanteric region during the single-leg stance (Figure 4-11).

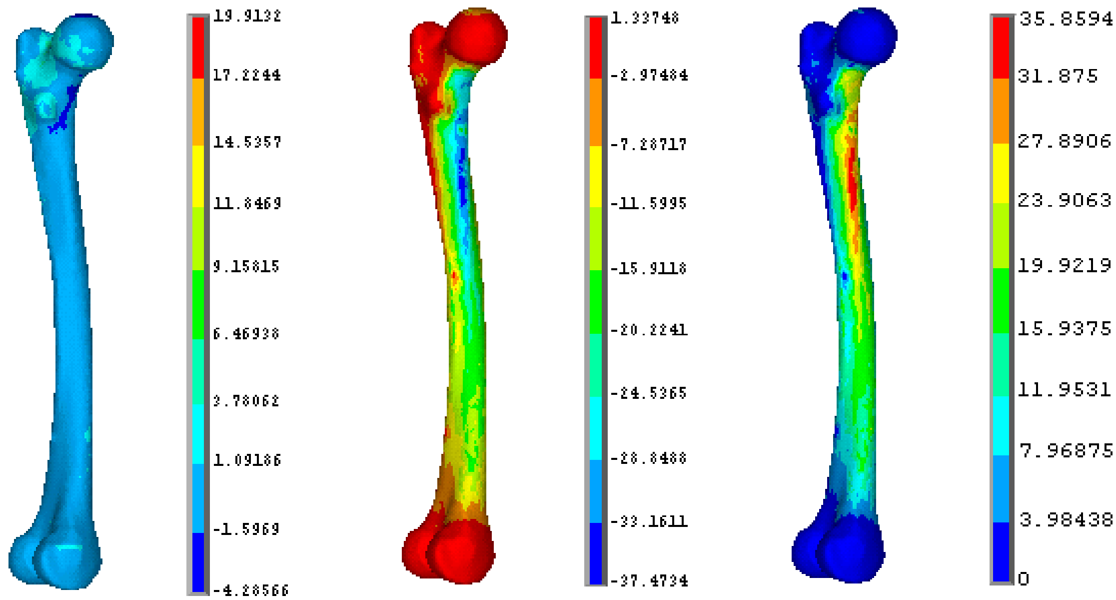

(a) (b) (c)

Figure 4-7. (a) The tensile stress (MPa), (b) the compressive stress (MPa), and (c) the von Mises stress (MPa) distributions in the femur during the single-leg stance.

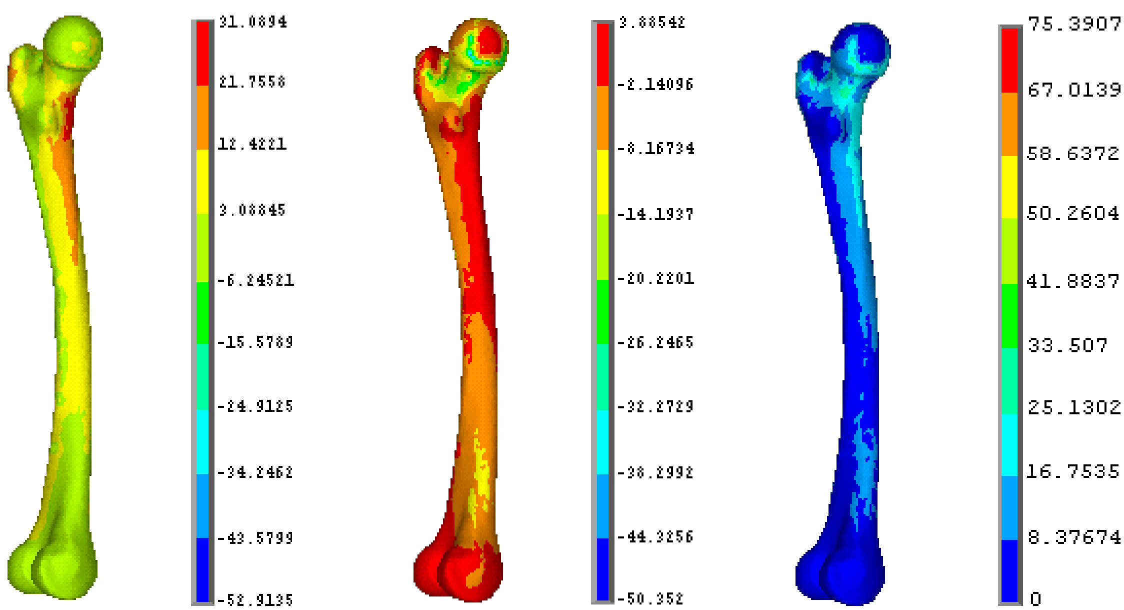

(a) (b) (c)

Figure 4-8. (a) The tensile stress (MPa), (b) the compressive stress (MPa), and (c) the von Mises stress (MPa) distributions in the femur during the sideways fall.

Table 4-3. Comparison of tensile stress and compressive stress distributions in the femoral neck of a clinical case during the single-leg stance and the sideways fall.

	Single-Leg Stance		Sideways Fall	
	Maximum Tensile Stress (MPa)	Maximum Compressive Stress (MPa)	Maximum Tensile Stress (MPa)	Maximum Compressive Stress (MPa)
	6.41	24.58	10.11	29.66
Corresponding occurring region	Superior femoral neck	Inferior femoral neck	Inferior femoral neck	Superior femoral neck

Table 4-4. Average maximum von Mises stress (MPa) at the smallest femoral neck cross-section (SFN CS), the intertrochanteric cross-section (IntT CS), and the subtrochanteric cross-section (SubT CS) of right and left femurs of 10 clinical cases during the single-leg stance.

	Maximum von Mises stress (MPa)					
	Right femurs			Left femurs		
	SFN CS	IntT CS	SubT CS	SFN CS	IntT CS	SubT CS
Range	21.7-49.96	22.23-45.37	26.93-52.47	19.56-52.38	23.55-47.8	27.09-43.04
Average	33.63	32.97	37.89	32.93	32.41	35.84

Table 4-5. Average maximum von Mises stress (MPa) at the smallest femoral neck cross-section (SFN CS), the intertrochanteric cross-section (IntT CS), and the subtrochanteric cross-section (SubT CS) of right and left femurs of 10 clinical cases during the sideways fall.

	Maximum von Mises stress (MPa)					
	Right femurs			Left femurs		
	SFN CS	IntT CS	SubT CS	SFN CS	IntT CS	SubT CS
Range	26.69-148.53	21.57-74.3	9.8-70.63	22.78-69.97	16.2-60.3	6.73-33.2
Average	57.22	40.74	27.08	46.52	33.48	18.66

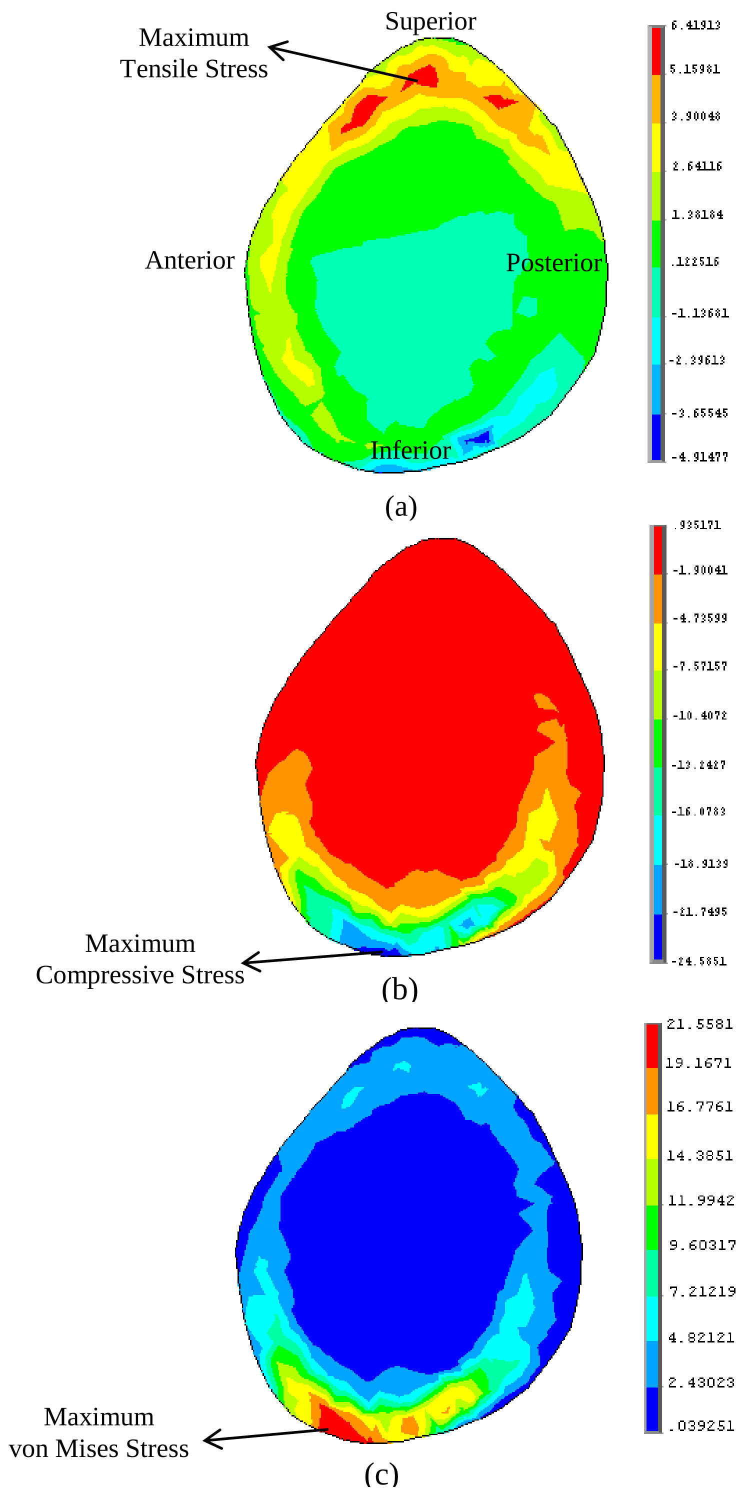

Figure 4-9. (a) The tensile stress (MPa), (b) the compressive stress (MPa), and (c) the von Mises stress (MPa) distributions at the smallest femoral neck cross-section during the single-leg stance.

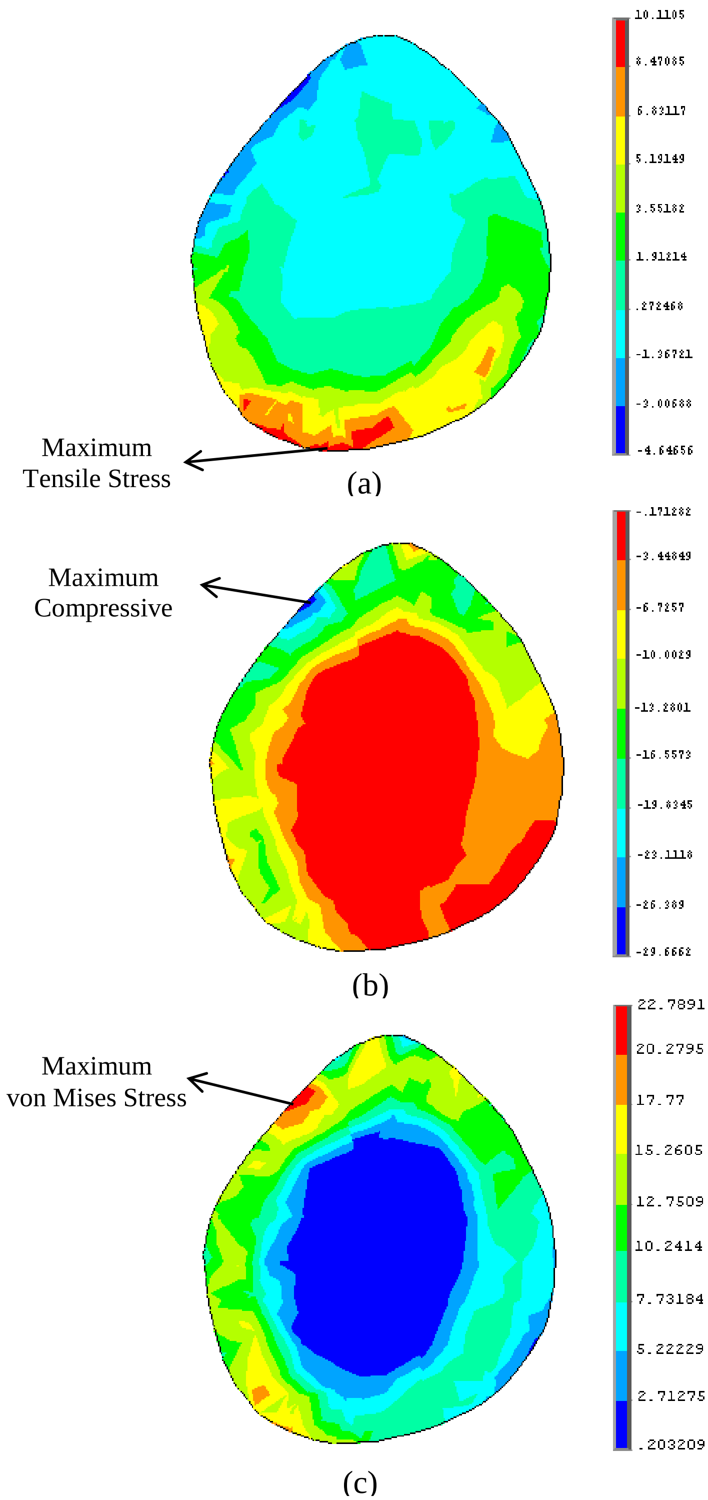

Figure 4-10. (a) The tensile stress (MPa), (b) the compressive stress (MPa), and (c) the von Mises stress (MPa) distributions at the smallest femoral neck cross-section during the sideways fall.

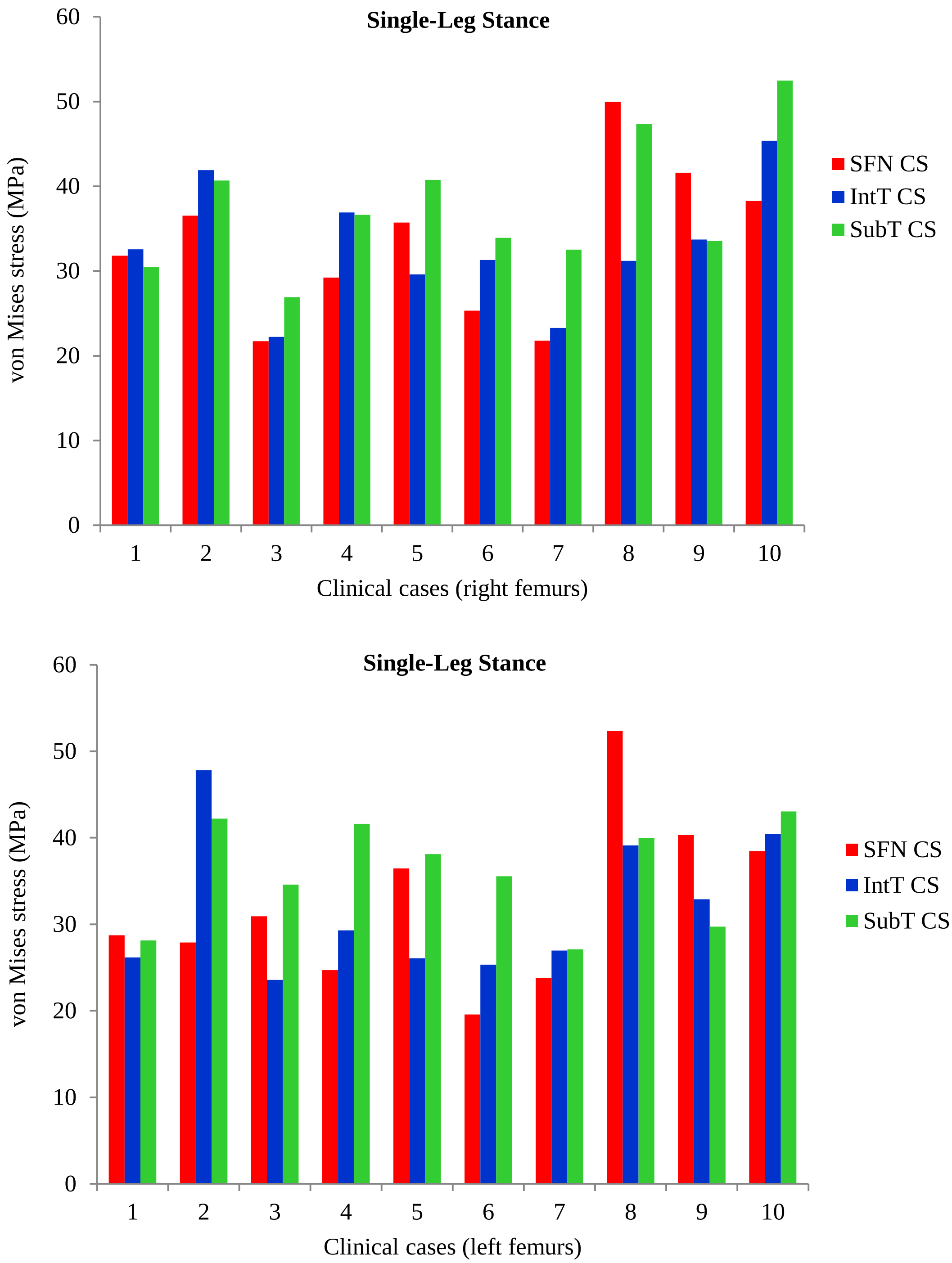

Figure 4-11. The maximum von Mises stress (MPa) at the smallest femoral neck cross-section (SFN CS), the intertrochanteric cross-section (IntT CS), and the subtrochanteric cross-section (SubT CS) of right and left femurs of 10 clinical cases during the single-leg stance.

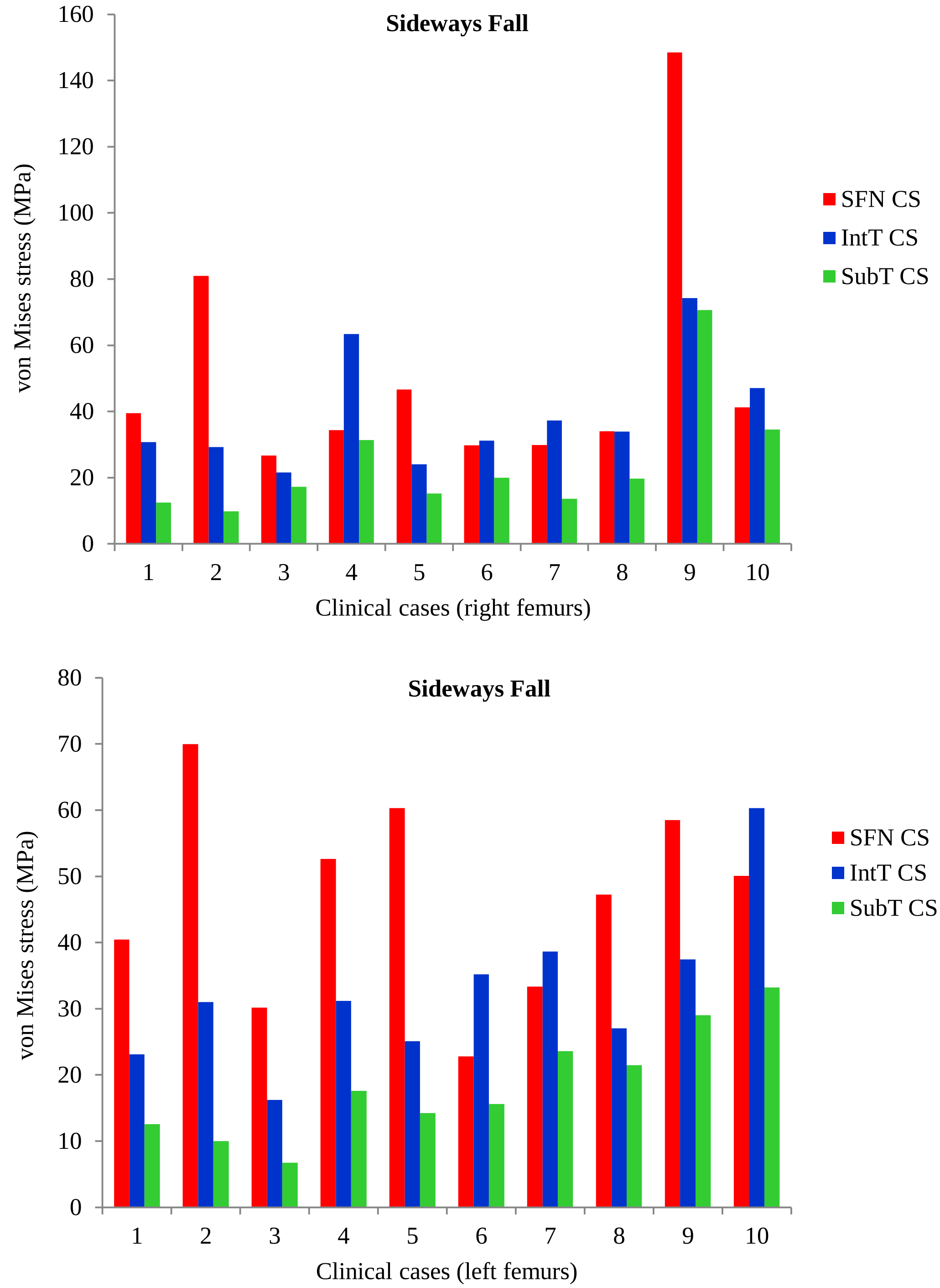

Figure 4-12. The maximum von Mises stress (MPa) at the smallest femoral neck cross-section (SFN CS), the intertrochanteric cross-section (IntT CS), and the subtrochanteric cross-section (SubT CS) of right and left femurs of 10 clinical cases during the sideways fall.

4.4 Strain Patterns at the Three Critical Cross-Sections

The maximum von Mises strain (ε_{vM}) was also obtained at the three critical cross-sections of femur for 10 clinical cases (5 females and 5 males, totally 20 right and left femurs), during both the single-leg stance and the sideways fall (Figure 4-13 and Figure 4-14). It was observed that the strains at the femoral neck and the intertrochanteric region are also much higher than those at the subtrochanteric region during both the single-leg stance and the sideways fall (Table 4-6 and Table 4-7).

Table 4-6. Average maximum von Mises strain at the smallest femoral neck cross-section (SFN CS), the intertrochanteric cross-section (IntT CS), and the subtrochanteric cross-section (SubT CS) of right and left femurs of 10 clinical cases during the single-leg stance.

	Maximum von Mises strain					
	Right femurs			Left femurs		
	SFN CS	IntT CS	SubT CS	SFN CS	IntT CS	SubT CS
Range	3.54E-03 - 1.46E-02	5.89E-03 - 1.74E-02	2.3E-03 - 4.75E-03	5.25E-03 - 1.55E-02	5.49E-03 - 1.87E-02	2.14E-03 - 4.34E-03
Average	9.15E-03	1.08E-02	3.32E-03	9.55E-03	1.05E-02	3.11E-03

Table 4-7. Average maximum von Mises strain at the smallest femoral neck cross-section (SFN CS), the intertrochanteric cross-section (IntT CS), and the subtrochanteric cross-section (SubT CS) of right and left femurs of 10 clinical cases during the sideways fall.

	Maximum von Mises strain					
	Right femurs			Left femurs		
	SFN CS	IntT CS	SubT CS	SFN CS	IntT CS	SubT CS
Range	1.67E-02 - 1.04E-01	4.34E-02 - 1.50E-01	1.12E-03 - 6.38E-03	1.67E-02 - 7.43E-02	3.35E-02 - 1.91E-01	5.08E-04 - 3.31E-03
Average	5.29E-02	9.80E-02	2.44E-03	4.26E-02	9.37E-02	1.74E-03

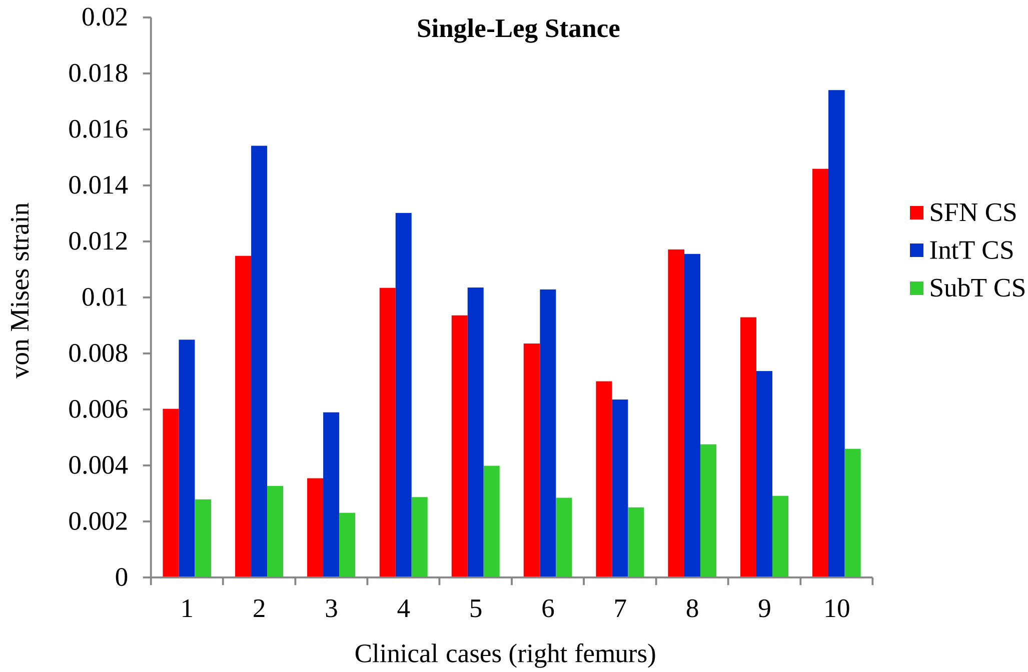

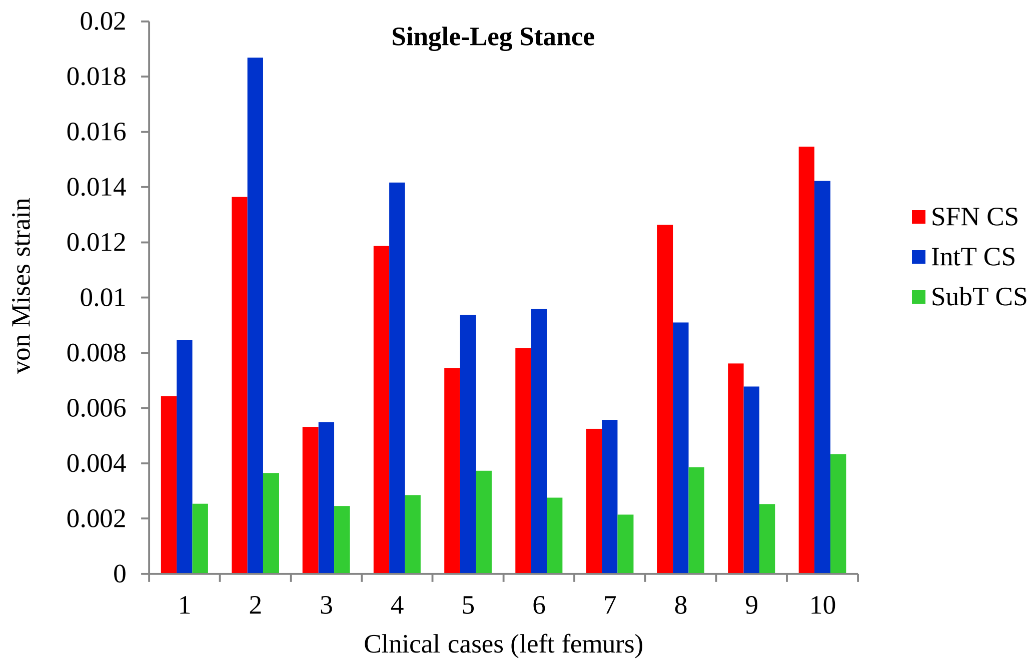

Figure 4-13. The maximum von Mises strain at the smallest femoral neck cross-section (SFN CS), the intertrochanteric cross-section (IntT CS), and the subtrochanteric cross-section (SubT CS) of right and left femurs of 10 clinical cases during the single-leg stance.

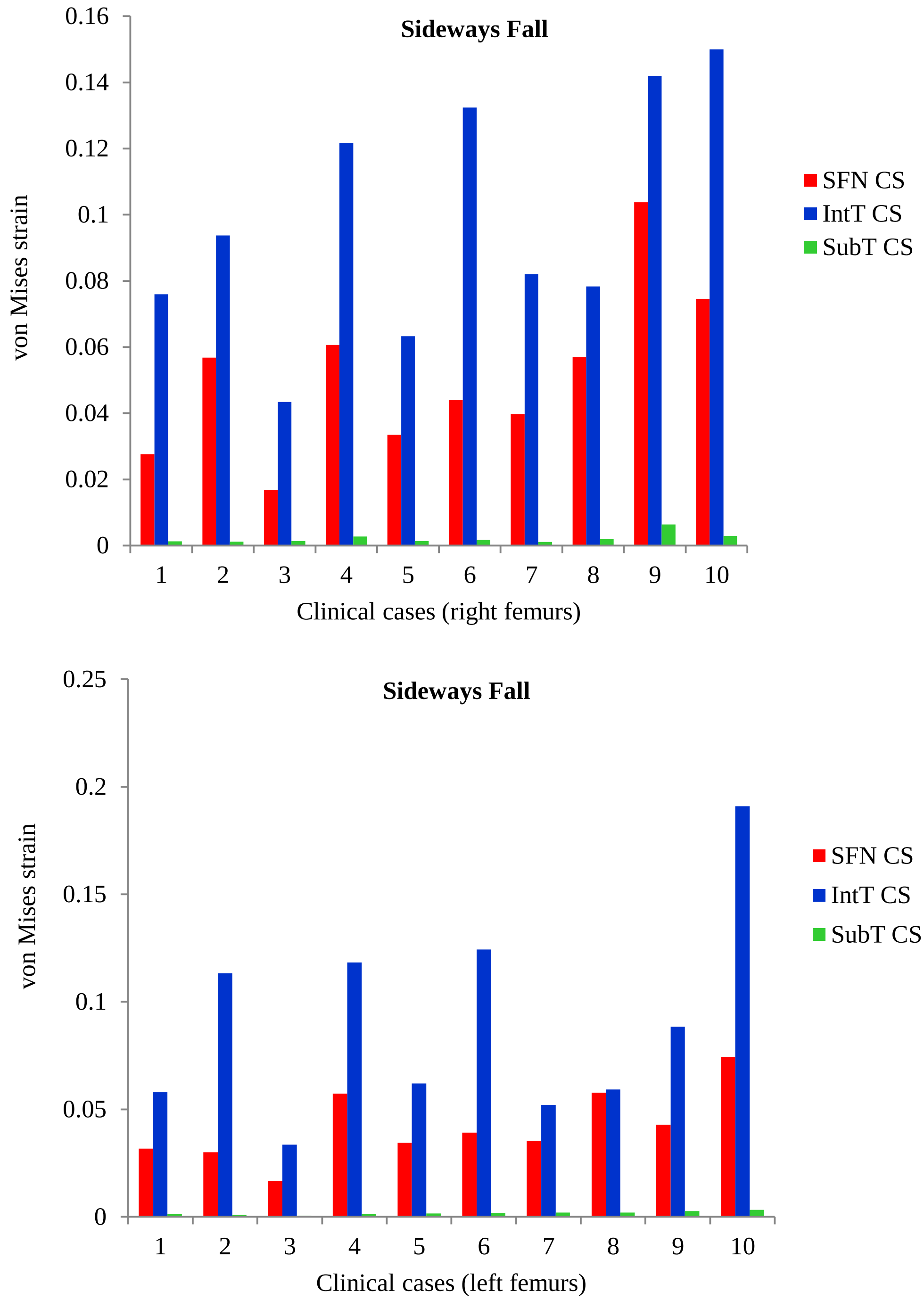

Figure 4-14. The maximum von Mises strain at the smallest femoral neck cross-section (SFN CS), the intertrochanteric cross-section (IntT CS), and the subtrochanteric cross-section (SubT CS) of right and left femurs of 10 clinical cases during the sideways fall.

4.5 Hip Fracture Risk Indices

4.5.1 Comparison of Hip Fracture Risk at the Three Critical Cross-Sections

For the 60 clinical cases (30 females and 30 males, totally 120 right and left femurs), hip fracture risk indices were calculated for the smallest femoral neck cross-section, the intertrochanteric cross-section, and the subtrochanteric cross-section of femur during the single-leg stance and the sideways fall using the strain energy criterion. The results of this study showed that during the single-leg stance, the smallest femoral neck cross-section had the highest FRI for both the right and left femurs of all clinical cases (Figure 4-15 and Figure 4-16). As shown in Table 4-8, Table 4-9, and Figure 4-17, the average FRI at the smallest femoral neck cross-section of the 60 right femurs and 60 left femurs was higher than those at the intertrochanteric cross-section and the subtrochanteric cross-section during the single-leg stance.

During the sideways fall, in 78.3% of the right femurs and in 76.7% of the left femurs, the maximum FRI was obtained at the smallest femoral neck cross-section; and in 21.7% of the right femurs and in 23.3% of the left femurs, the maximum FRI was observed in the intertrochanteric cross-section. For all clinical cases, in both right and left femurs, the FRIs at the subtrochanteric cross-section were much lower than those at the smallest femoral neck cross-section and the intertrochanteric cross-section during the sideways fall. Figure 4-18 and Figure 4-19 respectively show the FRIs at the three critical cross-sections of right and left femurs during the sideways fall. During the sideways fall, the average FRI at the smallest femoral neck cross-section in all cases was higher than those at the intertrochanteric cross-section and the subtrochanteric cross-section (Table 4-10, Table 4-11, and Figure 4-20).

For the single-leg stance, FRIs for all cases at the three critical cross-sections are much lower than one (FRI<<1), indicating that the possibility of hip fracture incidence in the single-leg stance was low. For the sideways fall, FRIs of 8 right femurs and 7 left femurs at the smallest femoral neck cross-section and FRIs of 7 right femurs and 5 left femurs at the intertrochanteric cross-section were higher than one (FRI>1), meaning there is possibility for fracture occurring in these regions; but the FRIs at the subtrochanteric cross-section in all cases were much lower than one (FRI<<1), indicating there is lower possibility of fracture in this region. Figure 4-21 shows the number of possible fracture at the three critical cross-sections of femur during the sideways fall, i.e., the cases that have FRI larger than one (FRI>1) at one of the three critical cross-sections.

Table 4-8. Average FRI at the three critical cross-sections of 60 right femurs during the single-leg stance.

	FRI		
	Smallest femoral neck cross-section	Intertrochanteric cross-section	Subtrochanteric cross-section
Range	0.0261-0.2124	0.0099-0.143	0.0058-0.0363
Average	0.0752	0.0351	0.0155

Table 4-9. Average FRI at the three critical cross-sections of 60 left femurs during the single-leg stance.

	FRI		
	Smallest femoral neck cross-section	Intertrochanteric cross-section	Subtrochanteric cross-section
Range	0.023-0.1936	0.0095-0.1078	0.0037-0.0337
Average	0.0681	0.0329	0.0142

Table 4-10. Average FRI at the three critical cross-sections of 60 right femurs during the sideways fall.

	FRI		
	Smallest femoral neck cross-section	Intertrochanteric cross-section	Subtrochanteric cross-section
Range	0.1725-3.0448	0.1226-1.534	0.0004-0.0812
Average	0.6944	0.5245	0.0091

Table 4-11. Average FRI at the three critical cross-sections of 60 left femurs during the sideways fall.

	FRI		
	Smallest femoral neck cross-section	Intertrochanteric cross-section	Subtrochanteric cross-section
Range	0.1599-1.8301	0.116-1.5493	0.0004-0.0585
Average	0.6395	0.4864	0.0083

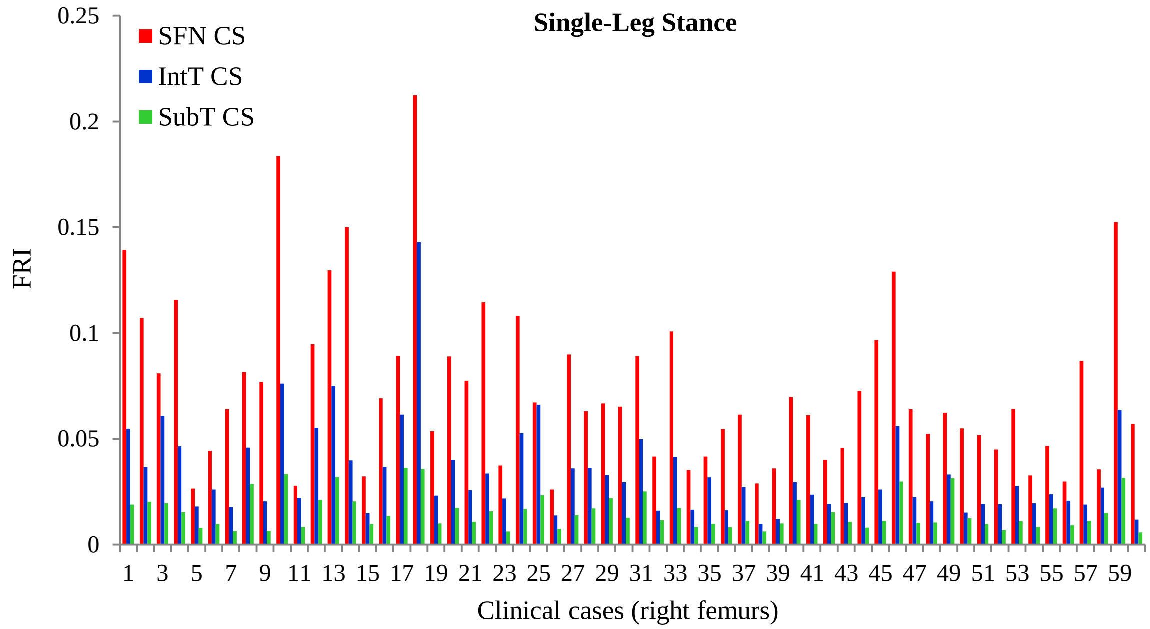

Figure 4-15. FRIs at the smallest femoral neck cross-section (SFN CS), the intertrochanteric cross-section (IntT CS), and the subtrochanteric cross-section (SubT CS) of 60 right femurs during the single-leg stance.

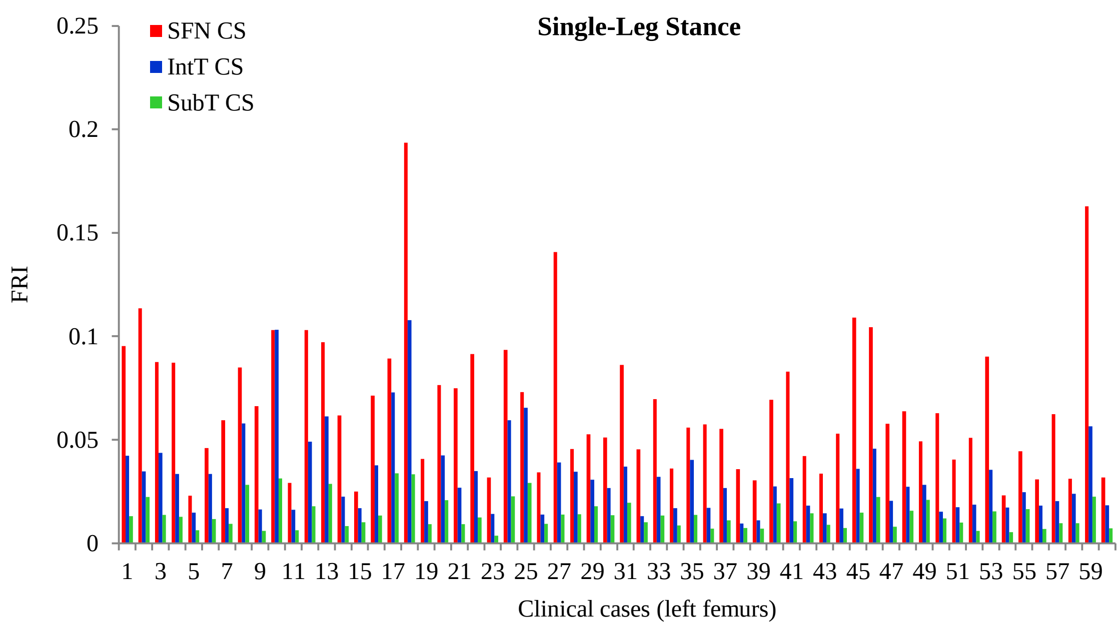

Figure 4-16. FRIs at the smallest femoral neck cross-section (SFN CS), the intertrochanteric cross-section (IntT CS), and the subtrochanteric cross-section (SubT CS) of 60 left femurs during the single-leg stance.

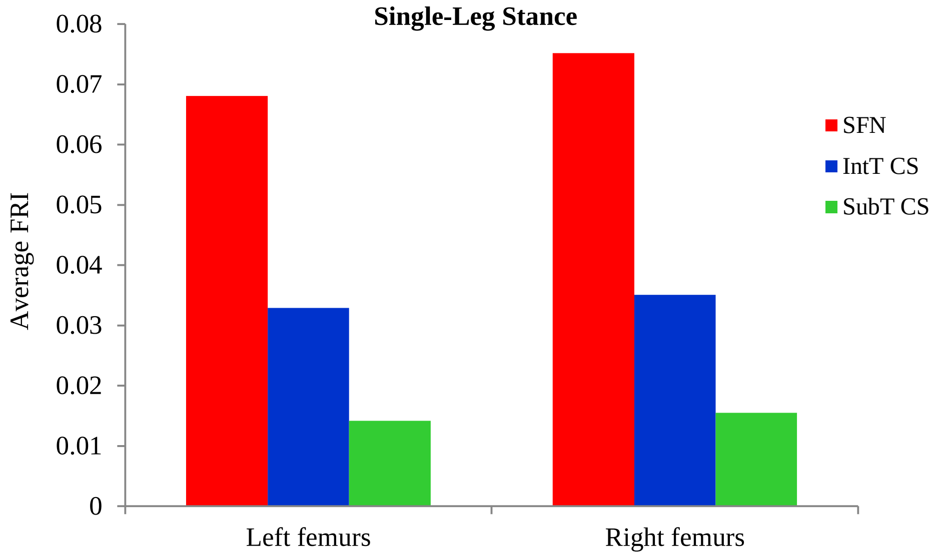

Figure 4-17. Average FRI at the smallest femoral neck cross-section (SFN CS), the intertrochanteric cross-section (IntT CS), and the subtrochanteric cross-section (SubT CS) of 60 right femurs and 60 left femurs during the single-leg stance.

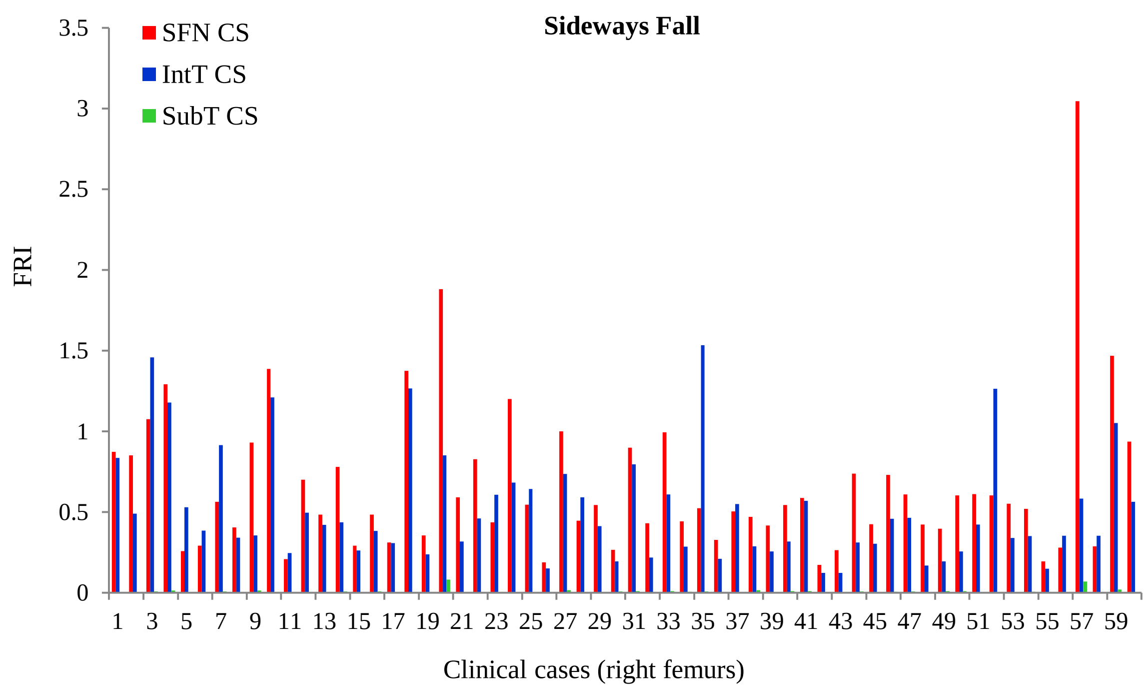

Figure 4-18. FRIs at the smallest femoral neck cross-section (SFN CS), the intertrochanteric cross-section (IntT CS), and the subtrochanteric cross-section (SubT CS) of 60 right femurs during the sideways fall.

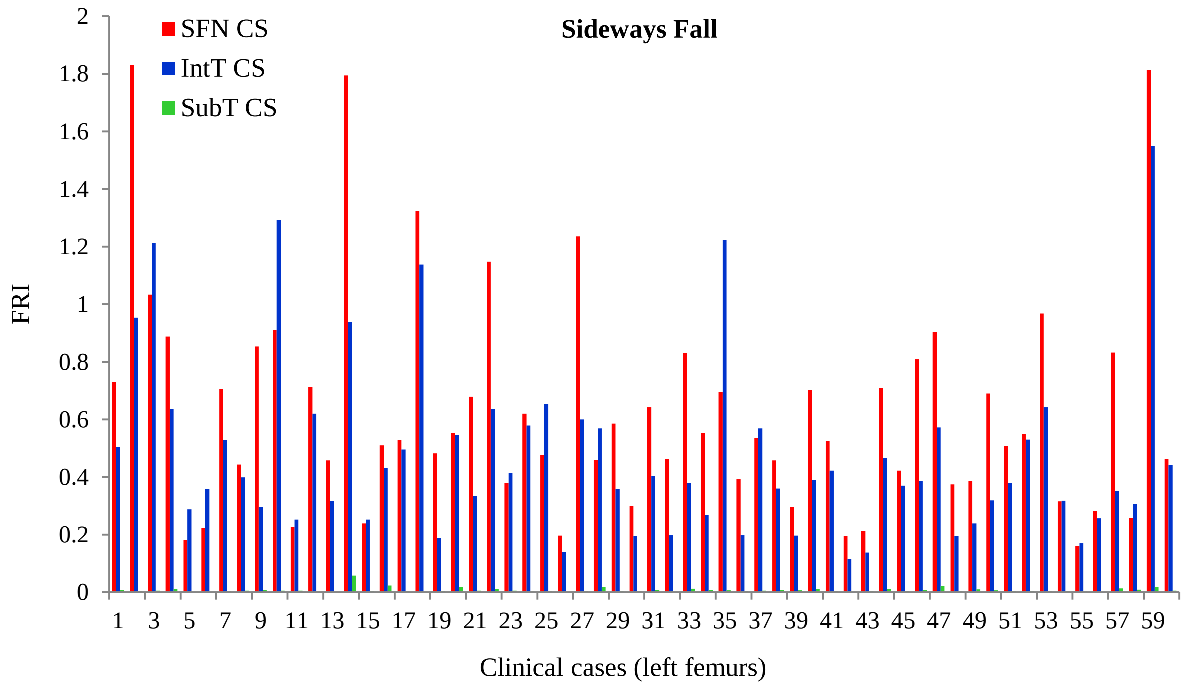

Figure 4-19. FRIs at the smallest femoral neck cross-section (SFN CS), the intertrochanteric cross-section (IntT CS), and the subtrochanteric cross-section (SubT CS) of 60 left femurs during the sideways fall.

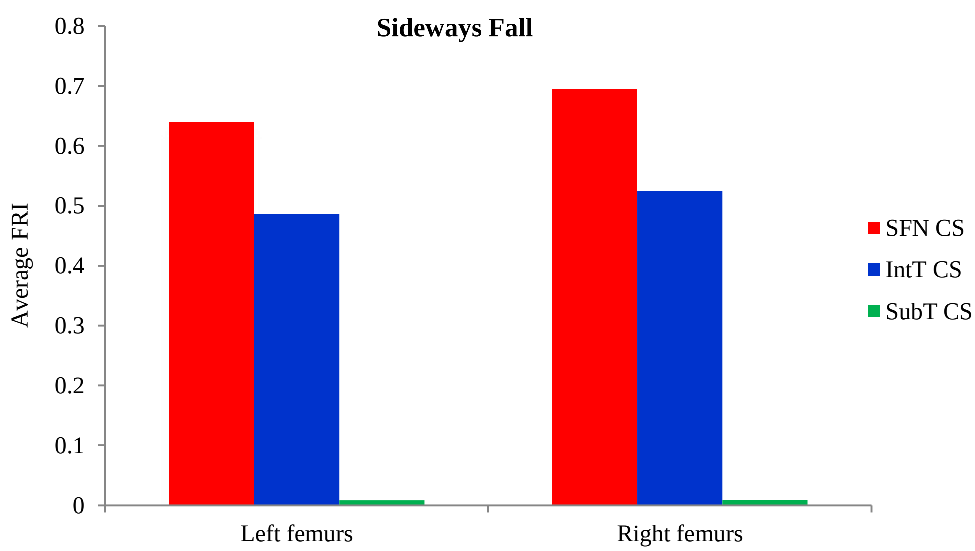

Figure 4-20. Average FRI at the smallest femoral neck cross-section (SFN CS), the intertrochanteric cross-section (IntT CS), and the subtrochanteric cross-section (SubT CS) of 60 right femurs and 60 left femurs during the sideways fall.

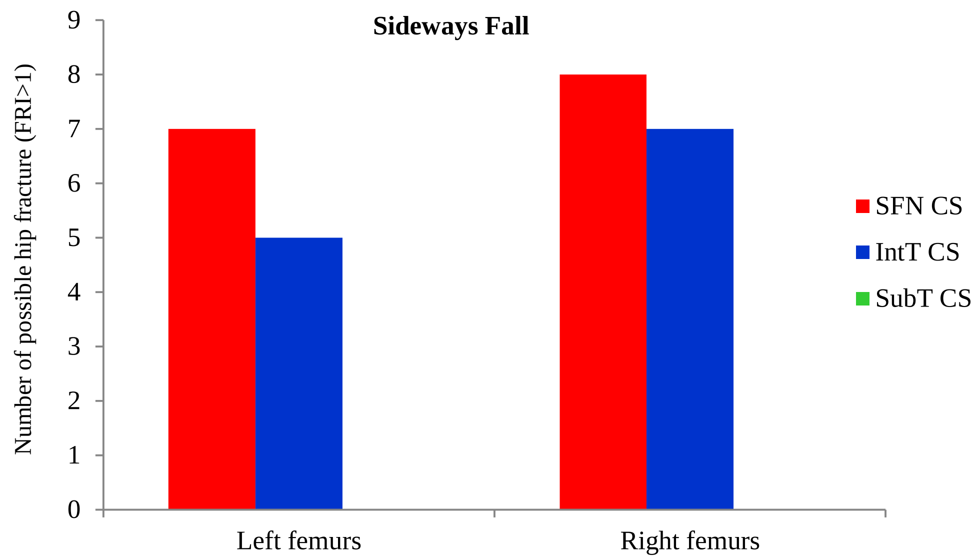

Figure 4-21. Number of possible hip fracture occurring at the smallest femoral neck cross-section (SFN CS), the intertrochanteric cross-section (IntT CS), and the subtrochanteric cross-section (SubT CS) of 60 right femurs and 60 left femurs during the sideways fall, i.e., cases that have the FRI higher than one (FRI >1) at one of the three critical cross-sections.

4.5.2 Comparison of Hip Fracture Risk in Women and Men

In this study, hip fracture risk for the 30 females (totally 60 right and left femurs) and 30 males (totally 60 right and left femurs) was assessed. Fracture risk indices at the smallest femoral neck cross-section, the intertrochanteric cross-section, and the subtrochanteric cross-section for the single-leg stance and the sideways fall are shown in Figure 4-22 to Figure 4-27. The average hip fracture risk of females was generally higher than that of males. As it can be seen from Table 4-12 to Table 4-14, Figure 4-28, and Figure 4-29, the average FRI at the smallest femoral neck cross-section, the intertrochanteric cross-section, and the subtrochanteric cross-section of the 30 females (totally 60 right and left femurs) are higher than that of the 30 males (totally 60 right and left femurs) for both the single-leg stance and the sideways fall.

For the single-leg stance, FRIs in all cases and at all the critical cross-sections are much smaller than one (FRI<<1), indicating there is lower possibility of hip fracture for both women and men during the single-leg stance. For the sideways fall, FRIs of 12 females and 3 males at the smallest femoral neck cross-section, and FRIs of 7 females and 5 males at the intertrochanteric cross-section were higher than one (FRI>1), meaning that hip fracture may occur in these regions; but FRIs at the subtrochanteric cross-section in all cases were much below one (FRI<<1), suggesting that the femoral shaft is the strongest part of the femur. Figure 4-30 shows the number of possible hip fracture in women and men during the sideways fall for the studied cases.

Table 4-12. Average FRI at the smallest femoral neck cross-section of 30 females (totally 60 right and left femurs) and 30 males (totally 60 right and left femurs) during the single-leg stance and the sideways fall.

FRI at the smallest femoral neck cross-section				
	Single-leg stance		Sideways fall	
	Female	Male	Female	Male
Range	0.023-0.2124	0.0231-0.1628	0.1826-1.8809	0.1599-3.0448
Average	0.0816	0.0611	0.7035	0.6315

Table 4-13. Average FRI at the intertrochanteric cross-section of 30 females (totally 60 right and left femurs) and 30 males (totally 60 right and left femurs) during the single-leg stance and the sideways fall.

FRI at the intertrochanteric cross-section				
	Single-leg stance		Sideways fall	
	Female	Male	Female	Male
Range	0.0138-0.143	0.0095-0.0637	0.1398-1.4572	0.116-1.5493
Average	0.042	0.0253	0.5666	0.4433

Table 4-14. Average FRI at the subtrochanteric cross-section of 30 females (totally 60 right and left femurs) and 30 males (totally 60 right and left femurs) during the single-leg stance and the sideways fall.

FRI at the subtrochanteric cross-section				
	Single-leg stance		Sideways fall	
	Female	Male	Female	Male
Range	0.0037-0.0363	0.0053-0.0315	0.0004-0.0812	0.0004-0.0694
Average	0.0167	0.0129	0.0087	0.0088

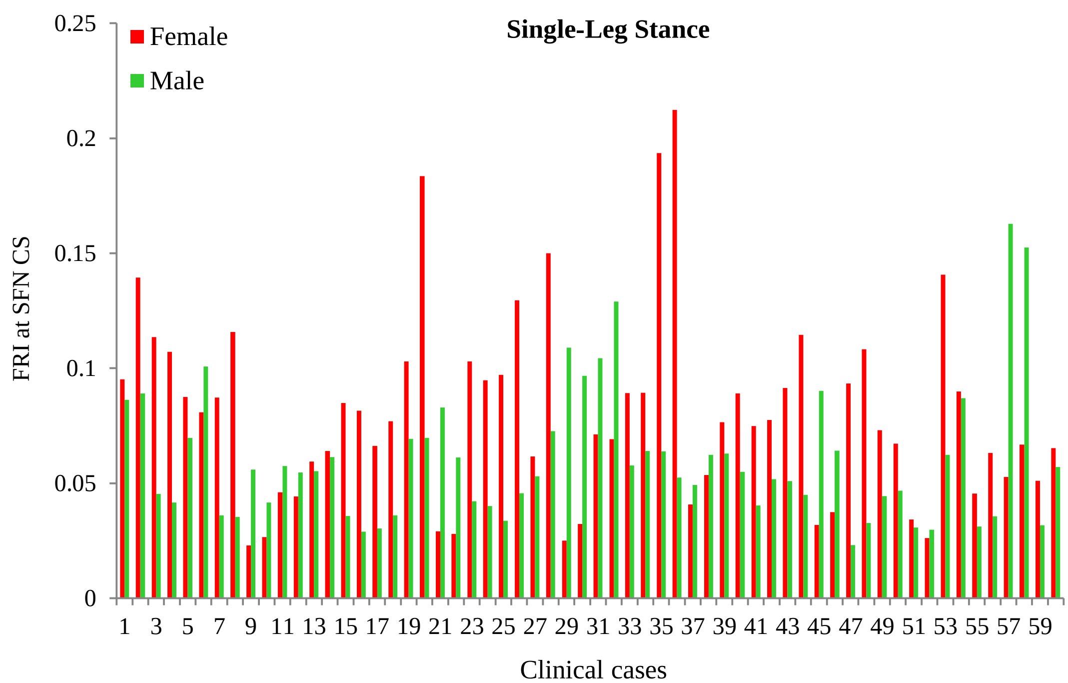

Figure 4-22. FRIs at the smallest femoral neck cross-section (SFN CS) of 30 females (totally 60 right and left femurs) and 30 males (totally 60 right and left femurs) during the single-leg stance.

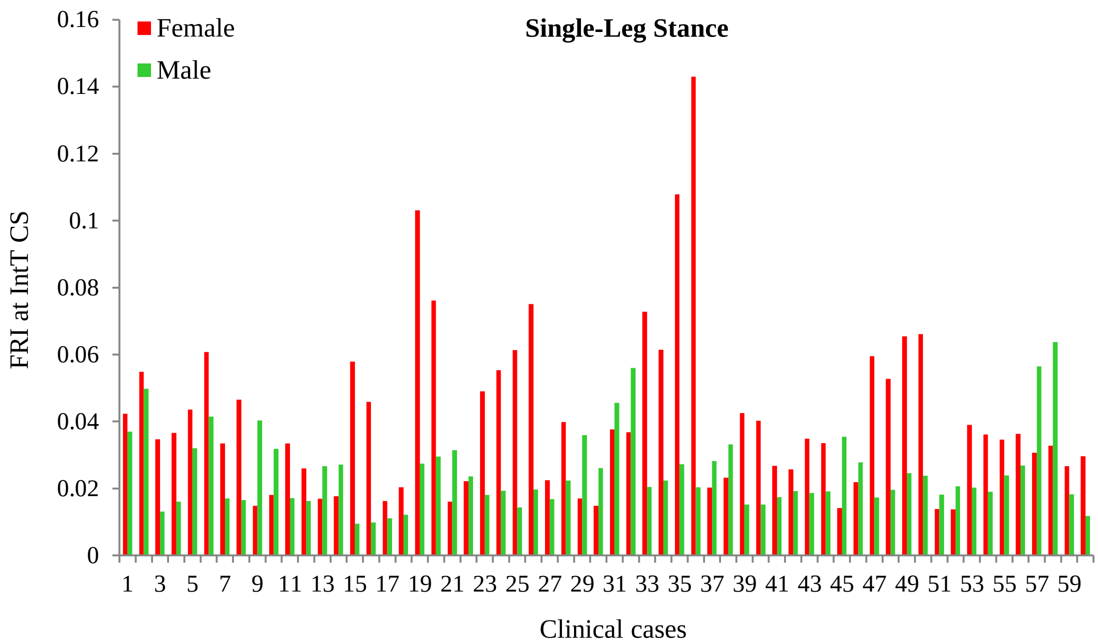

Figure 4-23. FRIs at the intertrochanteric cross-section (IntT CS) of 30 females (totally 60 right and left femurs) and 30 males (totally 60 right and left femurs) during the single-leg stance.

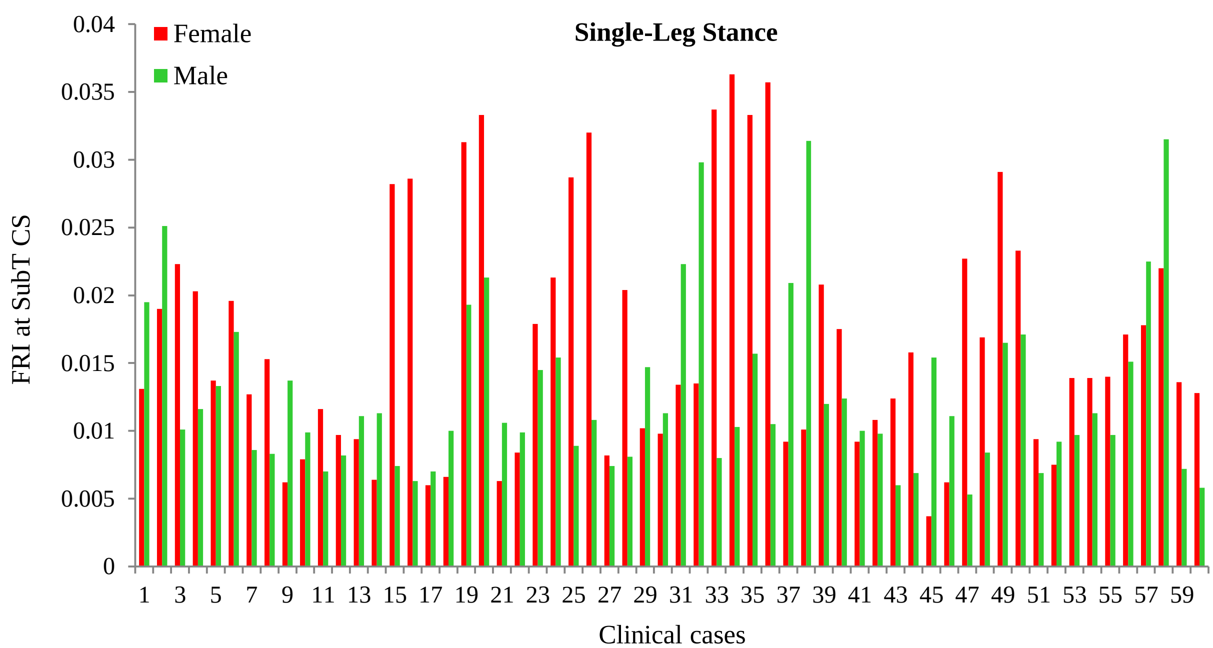

Figure 4-24. FRIs at the subtrochanteric cross-section (SubT CS) of 30 females (totally 60 right and left femurs) and 30 males (totally 60 right and left femurs) during the single-leg stance.

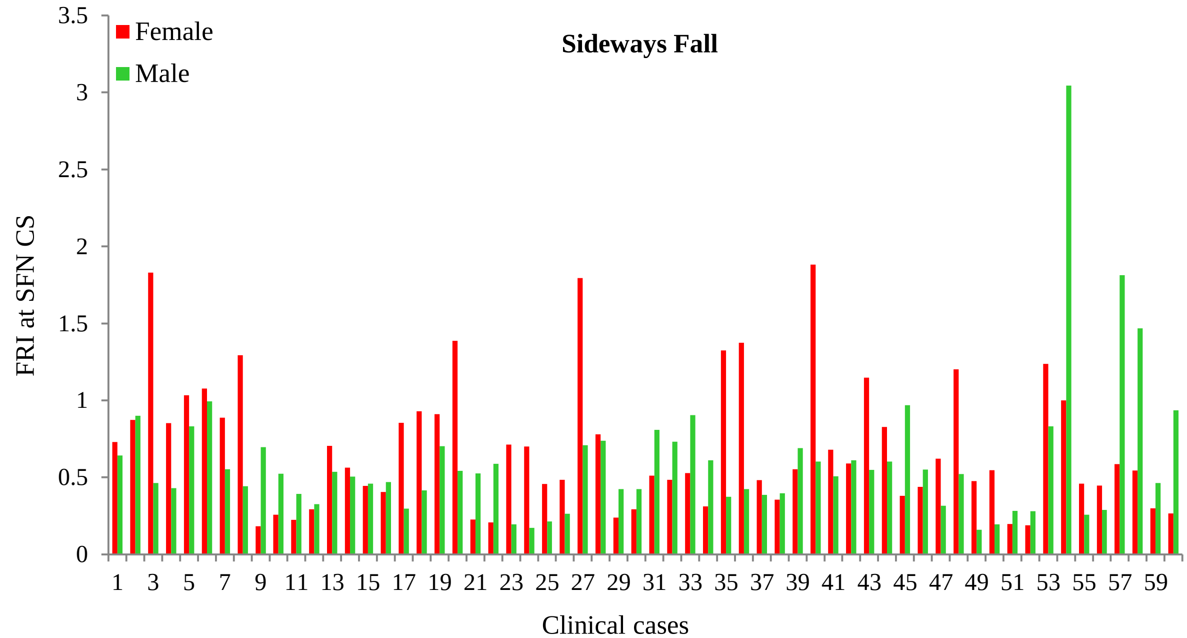

Figure 4-25. FRIs at the smallest femoral neck cross-section (SFN CS) of 30 females (totally 60 right and left femurs) and 30 males (totally 60 right and left femurs) during the sideways fall.

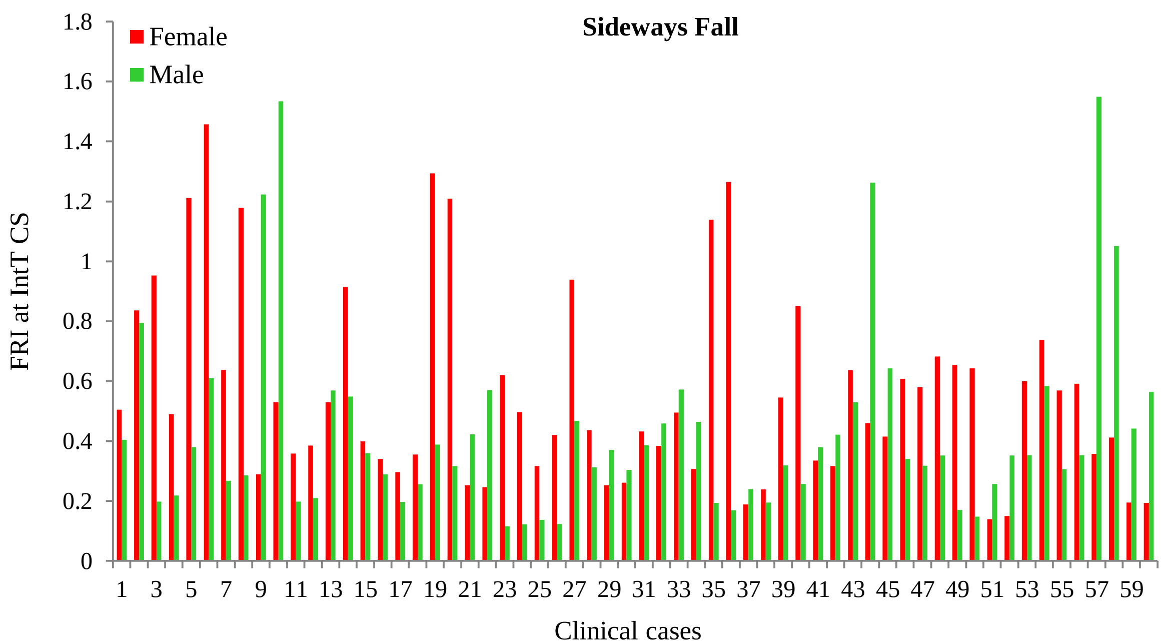

Figure 4-26. FRIs at the intertrochanteric cross-section (IntT CS) of 30 females (totally 60 right and left femurs) and 30 males (totally 60 right and left femurs) during the sideways fall.

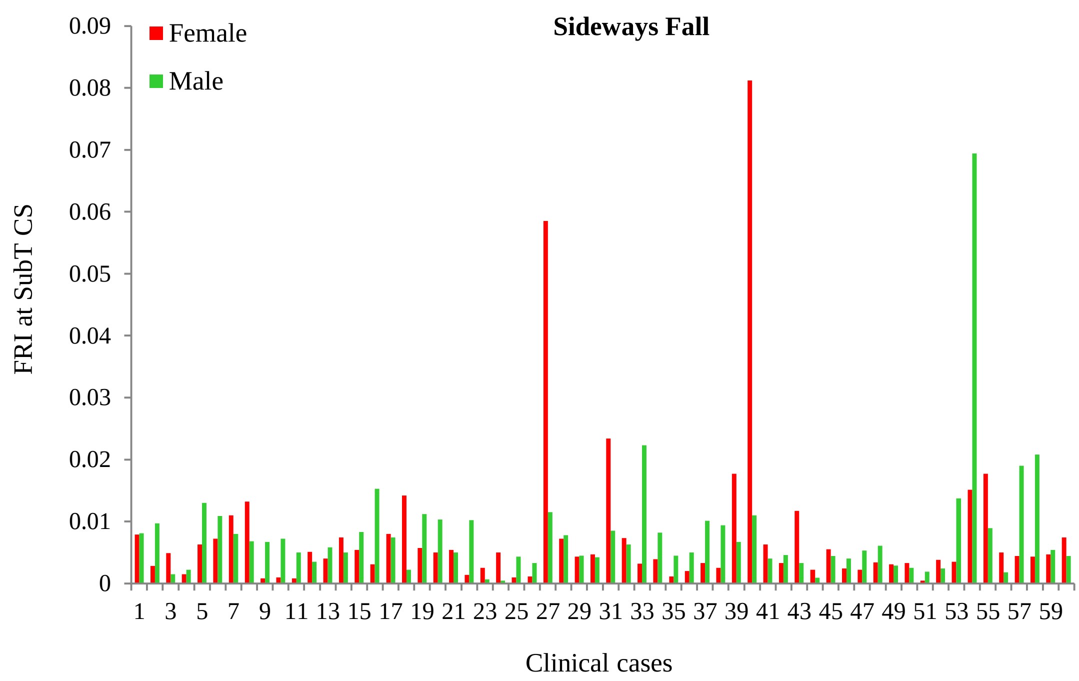

Figure 4-27. FRIs at the subtrochanteric cross-section (SubT CS) of 30 females (totally 60 right and left femurs) and 30 males (totally 60 right and left femurs) during the sideways fall.

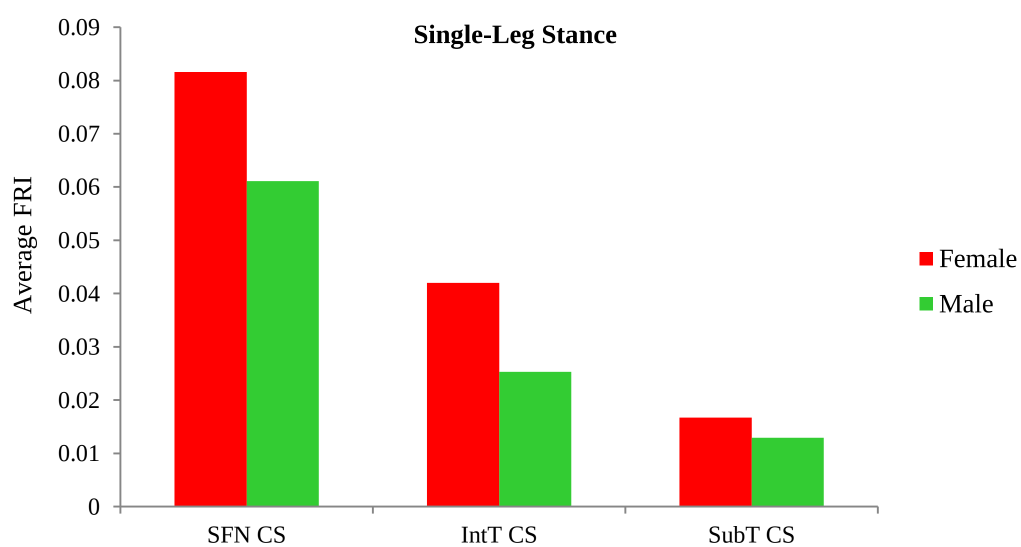

Figure 4-28. Average FRI at the smallest femoral neck cross-section (SFN CS), the intertrochanteric cross-section (IntT CS), and the subtrochanteric cross-section (SubT CS) of 30 females (totally 60 right and left femurs) and 30 males (totally 60 right and left femurs) during the single-leg stance.

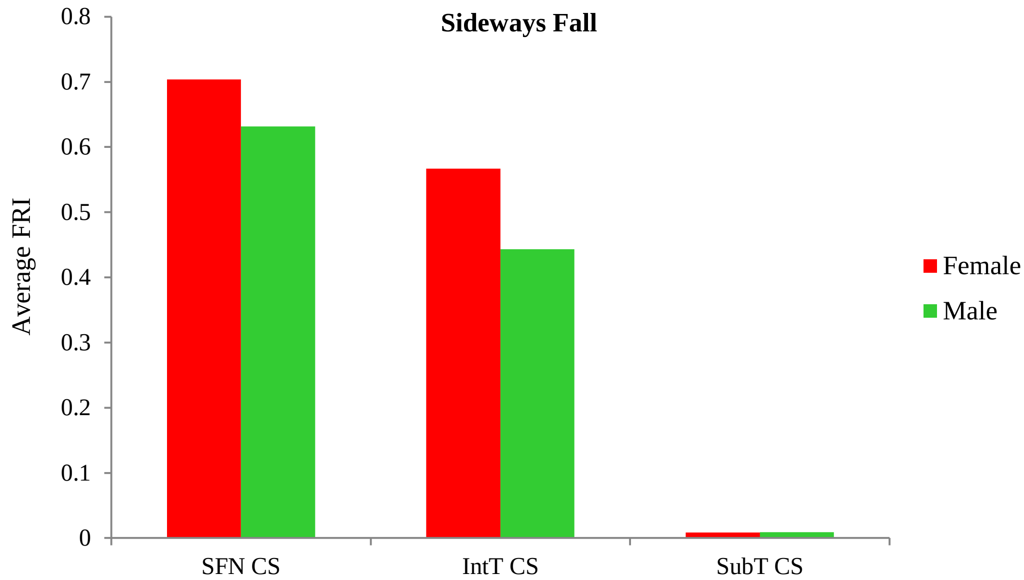

Figure 4-29. Average FRI at the smallest femoral neck cross-section (SFN CS), the intertrochanteric cross-section (IntT CS), and the subtrochanteric cross-section (SubT CS) of 30 females (totally 60 right and left femurs) and 30 males (totally 60 right and left femurs) during the sideways fall.

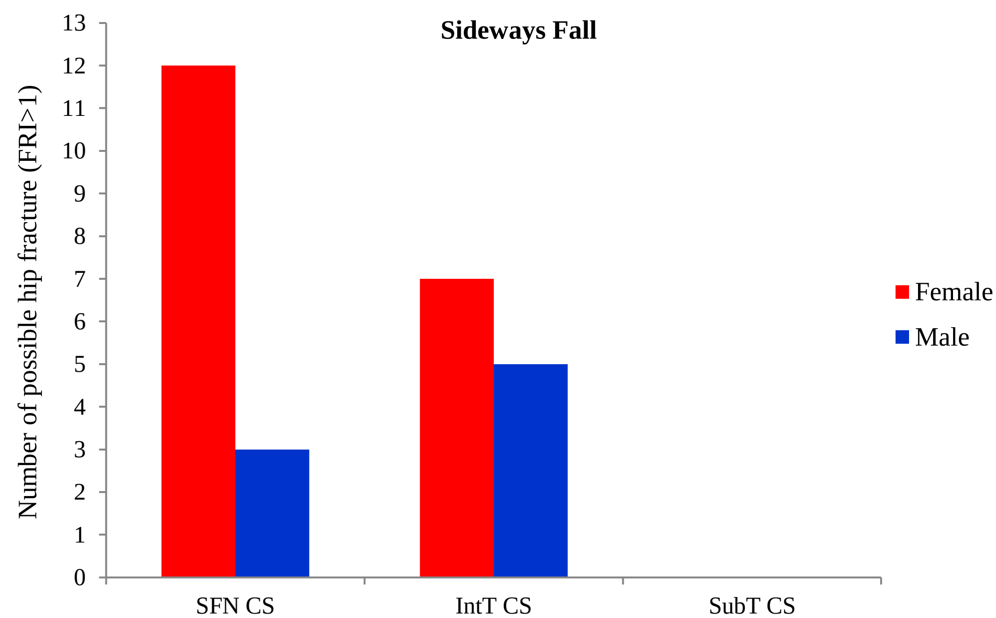

Figure 4-30. Number of possible hip fracture occurring at the smallest femoral neck cross-section (SFN CS), the intertrochanteric cross-section (IntT CS), and the subtrochanteric cross-section (SubT CS) of 30 females (totally 60 right and left femurs) and 30 males (totally 60 right and left femurs) during the sideways fall.

4.5.3 Parametric Study of Hip Fracture Risk

In this study, the correlation between the hip fracture risk and different parameters such as age, body height, weight, and BMI were investigated using 30 females (totally 60 right and left femurs) and 30 males (totally 60 right and left femurs). The correlation coefficients (r) and the corresponding statistical significance (p-value) were calculated using in-house MATLAB codes. The obtained results are given in Table 4-15 to Table 4-18.

The FRI versus age at the three critical cross-sections of femur during the single-leg stance and the sideways fall for 30 females and 30 males are shown in the scattered plots in Figure 4-31 and Figure 4-32 respectively. It is seen that the hip fracture risk has a positive correlation with age at the three critical cross-sections, but as shown in Table 4-15 to Table 4-18, this correlation is not strong ($p > 0.05$).

The scattered plots of FRI versus height at the three critical cross-sections of femur during the single-leg stance and the sideways fall for 30 females and 30 males are also shown respectively in Figure 4-33 and Figure 4-34. The hip fracture risk also has a positive correlation with height, but this correlation for females during both the single-leg stance and the sideways fall and for males during the single-leg stance is weak ($p > 0.05$) (Table 4-15 to Table 4-17), while there is a strong correlation ($p < 0.05$) between the hip fracture risk and height for males during the sideways fall (Table 4-18).

As seen in Figure 4-35 and Figure 4-36, there is an increasing trend of FRI versus body weight. There is a strong correlation ($p < 0.05$) between the hip fracture risk and body weight at the three critical cross-sections of femur for both females and males during the single-leg stance and also at the smallest femoral neck cross-section and the subtrochanteric cross-section of males during the sideways fall (Table 4-15, Table 4-17, and Table 4-18). While this correlation is not strong ($p > 0.05$) at the three critical cross-sections of femur for females and the intertrochanteric cross-section of males during the sideways fall (Table 4-16 and Table 4-18).

The correlation between FRI and BMI (representative of body shape) is also positive (Figure 4-37 and Figure 4-38). This correlation is strong ($p < 0.05$) at the three critical cross-sections of femur for both females and males during the single-leg stance, the smallest femoral neck cross-section of females and males during the sideways fall, and the subtrochanteric cross-section of males during the sideways fall (Table 4-15 to Table 4-18). While there is a weak correlation ($p > 0.05$) between FRI and BMI at the intertrochanteric cross-section of both females and males during the sideways fall and the subtrochanteric cross-section of females during the sideways fall (Table 4-16 and Table 4-18).

Table 4-15. Correlation (coefficient r, p-value) between FRIs and the parameters in 30 females during the single-leg stance.

	r (p)			
	Age	Height	Body weight	BMI
Smallest femoral neck cross-section	-0.0535 (0.6844)	0.0153 (0.9072)	0.2933 (0.0229)	0.3338 (0.0091)
Intertrochanteric cross-section	0.0422 (0.7484)	-0.0805 (0.5405)	0.2757 (0.0329)	0.3338 (0.0091)
Subtrochanteric cross-section	0.0398 (0.7625)	-0.0201 (0.8783)	0.546 (0.000006)	0.6108 (0.0000002)

Table 4-16. Correlation (coefficient r, p-value) between FRIs and the parameters in 30 females during the sideways fall.

	r (p)			
	Age	Height	Body weight	BMI
Smallest femoral neck cross-section	-0.0473 (0.7194)	0.0082 (0.9498)	0.2133 (0.1017)	0.2554 (0.0488)
Intertrochanteric cross-section	0.0379 (0.7734)	-0.0576 (0.6616)	0.0964 (0.4636)	0.1383 (0.2919)
Subtrochanteric cross-section	-0.0989 (0.452)	0.1332 (0.31)	0.1344 (0.3056)	0.103 (0.4332)

Table 4-17. Correlation (coefficient r, p-value) between FRIs and the parameters in 30 males during the single-leg stance.

	r (p)			
	Age	Height	Body weight	BMI
Smallest femoral neck cross-section	0.1464 (0.264)	0.0946 (0.472)	0.5372 (0.000009)	0.5038 (0.00004)
Intertrochanteric cross-section	-0.0358 (0.7859)	0.2242 (0.085)	0.4496 (0.0003)	0.3788 (0.0028)
Subtrochanteric cross-section	-0.1778 (0.174)	-0.0119 (0.928)	0.5681 (0.000002)	0.6028 (0.0000003)

Table 4-18. Correlation (coefficient r, p-value) between FRIs and the parameters in 30 males during the sideways fall.

	r (p)			
	Age	Height	Body weight	BMI
Smallest femoral neck cross-section	0.0697 (0.5964)	0.2566 (0.047)	0.4582 (0.0002)	0.3504 (0.006)
Intertrochanteric cross-section	-0.0475 (0.7179)	0.4446 (0.0003)	0.1485 (0.2573)	-0.0192 (0.8839)
Subtrochanteric cross-section	0.0059 (0.9637)	0.2678 (0.038)	0.5059 (0.00003)	0.4041 (0.0013)

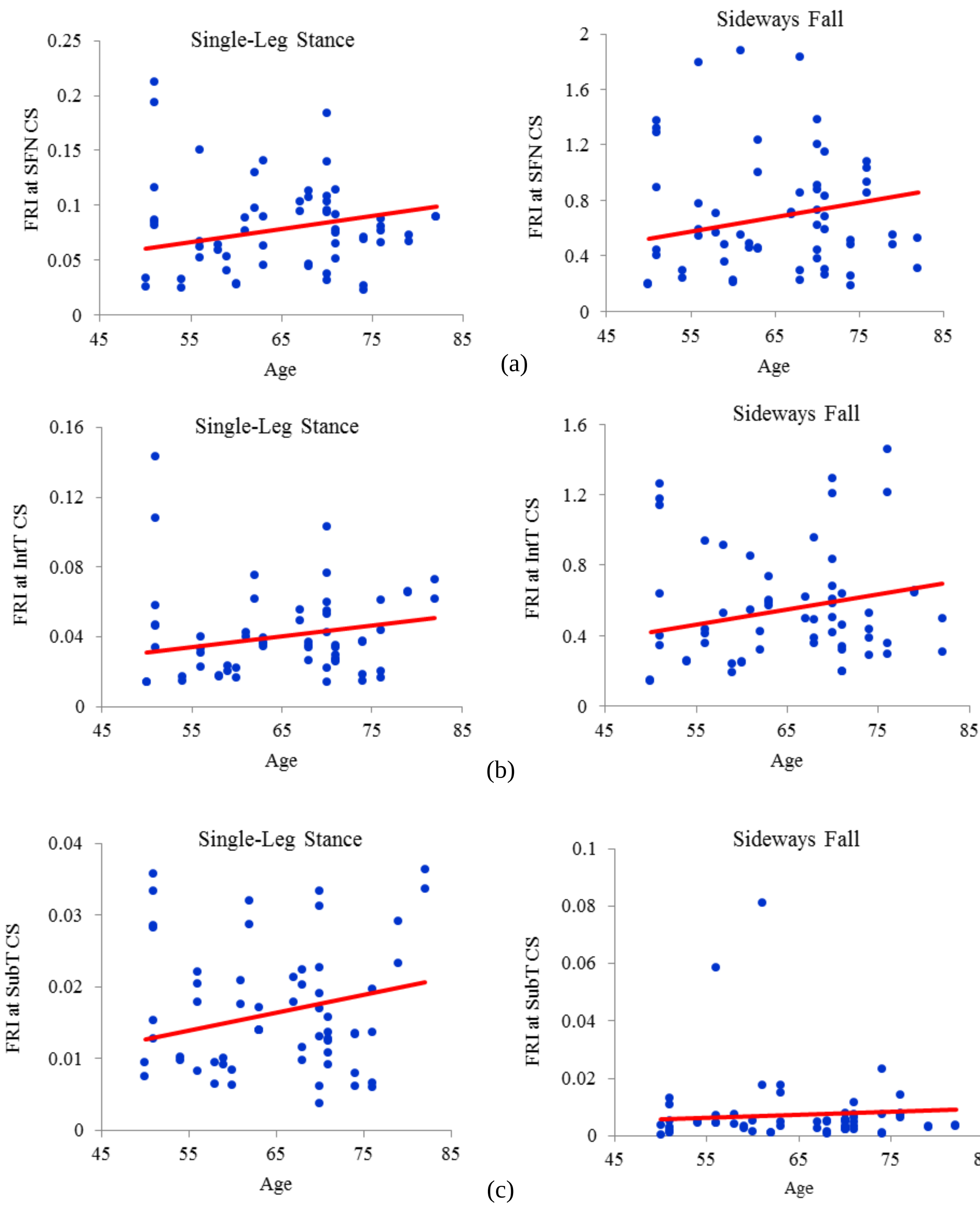

Figure 4-31. Variation of FRI with age in 30 females at (a) the smallest femoral neck cross-section (SFN CS); (b) the intertrochanteric cross-section (IntT CS); and (c) the subtrochanteric cross-section (SubT CS).

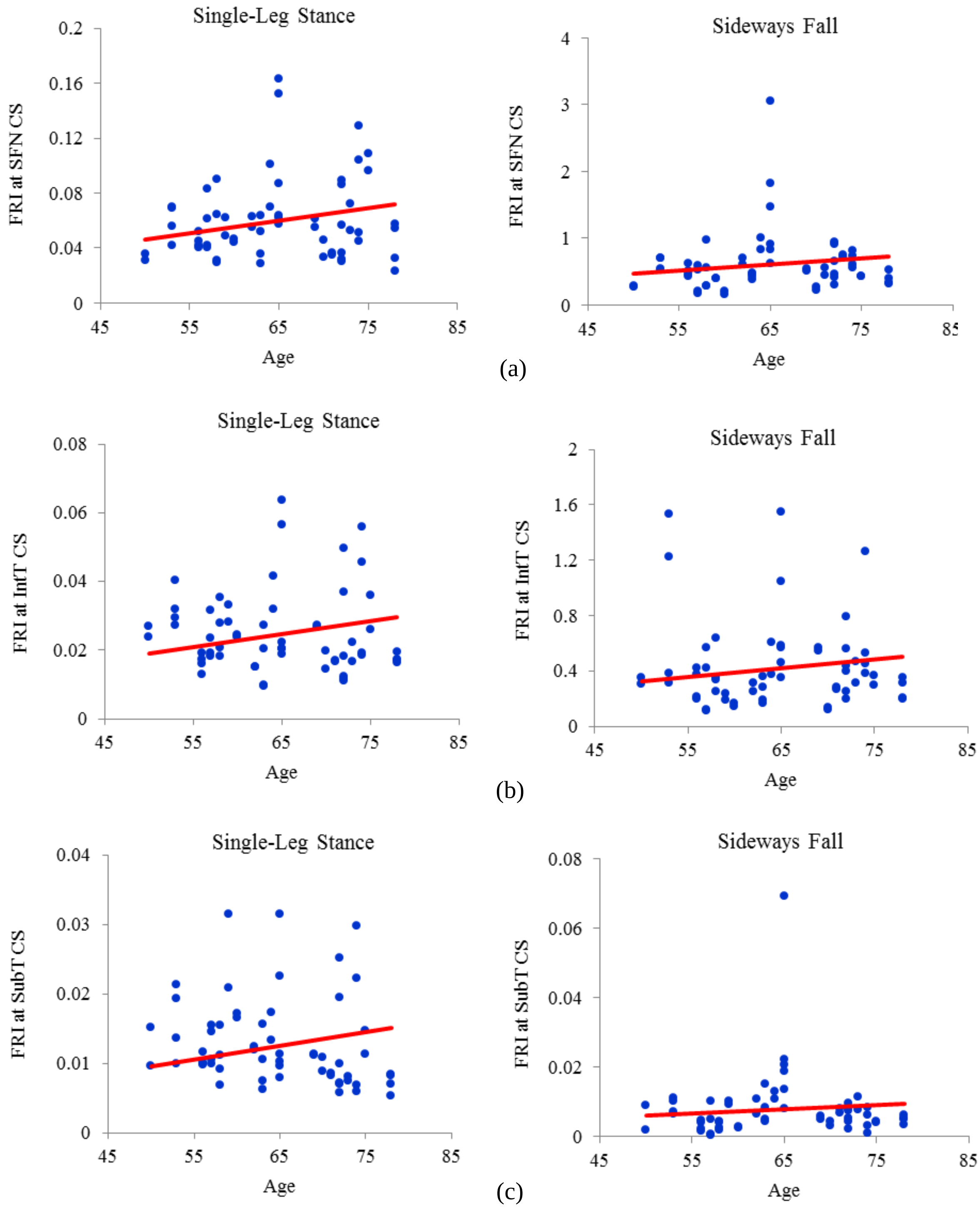

Figure 4-32. Variation of FRI with age in 30 males at (a) the smallest femoral neck cross-section (SFN CS); (b) the intertrochanteric cross-section (IntT CS); and (c) the subtrochanteric cross-section (SubT CS).

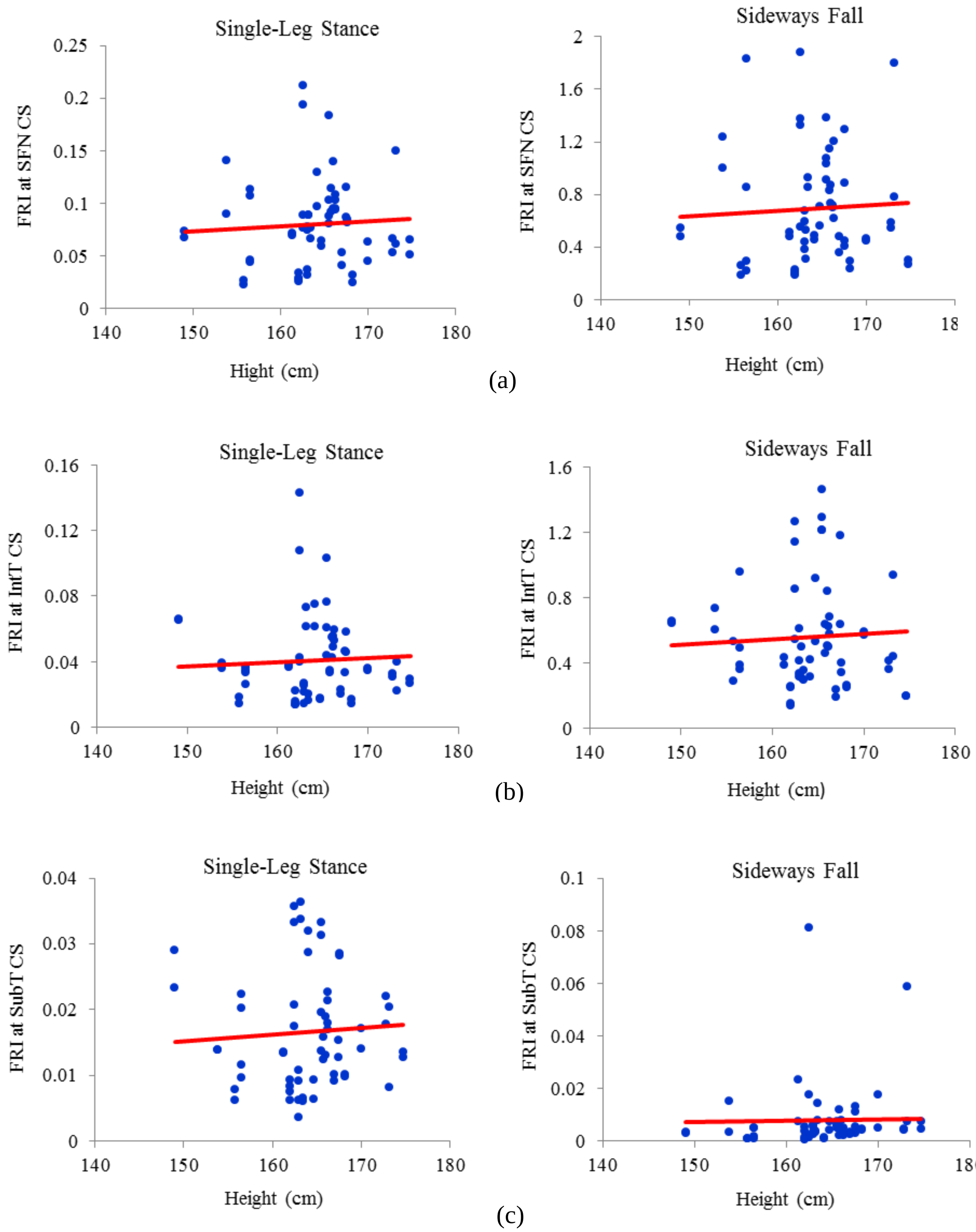

Figure 4-33. Variation of FRI with height in 30 females at (a) the smallest femoral neck cross-section (SFN CS); (b) the intertrochanteric cross-section (IntT CS); and (c) the subtrochanteric cross-section (SubT CS).

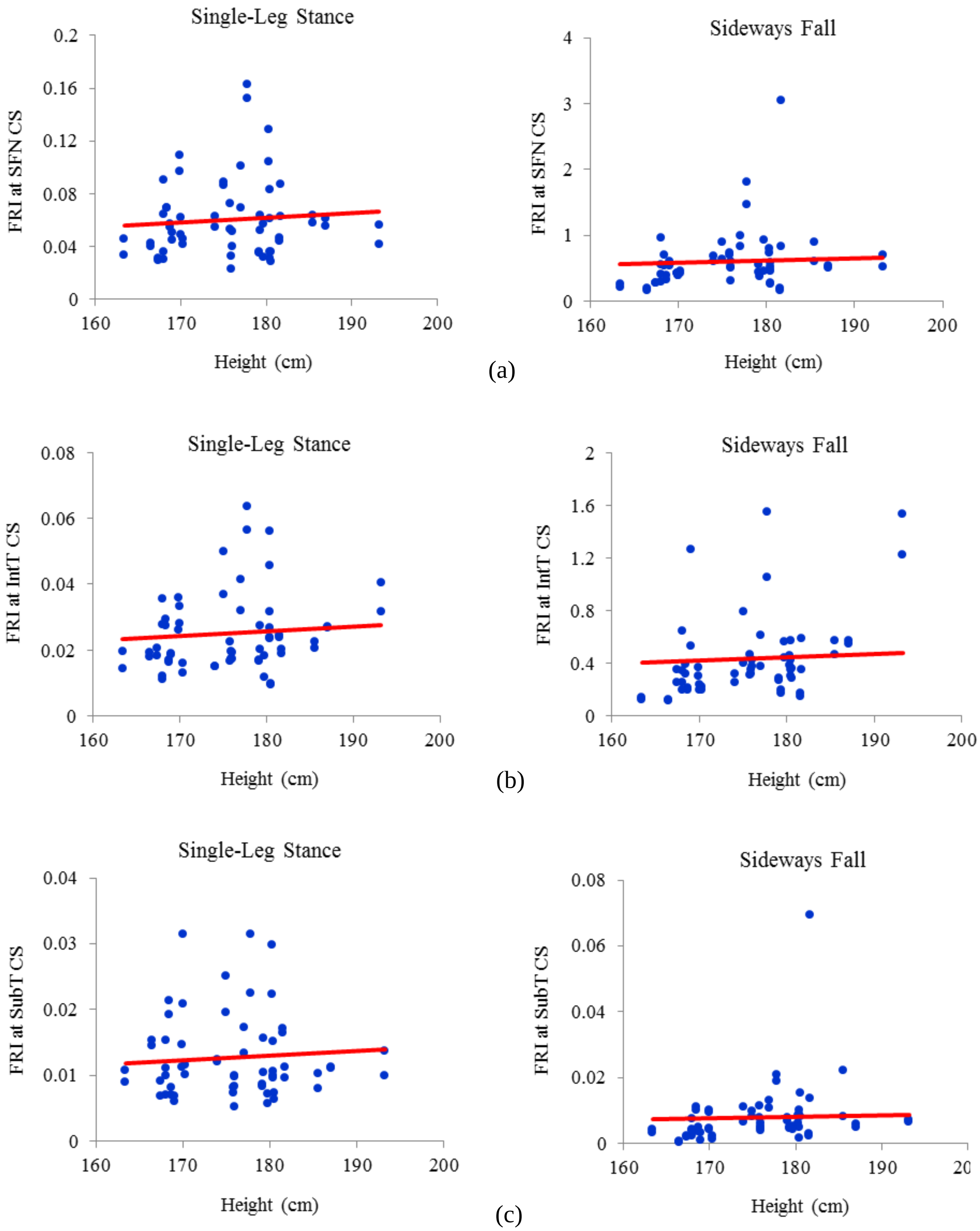

Figure 4-34. Variation of FRI with height in 30 males at (a) the smallest femoral neck cross-section (SFN CS), (b) the intertrochanteric cross-section (IntT CS), and (c) the subtrochanteric cross-section (SubT CS).

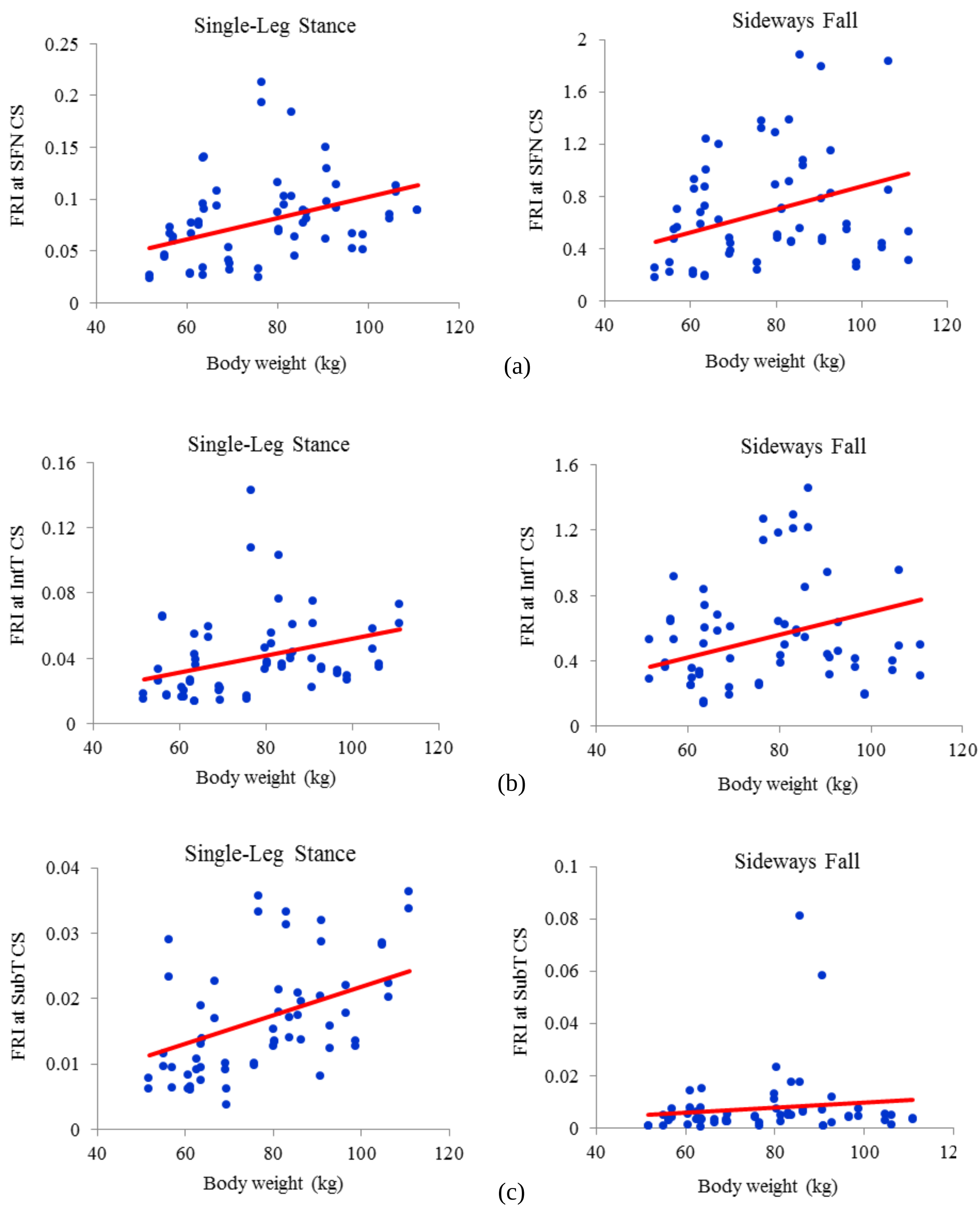

Figure 4-35. Variation of FRI with body weight in 30 females at (a) the smallest femoral neck cross-section (SFN CS), (b) the intertrochanteric cross-section (IntT CS), and (c) the subtrochanteric cross-section (SubT CS).

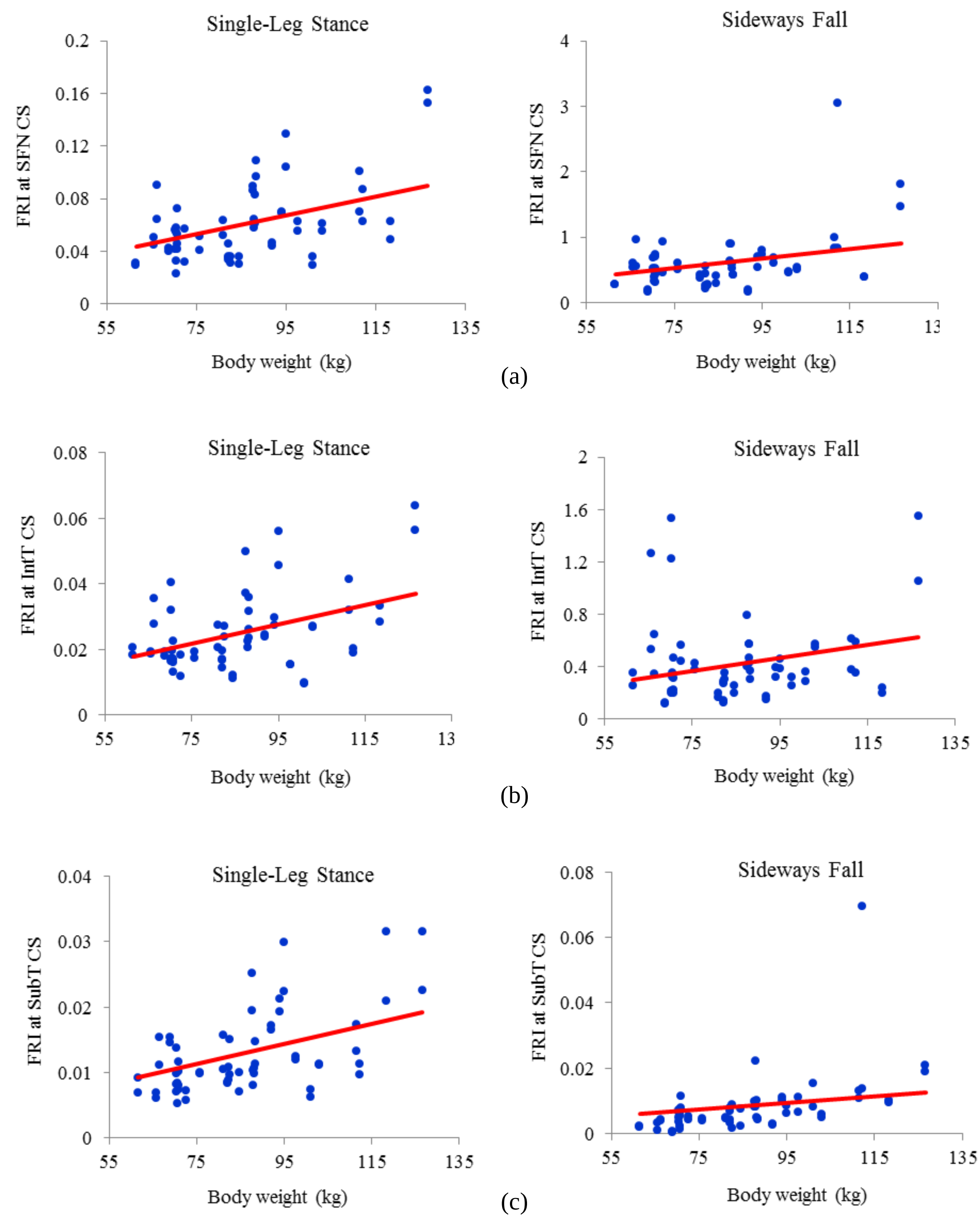

Figure 4-36. Variation of FRI with body weight in 30 males at (a) the smallest femoral neck cross-section (SFN CS), (b) the intertrochanteric cross-section (IntT CS), and (c) the subtrochanteric cross-section (SubT CS).

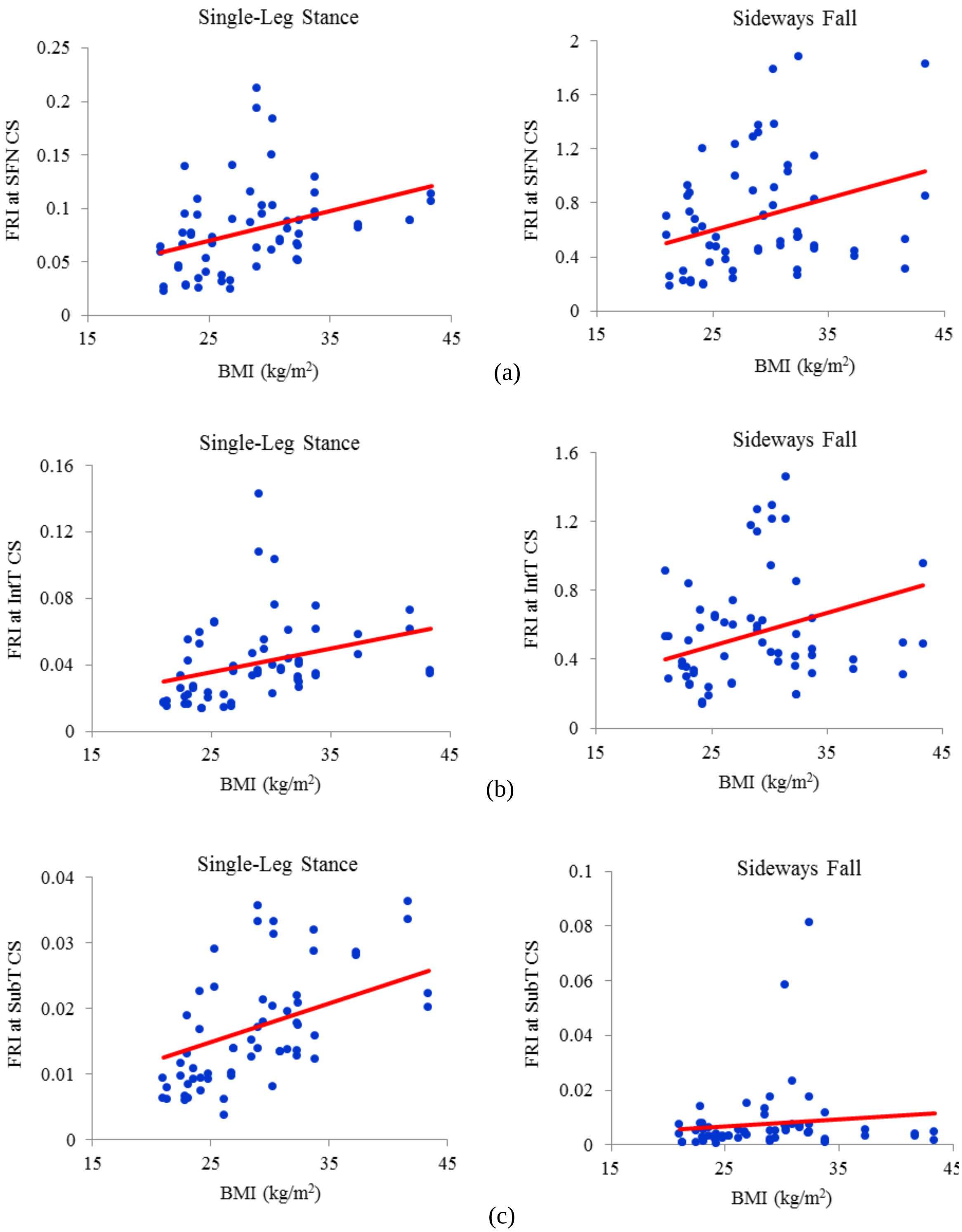

Figure 4-37. Variation of FRI with BMI in 30 females at (a) the smallest femoral neck cross-section (SFN CS), (b) the intertrochanteric cross-section (IntT CS), and (c) the subtrochanteric cross-section (SubT CS).

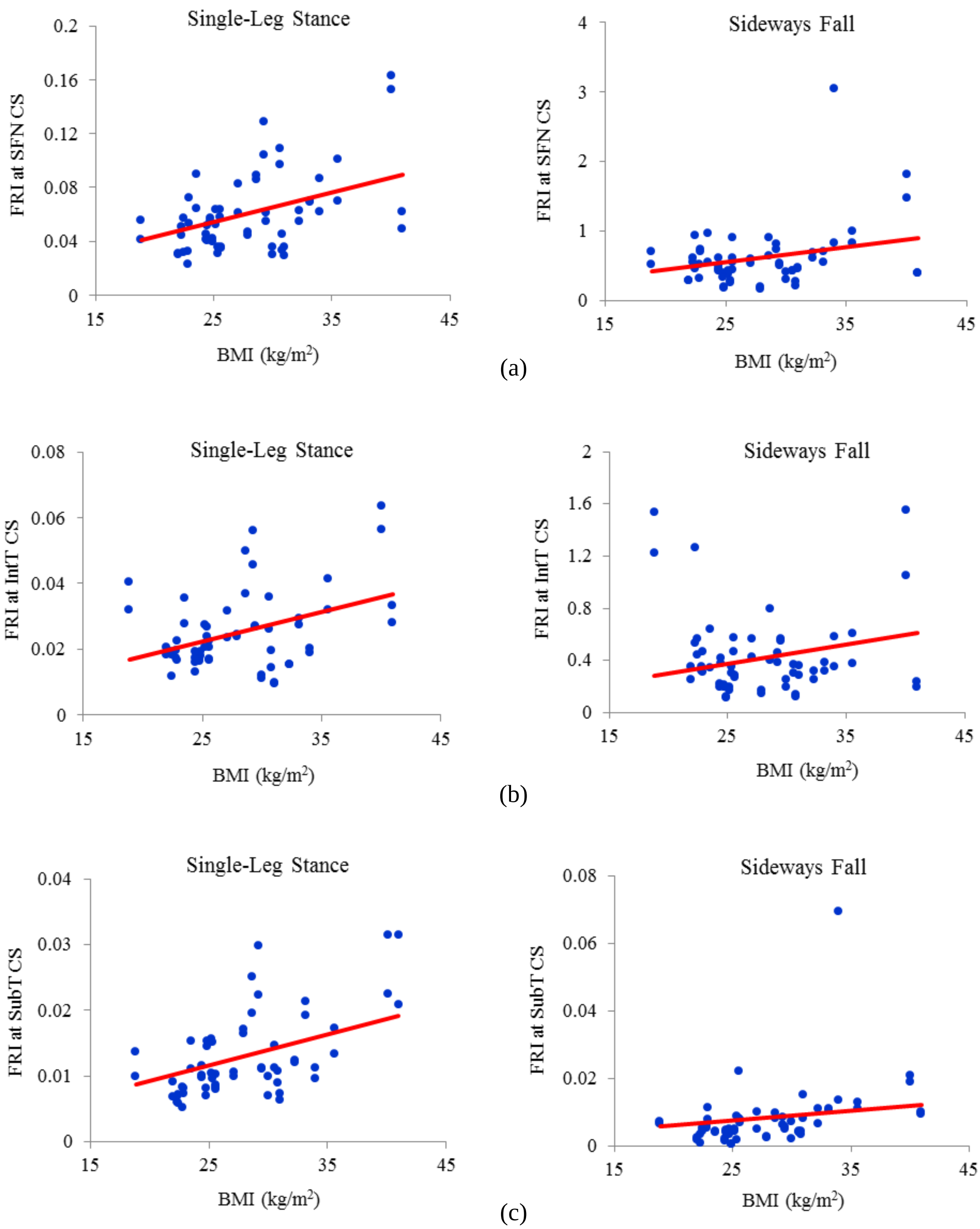

Figure 4-38. Variation of FRI versus BMI in 30 males at (a) the smallest femoral neck cross-section (SFN CS), (b) the intertrochanteric cross-section (IntT CS), and (c) the subtrochanteric cross-section (SubT CS).

4.6 Discussions

4.6.1 Stress and Strain Trends at the Three Critical Cross-Sections

The results of finite element analysis in this study show that during the single-leg stance, the maximum tensile stress appeared in the superior region of femoral neck (Figure 4-7a and Figure 4-9a), and the maximum compressive stress occurred in the inferior region (Figure 4-7b and Figure 4-9b); while during the sideways fall, the maximum tensile stress presented in the inferior region (Figure 4-8a and Figure 4-10a) and the maximum compressive stress showed in the superior region of femoral neck (Figure 4-8b and Figure 4-10b). The superior femoral neck only experiences low tensile stresses during the single-leg stance (Table 4-3); according to the Wolff's Law, bone in this region tends to weaken over time if alternative loading is not regularly applied. During the sideways fall, however, the same area, weakened in normal walking, is heavily loaded in compression (Table 4-3). High compressive stress in the superior region of femoral neck during the sideways fall may initiate a fracture in this region; it propagates into the inferior aspect of the femoral neck. These results show a good agreement with the previous experimental findings [34,93–96].

The maximum von Mises stress in the femoral neck and the intertrochanteric region were larger than that in the subtrochanteric region during the sideways fall (Figure 4-12 and Table 4-5). The maximum von Mises stresses during the single-leg stance (Figure 4-11 and Table 4-4) are in the same range as those during the sideways fall (Figure 4-12 and Table 4-5). Therefore, based on the stress distribution, we should not expect significant difference between the hip FRIs during the single-leg stance and the sideways fall, while from mechanical viewpoint, fracture risk in the sideways fall should be larger than that in the single-leg stance, as the impact force is much larger than the stance force. However, the influence of other parameters, in addition to the stress effects, should be considered to justify the larger fracture risk in the sideways fall. Bone is classified as a brittle material and the effective strains are important parameters in the failure of brittle materials, it encouraged us to investigate the effects of strains in the three critical regions of femur. Results of this study show that the maximum von Mises strains in the femoral neck and the intertrochanteric region are much higher than those in the subtrochanteric region during both the single-leg stance and the sideways fall (Figure 4-13, Figure 4-14, Table 4-6, and Table 4-7). The strains during the single-leg stance (Figure 4-13 and Table 4-6) are much lower than those during the sideways fall (Figure 4-14 and Table 4-7), which may explain the lower hip fracture risk during the single-leg stance.

No agreement has been adopted on the choice of a failure criterion in the analysis of bone failure. In literatures, stress and strain based failure criteria such as the von Mises stress and strain criteria, and the maximum principle stress and strain criteria were commonly used to assess hip fracture risk. To the best of our knowledge, the strain energy based failure criterion has not been used yet for hip fracture risk assessment. Whereas the cancellous bone failure is in the form of buckling and deformation (strain intensity) and the cortical bone failure is related to its local cracking (stress intensity), strain energy failure criterion, which is a combination of both stress and strain intensities, is theoretically more reasonable than other failure criteria for hip fracture risk assessment. The differences between the strains in the three critical regions of femur during both the single-leg stance and the sideways fall (Figure 4-13, Figure 4-14, Table 4-6, and Table 4-7) are much higher than the differences between the corresponding stresses (Figure 4-11, Figure 4-12, Table 4-4, and Table 4-5), indicating bone failure is more sensitive to the strains because of its fragility property, so, the effects of strains should also be considered in bone fracture risk assessment. Therefore, in this study we defined the hip fracture risk index using the strain energy failure criterion, which is theoretically the most appropriate failure criterion based on the bone failure mechanism and microstructure.

4.6.2 Hip Fracture Trend at the Three Critical Cross-Sections

Results of this study show that the femoral neck and the intertrochanteric region have higher fracture risk than the subtrochanteric region (Figure 4-15 to Figure 4-20), which is consistent with the fact that the femoral neck and the intertrochanteric region have a larger proportion of cancellous bone than the subtrochanteric region; and the cancellous bone is generally weaker than the cortical bone. For all subjects, there is a very low hip fracture risk during the single-leg stance (FRI<<1). In the 120 right and left femurs analyzed during the sideways fall, 15 femurs at the femoral neck and 12 femurs at the intertrochanteric region have FRI higher than one (FRI>1); while there is very low fracture risk at the subtrochanteric region for all the subjects (FRI<<1) (Figure 4-21). Our findings have a good agreement with the previous clinical observations. According to the clinical observations, the femoral neck is the most common location for a hip fracture, with 45% to 53% of hip fractures; the intertrochanteric fractures consist approximately 38% to 50% of hip fractures; and the subtrochanteric fractures are less common than the femoral neck and intertrochanteric fractures, with approximately 5% to 15% of hip fractures [85,86]. Also the same frequency of the femoral neck and intertrochanteric fractures was observed in patients with age between 65 and 99 [87]. Data on 176 geriatric patients with hip fractures showed that 59% were the intertrochanteric fractures while the rest (41%) were the intracapsular neck fractures [88]. In another study by Michelson et al. [89], it was observed that 37% of hip fractures are in the femoral neck, 49% are intertrochanteric, and 14% are subtrochanteric. Therefore, according to our findings and several clinical observations over the world, the femoral neck and the intertrochanteric region are more disposed to fracture than the subtrochanteric region.

Both the fracture risk level and the potential fracture location are patient-dependent and depend on BMD, BMI, and etc., which can be observed from the results shown in Figure 4-15, Figure 4-16, Figure 4-18, and Figure 4-19. For the single-leg stance, fracture risk in the three critical regions of femur is very low (FRI<<1) in all cases (Figure 4-15 and Figure 4-16), indicating femur is not disposed to fracture during the single-leg stance. However, fracture risk of the femoral neck is higher than the intertrochanteric and the subtrochanteric regions during the single-leg stance. During the sideways fall, in most cases, the highest fracture risk was observed at the femoral neck; while in some cases, the fracture risk in the intertrochanteric region was the highest (Figure 4-18 and Figure 4-19).

4.6.3 Hip Fracture Trend in Women and Men

We have also found that women generally have lower bone strength than men and thus expose to higher hip fracture risk during both the single-leg stance and the sideways fall (Figure 4-22 to Figure 4-29). There are 12 and 7 probable hip fracture incidences (FRI>1) at the femoral neck and the intertrochanteric region respectively in 30 women, while 3 probable femoral neck fractures and 5 probable intertrochanteric fractures (FRI>1) were identified in 30 men (Figure 4-30). Our finding is consistent with other studies that have found hip fracture risk in women is generally higher than men. The results of a world-wide study by Dhanwal, et al. [120] on incidence and epidemiology of hip fractures in Asia, Africa, Europe, Latin America, North America, and Oceania show that women are more disposed to the hip fracture risk than men in different countries over the world. In the study by Jacobsen et al. [121], the rate of hip fracture incidence in white US male and female were 4.3 and 8.1 per 1,000 per year, respectively. It was also found that lifetime risk of a hip fracture is 16 percent for a white woman and 5 percent for a white man [122]. Higher hip fracture risk in women may be related to their lower BMD.

4.6.4 Effective Parameters on Hip Fracture Trend

Different parameters such as age, height, weight, and body mass index may influence on the hip fracture risk in the elderly. Therefore, the correlations of hip fracture risk with age, body height, weight, and BMI were investigated in this study (Figure 4-31 to Figure 4-38) and the corresponding correlation coefficients were obtained (Table 4-15 to Table 4-18). Generally, there is an increasing trend of hip fracture risk with age, body height, weight, and BMI at the three critical regions of femur in both women and men during the single-leg stance and the sideways fall.

The correlation of hip fracture risk with age and height are not significant ($p > 0.05$) for the clinical cases investigated in this study. It means that at least for the clinical cases investigated in this study, we cannot conclude that the hip fracture risk strongly increases with age and it may depend on the individual's health status and life style. However, because we did not have any information about the subject's other health status, life style, medication, and etc., we were not able to consider the effects of these factors.

The results of this study also show that to some extent there is a strong correlation between the hip fracture risk with body weight and BMI ($p < 0.05$). It indicates that subjects with higher body weight and BMI, overweight and obese subjects, are more prone to hip fracture risk. However, the number of cases used in this study is small. To draw stronger conclusions about the effects of different parameters on hip fracture risk in the elderly, a large number of clinical cohorts are needed, while in this study we only investigated 60 clinical cases.

Chapter 5

Conclusions and Future Work

5.1 Conclusions and Contributions

Hip fracture is now a global health issue for old people. A lot of attention has been paid to it, due to the number of hip fracture is increasing over the world. A reliable methodology to assess hip fracture risk in individuals is very important for preventing hip fracture and initiating a treatment. In this reported research, the purpose is to assess hip fracture risk more precisely using the strain energy failure criterion, which can better describe bone failure mechanism and microstructure, and implemented in finite element model constructed from QCT images.

A total of 60 clinical cases (30 females and 30 males, totally 120 right and left femurs), with age in the scope from 50 to 82 years (average of 65 years) were obtained from the Winnipeg Health Science Centre for the investigation. QCT-based FE models were constructed based on the QCT image of the subjects. FE analysis was then performed for the single-leg stance and the sideways fall configuration. Hip FRI was defined using the strain energy criterion at the three critical cross-sections of femur, namely, the smallest femoral neck cross-section, the intertrochanteric cross-section, and the subtrochanteric cross-section.

The proposed fracture risk index can predict not only the fracture risk level, but also the potential fracture location. The results of this study showed that there is a very low hip fracture risk during the single-leg stance. While during the sideways fall, there is a high fracture risk at the femoral neck and the intertrochanteric region, compared to the subtrochanteric region. Based on the results obtained from this study, women are more prone to hip fracture than men and the probability of hip fracture in women is considerably higher than in men.

The procedure described in Figure 3-1 can be implemented into computer programming and used in hip fracture prevention and monitoring of osteoporosis treatments in the elderly. The method can also help us in design of more effective hip protectors, and even customized hip protectors can be achieved for seniors. However, the main limitation of this study is the experimental validation of the predicted fracture risk levels and potential fracture locations determined by the strain energy criterion. In the experimental validation, a comparison can be made between the FRIs computed using the strain energy criterion and those obtained from the other failure criteria. Experimental validation is set as future work.

The main contributions from the current study include:

1. An algorithm has been introduced for hip fracture risk assessment at the three critical cross-sections of femur using the strain energy criterion and QCT-based FE modeling.
2. The proposed definition of hip FRI based on the strain energy criterion is theoretically more reasonable. The strain energy criterion can better describe bone failure mechanism, as it integrates all information of stresses, strains and material properties in the bone.
3. A semi-automatic FE analysis procedure simulating the single-leg stance and the sideways fall is implemented using in-house APDL codes, with the stance and impact forces determined from the subject's body weight and height; the in-house developed MATLAB codes are able to automatically calculate FRI at the three critical cross-sections of femur.

5.2 Future Work

Although there is a good agreement between the results of this study and the findings of the previous clinical studies, there is a number of future works to improve and validate the proposed methodology. The suggested future works include:

1. Conducting in-vitro experiments to validate the fracture risk levels and the potential fracture locations determined by the strain energy criterion
2. Calculating the hip FRIs using other failure criteria and comparing them with the FRIs obtained using the strain energy criterion

3. Investigating the sensitivity of the FRIs at the three critical cross-sections respect to clinical risk factors, for example, life style, medication, alcohol consumption, and etc.

Bibliography

[1] Cummings, S. R., and Melton, L. J., 2002, "Epidemiology and outcomes of osteoporotic fractures," The Lancet, **359**(9319), pp. 1761–1767.

[2] Cooper, C., Atkinson, E. J., MichaelO'Fallon, W., and Melton, J. L., 1992, "Incidence of clinically diagnosed vertebral fractures: A population-based study in rochester, minnesota, 1985-1989," J. Bone Miner. Res., **7**(2), pp. 221–227.

[3] Unnanuntana, A., Gladnick, B. P., Donnelly, E., and Lane, J. M., 2010, "The Assessment of Fracture Risk," J. Bone Joint Surg. Am., **92**(3), pp. 743–753.

[4] Kanis, J. A., Odén, A., McCloskey, E. V., Johansson, H., Wahl, D. A., Cooper, C., and Life, on behalf of the I. W. G. on E. and Q. of, 2012, "A systematic review of hip fracture incidence and probability of fracture worldwide," Osteoporos. Int., **23**(9), pp. 2239–2256.

[5] Lauritzen, J. B., 1996, "Hip fractures: incidence, risk factors, energy absorption, and prevention," Bone, **18**(1 Suppl), p. 65S–75S.

[6] "What is Osteoporosis?," Osteoporos. Can. [Online]. Available: https://www.osteoporosis.ca/osteoporosis-and-you/what-is-osteoporosis/.

[7] Cummings, S. R., Kelsey, J. L., Nevitt, M. C., and O'Dowd, K. J., 1985, "Epidemiology of osteoporosis and osteoporotic fractures," Epidemiol. Rev., **7**, pp. 178–208.

[8] Melton, L. J., Chrischilles, E. A., Cooper, C., Lane, A. W., and Riggs, B. L., 1992, "Perspective how many women have osteoporosis?," J. Bone Miner. Res., **7**(9), pp. 1005–1010.

[9] Gullberg, B., Johnell, O., and Kanis, J. A., 1997, “World-wide Projections for Hip Fracture,” Osteoporos. Int., **7**(5), pp. 407–413.

[10] Johnell, O., 1997, “The socioeconomic burden of fractures: today and in the 21st century,” Am. J. Med., **103**(2A), p. 20S–25S; discussion 25S–26S.

[11] Resnick, N. M., and Greenspan, S. L., 1989, “‘Senile’ osteoporosis reconsidered,” JAMA, **261**(7), pp. 1025–1029.

[12] Grisso, J. A., Kelsey, J. L., Strom, B. L., Ghiu, G. Y., Maislin, G., O’Brien, L. A., Hoffman, S., and Kaplan, F., 1991, “Risk Factors for Falls as a Cause of Hip Fracture in Women,” N. Engl. J. Med., **324**(19), pp. 1326–1331.

[13] Nevitt, M. C., Cummings, S. R., Kidd, S., and Black, D., 1989, “Risk factors for recurrent nonsyncopal falls. A prospective study,” JAMA, **261**(18), pp. 2663–2668.

[14] Binkovitz, L. A., and Henwood, M. J., 2007, “Pediatric DXA: technique and interpretation,” Pediatr. Radiol., **37**(1), pp. 21–31.

[15] WHO Study Group, 1994, “Assessment of fracture risk and its application to screening for postmenopausal osteoporosis. Report of a WHO Study Group,” World Health Organ. Tech. Rep. Ser., **843**, pp. 1–129.

[16] Marshall, D., Johnell, O., and Wedel, H., 1996, “Meta-analysis of how well measures of bone mineral density predict occurrence of osteoporotic fractures,” BMJ, **312**(7041), pp. 1254–1259.

[17] Leib, E. S., Lewiecki, E. M., Binkley, N., Hamdy, R. C., and International Society for Clinical Densitometry, 2004, “Official positions of the International Society for Clinical Densitometry,” J. Clin. Densitom. Off. J. Int. Soc. Clin. Densitom., **7**(1), pp. 1–6.

[18] Blake, G. M., Noon, E., Spector, T. D., and Fogelman, I., 2013, “Intervertebral T-Score Differences in Younger and Older Women,” J. Clin. Densitom., **16**(3), pp. 329–335.

[19] Richmond, B., 2003, “DXA scanning to diagnose osteoporosis: do you know what the results mean?,” Cleve. Clin. J. Med., **70**(4), pp. 353–360.

[20] Beck, T. J., 2007, “Extending DXA beyond bone mineral density: understanding hip structure analysis,” Curr. Osteoporos. Rep., **5**(2), pp. 49–55.

[21] Carey, J. J., Delaney, M. F., Love, T. E., Cromer, B. A., Miller, P. D., Richmond, B. J., Manilla-McIntosh, M., Lewis, S. A., Thomas, C. L., and Licata, A. A., 2009, “Dual-Energy X-ray Absorptiometry Diagnostic Discordance Between Z-Scores and T-Scores in Young Adults,” J. Clin. Densitom., **12**(1), pp. 11–16.

[22] Kanis, J. A., Johansson, H., Oden, A., and McCloskey, E. V., 2009, “Assessment of fracture risk,” Eur. J. Radiol., **71**(3), pp. 392–397.

[23] McClung, M. R., 2012, “To FRAX or not to FRAX,” J. Bone Miner. Res., **27**(6), pp. 1240–1242.

[24] Kaptoge, S., Benevolenskaya, L. I., Bhalla, A. K., Cannata, J. B., Boonen, S., Falch, J. A., Felsenberg, D., Finn, J. D., Nuti, R., Hoszowski, K., Lorenc, R., Miazgowski, T., Jajic, I., Lyritis, G., Masaryk, P., Naves-Diaz, M., Poor, G., Reid, D. M., Scheidt-Nave, C., Stepan, J. J., Todd, C. J., Weber, K., Woolf, A. D., Roy, D. K., Lunt, M., Pye, S. R., O’Neill, T. W., Silman, A. J., and Reeve, J., 2005, “Low BMD is less predictive than reported falls for future limb fractures in women across Europe: results from the European Prospective Osteoporosis Study,” Bone, **36**(3), pp. 387–398.

[25] Järvinen, T. L. N., Sievänen, H., Khan, K. M., Heinonen, A., and Kannus, P., 2008, “Shifting the focus in fracture prevention from osteoporosis to falls,” BMJ, **336**(7636), pp. 124–126.

[26] Beck, T. J., Ruff, C. B., Warden, K. E., Scott, W. W., and Rao, G. U., 1990, “Predicting femoral neck strength from bone mineral data. A structural approach,” Invest. Radiol., **25**(1), pp. 6–18.

[27] Uusi-Rasi, K., Beck, T. J., Semanick, L. M., Daphtary, M. M., Crans, G. G., Desaiah, D., and Harper, K. D., 2006, “Structural effects of raloxifene on the proximal femur: results from the multiple outcomes of raloxifene evaluation trial,” Osteoporos. Int., **17**(4), pp. 575–586.

[28] Khoo, B. C. C., Beck, T. J., Qiao, Q.-H., Parakh, P., Semanick, L., Prince, R. L., Singer, K. P., and Price, R. I., 2005, "In vivo short-term precision of hip structure analysis variables in comparison with bone mineral density using paired dual-energy X-ray absorptiometry scans from multi-center clinical trials," Bone, **37**(1), pp. 112–121.

[29] Testi, D., Viceconti, M., Baruffaldi, F., and Cappello, A., 1999, "Risk of fracture in elderly patients: a new predictive index based on bone mineral density and finite element analysis," Comput. Methods Programs Biomed., **60**(1), pp. 23–33.

[30] Luo, Y., Ferdous, Z., and Leslie, W. D., 2013, "Precision study of DXA-based patient-specific finite element modeling for assessing hip fracture risk," Int. J. Numer. Methods Biomed. Eng., **29**(5), pp. 615–629.

[31] Luo, Y., Ferdous, Z., and Leslie, W. D., 2011, "A preliminary dual-energy X-ray absorptiometry-based finite element model for assessing osteoporotic hip fracture risk," Proc. Inst. Mech. Eng. [H], p. 0954411911424975.

[32] Mirzaei, M., Keshavarzian, M., and Naeini, V., 2014, "Analysis of strength and failure pattern of human proximal femur using quantitative computed tomography (QCT)-based finite element method," Bone, **64**, pp. 108–114.

[33] Taddei, F., Cristofolini, L., Martelli, S., Gill, H. S., and Viceconti, M., 2006, "Subject-specific finite element models of long bones: An in vitro evaluation of the overall accuracy," J. Biomech., **39**(13), pp. 2457–2467.

[34] De Bakker, P. M., Manske, S. L., Ebacher, V., Oxland, T. R., Cripton, P. A., and Guy, P., 2009, "During sideways falls proximal femur fractures initiate in the superolateral cortex: Evidence from high-speed video of simulated fractures," J. Biomech., **42**(12), pp. 1917–1925.

[35] Dall'Ara, E., Luisier, B., Schmidt, R., Kainberger, F., Zysset, P., and Pahr, D., 2013, "A nonlinear QCT-based finite element model validation study for the human femur tested in two configurations in vitro," Bone, **52**(1), pp. 27–38.

[36] Keyak, J. H., Rossi, S. A., Jones, K. A., Les, C. M., and Skinner, H. B., 2001, “Prediction of fracture location in the proximal femur using finite element models,” Med. Eng. Phys., **23**(9), pp. 657–664.

[37] Bessho, M., Ohnishi, I., Matsumoto, T., Ohashi, S., Matsuyama, J., Tobita, K., Kaneko, M., and Nakamura, K., 2009, “Prediction of proximal femur strength using a CT-based nonlinear finite element method: Differences in predicted fracture load and site with changing load and boundary conditions,” Bone, **45**(2), pp. 226–231.

[38] Dragomir-Daescu, D., Buijs, J. O. D., McEligot, S., Dai, Y., Entwistle, R. C., Salas, C., Iii, L. J. M., Bennet, K. E., Khosla, S., and Amin, S., 2010, “Robust QCT/FEA Models of Proximal Femur Stiffness and Fracture Load During a Sideways Fall on the Hip,” Ann. Biomed. Eng., **39**(2), pp. 742–755.

[39] Koivumäki, J. E. M., Thevenot, J., Pulkkinen, P., Kuhn, V., Link, T. M., Eckstein, F., and Jämsä, T., 2012, “Ct-based finite element models can be used to estimate experimentally measured failure loads in the proximal femur,” Bone, **50**(4), pp. 824–829.

[40] Nishiyama, K. K., Gilchrist, S., Guy, P., Cripton, P., and Boyd, S. K., 2013, “Proximal femur bone strength estimated by a computationally fast finite element analysis in a sideways fall configuration,” J. Biomech., **46**(7), pp. 1231–1236.

[41] Keyak, J. H., Rossi, S. A., Jones, K. A., and Skinner, H. B., 1997, “Prediction of femoral fracture load using automated finite element modeling,” J. Biomech., **31**(2), pp. 125–133.

[42] Lotz, J. C., Cheal, E. J., and Hayes, W. C., 1991, “Fracture Prediction for the Proximal Femur Using Finite Element Models: Part I—Linear Analysis,” J. Biomech. Eng., **113**(4), pp. 353–360.

[43] Lotz, J. C., Cheal, E. J., and Hayes, W. C., 1991, “Fracture Prediction for the Proximal Femur Using Finite Element Models: Part II—Nonlinear Analysis,” J. Biomech. Eng., **113**(4), pp. 361–365.

[44] Ota, T., Yamamoto, I., and Morita, R., 1999, “Fracture simulation of the femoral bone using the finite-element method: How a fracture initiates and proceeds,” J. Bone Miner. Metab., **17**(2), pp. 108–112.

[45] Schileo, E., Taddei, F., Cristofolini, L., and Viceconti, M., 2008, “Subject-specific finite element models implementing a maximum principal strain criterion are able to estimate failure risk and fracture location on human femurs tested in vitro,” J. Biomech., **41**(2), pp. 356–367.

[46] Keyak, J. H., and Rossi, S. A., 2000, “Prediction of femoral fracture load using finite element models: an examination of stress- and strain-based failure theories,” J. Biomech., **33**(2), pp. 209–214.

[47] Stölken, J. S., and Kinney, J. H., 2003, “On the importance of geometric nonlinearity in finite-element simulations of trabecular bone failure,” Bone, **33**(4), pp. 494–504.

[48] Cordey, J., and Gautier, E., 1999, “Strain gauges used in the mechanical testing of bones Part I: Theoretical and technical aspects,” Injury, **30, Supplement 1**, pp. SA7–SA13.

[49] Mirzaei, M., Zeinali, A., Razmjoo, A., and Nazemi, M., 2009, “On prediction of the strength levels and failure patterns of human vertebrae using quantitative computed tomography (QCT)-based finite element method,” J. Biomech., **42**(11), pp. 1584–1591.

[50] Sih, G. C., 1974, “Strain-energy-density factor applied to mixed mode crack problems,” Int. J. Fract., **10**(3), pp. 305–321.

[51] Sih, G. C., 1991, Mechanics of Fracture Initiation and Propagation, Springer Netherlands, Dordrecht.

[52] Wei, Y., 2012, “An extended strain energy density failure criterion by differentiating volumetric and distortional deformation,” Int. J. Solids Struct., **49**(9), pp. 1117–1126.

[53] Wolfe, W. E., and Butalia, T. S., 1998, “A Strain-Energy Based Failure Criterion for Non-Linear Analysis of Composite Laminates Subjected to Biaxial Loading,” Compos. Sci. Technol., **58**(7), pp. 1107–1124.

[54] Butalia, T. S., and Wolfe, W. E., 2002, “A strain-energy-based non-linear failure criterion: comparison of numerical predictions and experimental observations for symmetric composite laminates,” Compos. Sci. Technol., **62**(12–13), pp. 1697–1710.

[55] Vasu, R., Carter, D. R., and Harris, W. H., 1983, “Evaluation of Bone Cement Failure Criteria With Applications to the Acetabular Region,” J. Biomech. Eng., **105**(4), pp. 332–337.

[56] “File:Gray’s Anatomy 20th edition (1918)- Title page.png,” Wikipedia Free Encycl.

[57] “Hip Anatomy, Pictures, Function, Problems & Treatment.”

[58] Ranit, R., “Femoroacetabular Impingement Syndrome (FAIS) – Hip Pain,” Val. Health Clin.

[59] Reis, J., Silva, F. C. E., Queiroga, C., Lucena, S., and Potes, J., 2011, “Bone mechanotransduction: A review,” J. Biomed. Bioeng., **2**(1), pp. 37–44.

[60] Jee, W., 2001, Integrated bone tissue physiology: Anatomy and physiology. In Cowin S (ed) Bone Mechanics Handbook, Taylor & Francis.

[61] Tortora, G. J., and Derrickson, B., 2013, Principle of Anatomy & Physiology, 14th Edition, John Wiley.

[62] Nigg, B. M., and Herzog, W., 2007, Biomechanics of the Musculo-skeletal System,3rd Edition, John Wiley.

[63] Currey, J. D., 2002, Bones: Structure and Mechanics, Princeton, NJ, Princeton University Press.

[64] 2015, “Long bone,” Wikipedia Free Encycl.

[65] Weiner, S., and Wagner, H. D., 1998, “The Material Bone: Structure-Mechanical Function Relations,” Annu. Rev. Mater. Sci., **28**(1), pp. 271–298.

[66] Keaveny, T. M., and Hayes, W. C., 1993, “A 20-Year Perspective on the Mechanical Properties of Trabecular Bone,” J. Biomech. Eng., **115**(4B), pp. 534–542.

[67] Goldstein, S. A., Wilson, D. L., Sonstegard, D. A., and Matthews, L. S., 1983, “The mechanical properties of human tibial trabecular bone as a function of metaphyseal location,” J. Biomech., **16**(12), pp. 965–969.

[68] Carter, D. R., and Hayes, W. C., 1977, “The compressive behavior of bone as a two-phase porous structure,” J. Bone Jt. Surg., **59**(7), pp. 954–962.

[69] Baca, V., Horak, Z., Mikulenka, P., and Dzupa, V., 2008, “Comparison of an inhomogeneous orthotropic and isotropic material models used for FE analyses,” Med. Eng. Phys., **30**(7), pp. 924–930.

[70] Peng, L., Bai, J., Zeng, X., and Zhou, Y., 2006, “Comparison of isotropic and orthotropic material property assignments on femoral finite element models under two loading conditions,” Med. Eng. Phys., **28**(3), pp. 227–233.

[71] Rachner, T. D., Khosla, S., and Hofbauer, L. C., 2011, “Osteoporosis: now and the future,” The Lancet, **377**(9773), pp. 1276–1287.

[72] Daniel, T., 1996, Metabolic bone disease. Textbook of Primary Care Medicine. John N (ed). St. Louis, CV Mosby Publisher.

[73] Charles, H., 1997, Approach to the elderly patient with osteopenia or osteoporosis. Textbook of Internal Medicine. William NK (ed)., Lippincott-Raven Publishers, Philadelphia.

[74] Anderson, F., 1997, “Osteoporosis in men.,” Int. J. Clin. Pract., **52**(3), pp. 176–180.

[75] Gallagher, J., 1999, Osteoporosis. Conn’s Current Therapy. Robert ER (ed), Philadelphia, WB Saunders Co.

[76] Riggs, B. L., Khosla, S., and Melton, L. J., 2002, “Sex Steroids and the Construction and Conservation of the Adult Skeleton,” Endocr. Rev., **23**(3), pp. 279–302.

[77] Khosla, S., and Riggs, B. L., 2005, "Pathophysiology of Age-Related Bone Loss and Osteoporosis," Endocrinol. Metab. Clin. North Am., **34**(4), pp. 1015–1030.

[78] Abrahamsen, B., Staa, T. van, Ariely, R., Olson, M., and Cooper, C., 2009, "Excess mortality following hip fracture: a systematic epidemiological review," Osteoporos. Int., **20**(10), pp. 1633–1650.

[79] Butler, M., Forte, M., Kane, R. L., Joglekar, S., Duval, S. J., Swiontkowski, M., and Wilt, T., 2009, Treatment of Common Hip Fractures, Agency for Healthcare Research and Quality (US).

[80] Vega, E., Mautalen, C., Gómez, H., Garrido, A., Melo, L., and Sahores, A. O., 1991, "Bone mineral density in patients with cervical and trochanteric fractures of the proximal femur," Osteoporos. Int. J. Establ. Result Coop. Eur. Found. Osteoporos. Natl. Osteoporos. Found. USA, **1**(2), pp. 81–86.

[81] Nakamura, N., Kyou, T., Takaoka, K., Ohzono, K., and Ono, K., 1992, "Bone mineral density in the proximal femur and hip fracture type in the elderly," J. Bone Miner. Res., **7**(7), pp. 755–759.

[82] Greenspan, S. L., Myers, E. R., Maitland, L. A., Kido, T. H., Krasnow, M. B., and Hayes, W. C., 1994, "Trochanteric bone mineral density is associated with type of hip fracture in the elderly," J. Bone Miner. Res., **9**(12), pp. 1889–1894.

[83] Mautalen, C. A., Vega, E. M., and Einhorn, T. A., 1996, "Are the etiologies of cervical and trochanteric hip fractures different?," Bone, **18**(3 Suppl), p. 133S–137S.

[84] Birrer, R. B., 2005, Field Guide to Fracture Management, Lippincott Williams & Wilkins.

[85] Koval, K. J., and Zuckerman, J. D., 1994, "Hip Fractures: I. Overview and Evaluation and Treatment of Femoral-Neck Fractures," J. Am. Acad. Orthop. Surg., **2**(3), pp. 141–149.

[86] "Fixing Hip Fractures" [Online]. Available: http://www.hopkinsmedicine.org/gec/series/fixing_hip_fractures. [Accessed: 05-Mar-2015].

[87] Karagas, M. R., Lu-Yao, G. L., Barrett, J. A., Beach, M. L., and Baron, J. A., 1996, “Heterogeneity of Hip Fracture: Age, Race, Sex, and Geographic Patterns of Femoral Neck and Trochanteric Fractures among the US Elderly,” Am. J. Epidemiol., **143**(7), pp. 677–682.

[88] Trikha, V., and Rastogi, S., 2005, “Epidemiology and Rehabilitation of Hip Fractures in the Geriatric Population,” Indian Journal of Physical Medicine and Rehabilitation, **16**(1), pp. 16–19.

[89] Michelson, J. D., Myers, A., Jinnah, R., Cox, Q., and Van Natta, M., 1995, “Epidemiology of hip fractures among the elderly. Risk factors for fracture type,” Clin. Orthop., (311), pp. 129–135.

[90] “Advanced Orthopedic Specialist” [Online]. Available: http://advancedortho.net/info/hipfractureinfo.php.

[91] Neumann, D. A., 2002, Kinesiology of the Musculoskeletal System, Elsevier – Health Sciences Division, Philadelphia, Pennsylvania.

[92] Nachreiner, N. M., Findorff, M. J., Wyman, J. F., and McCarthy, T. C., 2007, “Circumstances and Consequences of Falls in Community-Dwelling Older Women,” J. Womens Health, **16**(10), pp. 1437–1446.

[93] Lotz, J. C., Cheal, E. J., and Hayes, W. C., 1995, “Stress distributions within the proximal femur during gait and falls: implications for osteoporotic fracture,” Osteoporos. Int. J. Establ. Result Coop. Eur. Found. Osteoporos. Natl. Osteoporos. Found. USA, **5**(4), pp. 252–261.

[94] Verhulp, E., van Rietbergen, B., and Huiskes, R., 2008, “Load distribution in the healthy and osteoporotic human proximal femur during a fall to the side,” Bone, **42**(1), pp. 30–35.

[95] Carpenter, R. D., Beaupré, G. S., Lang, T. F., Orwoll, E. S., and Carter, D. R., 2005, “New QCT Analysis Approach Shows the Importance of Fall Orientation on Femoral Neck Strength,” J. Bone Miner. Res., **20**(9), pp. 1533–1542.

[96] Mayhew, P. M., Thomas, C. D., Clement, J. G., Loveridge, N., Beck, T. J., Bonfield, W., Burgoyne, C. J., and Reeve, J., 2005, “Relation between age,

femoral neck cortical stability, and hip fracture risk," The Lancet, **366**(9480), pp. 129–135.

[97] Yoshikawa, T., Turner, C. h., Peacock, M., Slemenda, C. w., Weaver, C. m., Teegarden, D., Markwardt, P., and Burr, D. b., 1994, "Geometric structure of the femoral neck measured using dual-energy X-ray absorptiometry," J. Bone Miner. Res., **9**(7), pp. 1053–1064.

[98] Turner, C. H., 2005, "The biomechanics of hip fracture," The Lancet, **366**(9480), pp. 98–99.

[99] Brekelmans, W. A., Poort, H. W., and Slooff, T. J., 1972, "A new method to analyse the mechanical behaviour of skeletal parts," Acta Orthop. Scand., **43**(5), pp. 301–317.

[100] Huiskes, R., and Chao, E. Y. S., 1983, "A survey of finite element analysis in orthopedic biomechanics: The first decade," J. Biomech., **16**(6), pp. 385–409.

[101] Liu, X. S., Zhang, X. H., Sekhon, K. K., Adams, M. F., McMahon, D. J., Bilezikian, J. P., Shane, E., and Guo, X. E., 2010, "High-resolution peripheral quantitative computed tomography can assess microstructural and mechanical properties of human distal tibial bone," J. Bone Miner. Res., **25**(4), pp. 746–756.

[102] Burghardt, A. J., Issever, A. S., Schwartz, A. V., Davis, K. A., Masharani, U., Majumdar, S., and Link, T. M., 2010, "High-Resolution Peripheral Quantitative Computed Tomographic Imaging of Cortical and Trabecular Bone Microarchitecture in Patients with Type 2 Diabetes Mellitus," J. Clin. Endocrinol. Metab., **95**(11), pp. 5045–5055.

[103] Cheung, A. M., Adachi, J. D., Hanley, D. A., Kendler, D. L., Davison, K. S., Josse, R., Brown, J. P., Ste-Marie, L.-G., Kremer, R., Erlandson, M. C., Dian, L., Burghardt, A. J., and Boyd, S. K., 2013, "High-Resolution Peripheral Quantitative Computed Tomography for the Assessment of Bone Strength and Structure: A Review by the Canadian Bone Strength Working Group," Curr. Osteoporos. Rep., **11**(2), pp. 136–146.

[104] Keyak, J. H., Meagher, J. M., Skinner, H. B., and Mote Jr, C. D., 1990, "Automated three-dimensional finite element modelling of bone: a new method," J. Biomed. Eng., **12**(5), pp. 389–397.

[105] Keaveny, T. M., Borchers, R. E., Gibson, L. J., and Hayes, W. C., 1993, "Trabecular bone modulus and strength can depend on specimen geometry," J. Biomech., **26**(8), pp. 991–1000.

[106] ANSYS, Ansys, Inc.

[107] Les, C. M., Keyak, J. H., Stover, S. M., Taylor, K. T., and Kaneps, A. J., 1994, "Estimation of material properties in the equine metacarpus with use of quantitative computed tomography," J. Orthop. Res. Off. Publ. Orthop. Res. Soc., **12**(6), pp. 822–833.

[108] Keller, T. S., 1994, "Predicting the compressive mechanical behavior of bone," J. Biomech., **27**(9), pp. 1159–1168.

[109] Reilly, D. T., and Burstein, A. H., 1975, "The elastic and ultimate properties of compact bone tissue," J. Biomech., **8**(6), pp. 393–405.

[110] Van Buskirk, W. C., and Ashman, R. B., 1981, "The elastic moduli of bone," Trans. American Society of Mechanical Engineers (Applied Mechanics Division), American Society of Mechanical Engineers, New York, pp. 131–143.

[111] Robinovitch, S. N., Hayes, W. C., and McMahon, T. A., 1991, "Prediction of Femoral Impact Forces in Falls on the Hip," J. Biomech. Eng., **113**(4), pp. 366–374.

[112] Kim, J. S., Park, T. S., Park, S. B., Kim, J. S., Kim, I. Y., and Kim, S. I., 2000, "Measurement of femoral neck anteversion in 3D. Part 1: 3D imaging method," Med. Biol. Eng. Comput., **38**(6), pp. 603–609.

[113] Atilla, B., Oznur, A., Caglar, O., Tokgozoglu, M., and Alpaslan, M., 2007, "Osteometry of the femora in Turkish individuals: a morphometric study in 114 cadaveric femora as an anatomic basis of femoral component design," Acta Orthop. Traumatol. Turc., **41**(1), pp. 64–68.

[114] Sariali, E., Mouttet, A., Pasquier, G., and Durante, E., 2009, “Three-Dimensional Hip Anatomy in Osteoarthritis: Analysis of the Femoral Offset,” J. Arthroplasty, **24**(6), pp. 990–997.

[115] Mimics, Materialise, Leuven, Belgium.

[116] Nikander, R., Kannus, P., Dastidar, P., Hannula, M., Harrison, L., Cervinka, T., Narra, N. G., Aktour, R., Arola, T., Eskola, H., Soimakallio, S., Heinonen, A., Hyttinen, J., and Sievänen, H., 2008, “Targeted exercises against hip fragility,” Osteoporos. Int., **20**(8), pp. 1321–1328.

[117] Oravec, D., 2009, “Proximal femur FEM representing Different Exercise loadign types. Tampere. Tampere University of Technology,” Tampere University of Technology.

[118] Abe, S., 2013, “Influence of Exercise History on the Proximal Femur Strength; Finite Element Analysis of Female Athletes,” Master Thesis, Tampere University of Tchnology.

[119] Timoshenko, S., and Goodier, J. N., 1951, Theory of Elasticity, McGraw-Hill.

[120] Dhanwal, D. K., Dennison, E. M., Harvey, N. C., and Cooper, C., 2011, “Epidemiology of hip fracture: Worldwide geographic variation,” Indian J. Orthop., **45**(1), pp. 15–22.

[121] Jacobsen, S. J., Goldberg, J., Miles, T. P., Brody, J. A., Stiers, W., and Rimm, A. A., 1990, “Hip fracture incidence among the old and very old: a population-based study of 745,435 cases.,” Am. J. Public Health, **80**(7), pp. 871–873.

[122] Cummings, S. R., Black, D. M., and Rubin, S. M., 1989, “Lifetime risks of hip, Colles’, or vertebral fracture and coronary heart disease among white postmenopausal women,” Arch. Intern. Med., **149**(11), pp. 2445–2448.